International Journal of Automotive Engineering and Technologies
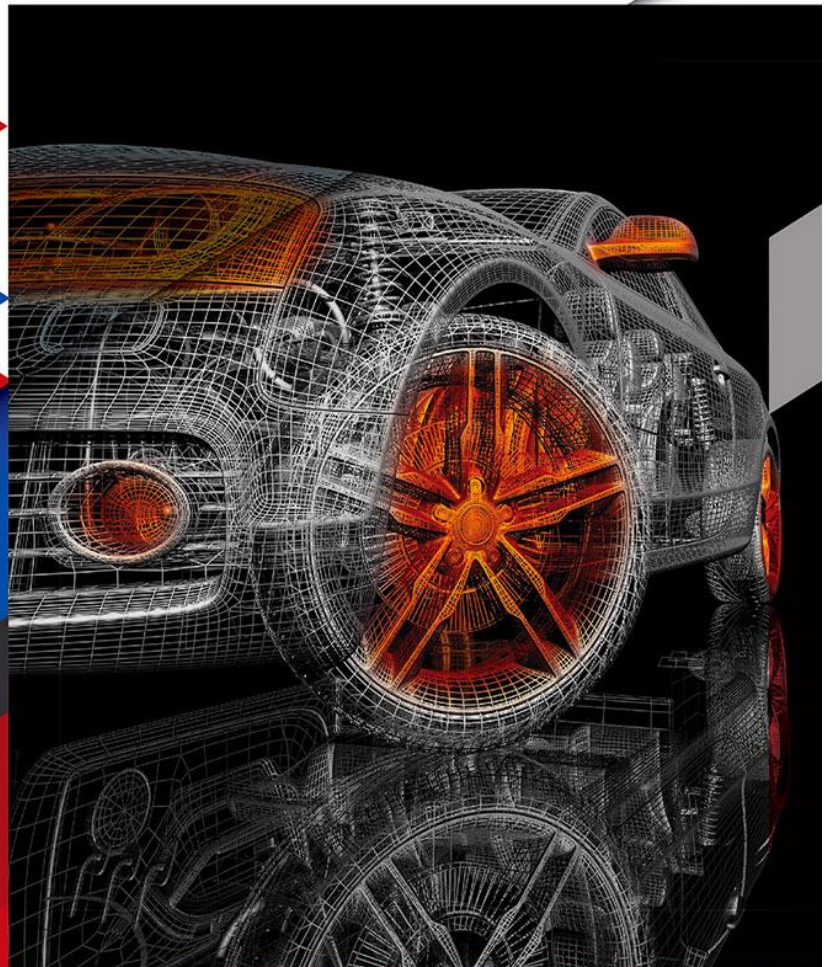
e-mail: editorofijaet@gmail.com

Editor: Prof. Dr. Murat CİNİVİZ

12.	Assoc. Prof. Dr. Sivakumar MUTHUSAMY	K.S.R. College of Engineering	India
13.	Assoc. Prof. Dr. Fuhaid ALSHAMMARI	University of Hail	Saudi Arabia
14.	Prof. Dr. Adrian CLENCI	National University of Science and Technology	Romania
15.	Assoc. Prof. Dr. Ratchagaraja DHAİRİYASAMY	Saveetha Institute of Medical and Technical Sciences, Saveetha University	India
16.	Prof. Dr. Altin DORRİ	Polytechnic University of Tirana	Albania
17.	Assoc. Prof. Dr. Mohamed R. Gomaa	Benha University	Egypt
18.	Dr. Guohong Tian	University of Surrey	United Kingdom

Language Editor

1.	DR. Öznur YEMEZ	Selçuk University	Türkiye

Original Research Article

The effectiveness of iso-alcohols in reducing vapor pressure and enhancing fuel properties of ethanol-gasoline mixtures

hosted by
Turkish JournalPark
ACADEMIC

Nour Eddın Bulbul[1] and Abdülvahap Çakmak[2,*]

[1, 2 *] Samsun University, Faculty of Engineering and Natural Sciences, Mechanical Engineering Department, Ondokuzmayıs, Samsun, Türkiye.

ABSTRACT

Ethanol, with its high octane rating and emissions advantages, is a viable and renewable alternative to gasoline for Spark-Ignition (SI) engines. However, when mixed with gasoline, ethanol forms an azeotropic mixture that increases the fuel's vapor pressure, potentially causing a clogged fuel line, engine stalling, and unstable operation. This study aimed to address the high vapor pressure challenge by adding C3, C4, and C5 iso-alcohols, namely, isopropanol (IP), isobutanol (IB), and isoamyl alcohol (IA), to reduce the vapor pressure of ethanol-gasoline blends. Fuel properties, including Reid vapor pressure (RVP), density, and distillation temperatures, were measured after each iso-alcohol was individually added to ethanol-gasoline blends (E10, E20, and E30) at a 5% volumetric ratio. According to the findings, E10 and E20 behaved as an azeotropic mixture, yielding increased vapor pressure. The highest RVP of 63.2 kPa was measured for E10. However, adding IP, IB, and IA alcohols to E10 reduced the RVP to 61.8 kPa, 61.3 kPa, and 61.1 kPa, respectively. Including iso-alcohols also increased the density of ethanol-gasoline blends, with the highest density of 763.6 kg/m³ was measured for E30+IA5. Furthermore, adding iso-alcohols improved the distillation profiles, octane rating, and heating value of the ethanol-gasoline blends. More importantly, it was found that the measured fuel properties met the requirements of the European Standards for Gasoline (EN 228) except for some gasoline samples' distilled values for E70 and E100. Based on the findings, C3-C5 iso-alcohols effectively reduce the high vapor pressure associated with ethanol-gasoline azeotropic mixtures, allowing a higher volume of renewable ethanol blending.

Keywords: Ethanol-gasoline blends, Reid vapor pressure, Iso-alcohols, Sustainable fuel, Spark-ignition engine

1. Introduction

Environmental, economic, and energy security concerns have driven the growing need for biofuels in engine applications. Biofuels derived from renewable sources can potentially reduce greenhouse gas and pollutant emissions [1]. By decreasing

dependence on imported fossil fuels and diversifying energy sources, biofuels can enhance energy security and independence [2]. In addition, biofuels can be produced from waste, supporting sustainable biofuel production and reducing waste's environmental and health impacts [3]. These advantages are helping to make them a more viable energy source for fueling internal combustion engines (ICEs). Bioethanol, biodiesel, methanol, and biogas are the main biofuels suitable for ICEs. Bioethanol and methanol are viable substitutes for conventional gasoline in SI engines as they offer enhanced fuel properties such as high-octane numbers, oxygen content, and high auto-ignition temperature. Due to its renewable nature and high feedstock availability, ethanol is the most widely used biofuel as a substitute or additive to gasoline in SI engines. Many countries have already incorporated ethanol into their fuel supply, intending to upgrade gasoline quality, reduce their dependence on fossil fuels, and lower greenhouse gas emissions. E5 (5% v/v ethanol + 95% v/v gasoline) and E10 (10% v/v ethanol + 90% v/v gasoline) are the most common ethanol-gasoline blends as they do not require engine modifications. As of January 1, 2011, the Fuel Quality Directive 2009/30/EC in Europe permits a maximum of 10% v/v of ethanol in gasoline [4]. In Türkiye, ethanol is added to gasoline at a maximum volumetric ratio of 5% before the distribution stage to improve fuel properties. Ethanol in gasoline serves as an octane booster and provides oxygen content to improve combustion. E15 is becoming more common, particularly in the United States and Europe. E85, with its high ethanol content, further reduces emissions and fossil fuel consumption. E85 is widely adopted in Brazil and used in flex-fuel vehicles operating on pure gasoline or high ethanol-gasoline mixtures. While ethanol plays a crucial role in reducing carbon emissions and transitioning toward clean and sustainable energy, it has significant limitations, particularly the high vapor pressure of ethanol-gasoline mixtures and its low energy density. Although ethanol has a significantly lower vapor pressure than gasoline due to its stronger intermolecular hydrogen bonds, ethanol-gasoline blends exhibit higher vapor pressure than either pure ethanol or pure gasoline [5]. This is because ethanol and gasoline hydrocarbons combine to form near-azeotropic mixtures that alter the blend's vapor pressure in a non-ideal manner [6]. Increased fuel vapor pressure can cause technical problems, such as blockages in the fuel system, unstable engine operation, and high evaporative HC emissions [7]. The vapor pressure of the fuel also affects combustion efficiency, fuel consumption, and exhaust emissions. Additionally, it plays a significant role in safety in storage distribution and refueling activities [8]. However, excessively low vapor pressure can cause cold start difficulties in cold weather. Therefore, gasoline with slightly higher vapor pressure is marketed in cold weather seasons and cold climate regions to facilitate cold engine starting. The EN 228 gasoline specification regulates the vapor pressure of gasoline for the winter and summer periods. According to this standard, the vapor pressure of winter gasoline should be between 60 and 90 kPa, and the vapor pressure of summer gasoline should fall between 45 and 60 kPa. However, the upper vapor pressure value (60 kPa) given for the summer period is increased depending on the ethanol content. It is 68 kPa for gasoline with 5% v/v ethanol content. Adding ethanol to gasoline can lead to a high vapor pressure value, even exceeding the maximum limit specified in the gasoline specification. The approaches to reducing the vapor pressure of ethanol-gasoline mixture include reformulating the gasoline composition, which poses technical challenges and high processing cost, and adding a third component with lower vapor pressure or high boiling point. The latter is preferable as it is cost-effective and helps stabilize the blend while allowing increasing renewable fuel content [7]. The concept of adding higher alcohol in ethanol-gasoline blends offers the final fuel with a Reid vapor pressure (RVP) equivalent to that of the base gasoline or even below. Recent scientific studies have investigated adding oxygenated compounds to ethanol-gasoline blends to modify their vapor pressure characteristics. Amine and Barakat [9] researched the addition of cyclohexanol (CH) at 3%, v/v to hydrous ethanol-gasoline blends (E0, E5, E10, E15, and

E20) to evaluate phase stability and volatility. The results showed that adding CH to hydrous ethanol-gasoline blends improved water tolerance. Furthermore, cyclohexanol did not negatively impact on the volatility properties of the fuel blends. The study also revealed that blending CH into hydrous ethanol blends reduced the vapor lock index (VLI) due to decreased azeotrope formation.

The same team in a different study [10] examined the effects of adding dimethyl carbonate (DMC) with various volumetric concentrations (0, 2, 4, 6, 8, and 10%) to an ethanol-gasoline blend (E10) on octane numbers and volatility features, such as vapor pressure and distillation profile. The changes in front-end and midrange volatility of the fuel were negligible when DMC was added to the blend. However, the tail-end volatility increased slightly due to the formation of an azeotropic mixture between DMC and the higher boiling components of gasoline. The vapor pressure of E10 was reduced by 3 kPa with a DMC concentration of 8%. The research found that adding 10% DMC to E10 increased the research octane number (RON) by 4 points. As a result, DMC was suggested as an environmentally friendly octane booster additive for E10 fuel blends.

Awad et al. [10] investigated the impact of adding polyoxymethylene dimethyl ether (PODE1) to ethanol-gasoline blend (E10) on fuel properties and phase stability. Their findings showed that E10 remained stable across various PODE1 concentrations (0%, 2.5%, 5%, 7.5%, and 10%). However, the addition of PODE1 slightly influenced the fuel's distillation behavior. Due to the low boiling point of PODE1, it reduced the distillation temperatures, ultimately increasing fuel volatility.

Dash and Tamilvendan [11] examined the effects of co-solvent inclusion on ethanol-gasoline blends, focusing on phase stability, vapor pressure, and distillation properties. Results revealed that adding isopropanol as a co-solvent means that it improves stability at low temperatures and reduces vapor pressure. Further, the vapor pressure decreased with an increase in isopropanol concentration. It was concluded that isopropanol offers an effective solution for enhancing ethanol-blended fuel performance.

Shirazi et al. [12] extensively studied dual-alcohol gasoline blends' physiochemical properties and volatility behavior. Dual-alcohol blends, with volumetric ratios ranging from 10% to 80%, consisting of ethanol or methanol combined with isobutanol or 3-methyl-3-pentanol as the higher alcohols. The main aim of this investigation was to obtain a dual-alcohol-gasoline blend with an RVP matching that of the base gasoline, and it was achieved. All dual-alcohol blends had an RVP within 9% of that of the base gasoline. Moreover, the dual-alcohol blends offered satisfactory fuel properties like volatility, kinematic viscosity, and water tolerance.

The literature survey reveals that various additives are available to reduce the vapor pressure of ethanol-gasoline azeotropic mixtures. Furthermore, long-chain alcohols have been noted as more effective in mitigating the hydroxyl group's azeotropic effect. However, their effectiveness remains unclear, emphasizing the need for comparative study.

This study aims to reduce the vapor pressure of ethanol-gasoline blends by adding C3, C4, and C5 iso-alcohols. Its significance lies in comparing the effectiveness of these iso-alcohols in reducing vapor pressure and improving other critical fuel properties of ethanol-gasoline blends. To the authors' knowledge, no previous study has directly compared the impacts of C3-C5 iso-alcohols on vapor pressure reduction in ethanol-gasoline blends, establishing the novelty of this research.

Higher saturated mono-alcohols, namely, isopropanol (C3), isobutanol (C4), and isoamyl alcohol (C5), were selected as blending components for their low vapor pressure and high-octane numbers. This study's outcomes will contribute to bridging the knowledge gap and offer novel insights into the role of C3, C4, and C5 iso-alcohols as additives in ethanol-gasoline blends.

2. Materials and Methods

Commercial summer gasoline, ethanol (E), isopropanol (IP), isobutanol (IB), and isoamyl alcohol (IA) was used to form fuel samples. The purities of all alcohols used were 99.0% or

greater. The thermophysical properties of gasoline and alcohol are shown in Table 1. Commercial gasoline with an octane number of 95 was obtained from a local fuel station. Fuel blends were prepared using the splash blending method, combining gasoline and alcohol in specific quantities to achieve the desired blend. Blends were homogenized by agitation during the preparation, and this process was repeated before measurements. Binary blends of ethanol-gasoline were prepared by adding ethanol at volumetric ratios of 10%, 20%, and 30% to gasoline. Subsequently, ternary blends were obtained by separately adding isopropanol, isobutanol, and isoamyl alcohol at a volumetric fraction of 5% to binary blends of ethanol-gasoline. Table 2 lists the fuel samples and their compositions.

Table 1: Some thermophysical properties of gasoline and alcohol [7, 13-16].

Property	Gasoline	E	IP	IB	IA
Formula	$\approx C_8H_{15}$	C_2H_6O	C_3H_8O	$C_4H_{10}O$	$C_5H_{12}O$
Oxygen content (wt, %)	≤ 2.7	34.8	26.6	21.6	18.1
Density @ 20°C (kg/m³)	740	790	786	802	810
Octane number	95	108	112	105	113
LHV (kJ/kg)	43400	26700	30662	33500	35370
Stoichiometric AFR	14.6	9.0	10.1	11.2	11.7
Boiling point (°C)	35-200	78.5	82.3	108	132
Flash Point (°C)	-40	13	12	28	43
Auto-ignition (°C)	~300	434	456	430	340
Heat of vap. @ 25°C (kJ/kg)	380-500	904	758	686.4	621
RVP (kPa)	65.0	13.8	9	3.3	1.1

Table 2: Fuel samples and their volumetric composition.

Fuel sample	G	E	IP	IB	IA
G	100%	-	-	-	-
E10	90%	10%	-	-	-
E10-IP5	85.5%	9.5%	5%	-	-
E10-IB5	85.5%	9.5%	-	5%	-
E10-IA5	85.5%	9.5%	-	-	5%
E20	80%	20%	-	-	-
E20-IP5	76%	19%	5%	-	-
E20-IB5	76%	19%	-	5%	-
E20-IA5	76%	19%	-	-	5%
E30	70%	30%	-	-	-
E30-IP5	66.5%	28.5%	5%	-	-
E30-IB5	66.5%	28.5%	-	5%	-
E30-IA5	66.5%	28.5%	-	-	5%

RVP, density, and distillation temperature measurements were performed according to the standard test method via equipment given in Table 3.

Table 3: Equipment, test method, and accuracy.

Measurement	Equipment	Method	Accuracy
Density	Mettler Toledo D4	EN ISO 3675	±0.0001 g/cm³
RVP	Herzog HVP 972	EN 13016	±0.2 kPa
Distillation	Herzog distillation analyzer	EN ISO 3405	±0.1 °C

RVP is a crucial fuel property for gasoline and other light-liquid petroleum products. The RVP is also an indicator of the front-end volatility of fuels [17]. It represents the absolute vapor pressure of the fuel at 37.8 °C and at a vapor-to-liquid ratio of 4:1. The higher the RVP, the more volatile the fuel, and vice versa. RVP is often used interchangeably with the fuel's dry vapor pressure equivalent (DVPE) [18]. DVPE is calculated based on the total vapor pressure of the fuel sample that was measured. The correlation equation for DVPE is provided below [5]:

$$DVPE\,(kPa) = (0.965\,P_{total})\text{-}3.78\,kPa \qquad (1)$$

Where P_{total} is the measured total vapor pressure in kPa. Equations 2 and 3 were used to calculate fuel samples' octane number and lower heating value, respectively.

$$ON_f = \sum_{i=1}^{3} x_i \rho_i ON_i / \sum_{i=1}^{3} x_i \rho_i \qquad (2)$$

Here, x, ρ, and ON are the volumetric ratio in the mixture, density, and octane number of the ith component, respectively.

$$LHV_f = \sum_{i=1}^{3} x_i \rho_i LHV_i / \sum_{i=1}^{3} x_i \rho_i \qquad (3)$$

Here, LHV_i is the lower heating value of the component in the mixture.

3. Results and Discussions

The results of the measurement RVP for gasoline and ethanol-gasoline blends are presented in Figure 1. The RVP increased as the ethanol content in the blend reached 10% but decreased with further increases in ethanol concentration. E10 and E20 led to higher RVP, while E30 exhibited a lower RVP than that of gasoline. This behavior was due to the formation of the azeotropic ethanol-gasoline mixture. This result aligns with previous findings [11,19], indicating that a higher vapor pressure in gasoline-ethanol blends is observed when ethanol content is between 10% and 30%, compared to neat gasoline. E10 yielded

the highest RVP with 63.2 kPa, whereas E30 offered the lowest with 60.9 kPa, even below that of gasoline. However, as seen in Figure 2, the RVP of all gasoline-ethanol mixtures was reduced by adding C3-C5 iso-alcohols. Specifically, considering E10, the RVP was decreased from 63.2 kPa to 61.2 kPa with the addition of isoamyl alcohol (E10-IA5). This value is 2 kPa and 1.3 kPa lower than the RVP of E10 and gasoline, respectively. Similarly, the RVP of E20 and E30 was reduced by adding C3-C5 iso-alcohols. Moreover, the RVP dropped even further when the added alcohol's chain length increased. This confirms that the hydroxyl group azeotropic effect is weakened as the carbon chain length increases [12]. Therefore, the lowest RVP of 58.9 kPa was measured for E30-IA5. More importantly, all fuels met the requirements of the EN 228 standard, which sets the RVP in the range of 45–60 (68) kPa for summer gasoline.
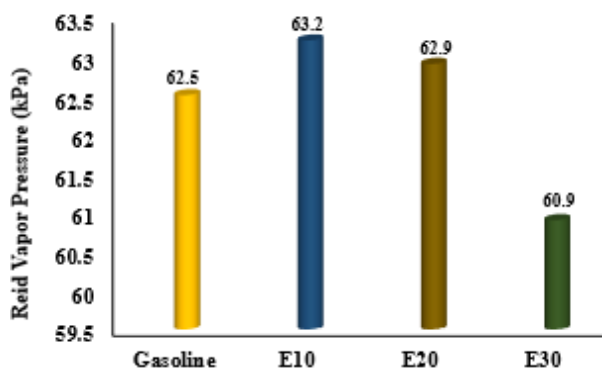

Figure 1. RVP of gasoline and ethanol-gasoline blends.

Adding C3-C5 iso-alcohol to ethanol-gasoline blends also affects other fuel properties. Thus, we determined the fuel samples' density, distillation temperature, lower heating value, and octane number. Figure 3 shows the measured density values for each fuel. The density of ethanol-gasoline blends was higher than that of gasoline, and it increased with the rise in ethanol fraction in the blend as ethanol has a higher density than gasoline. Furthermore, because C3-C5 iso-alcohols have a higher density than ethanol, adding them to ethanol-gasoline blends increased the density further, as expected. Therefore, the highest density of 763.6 kg/m^3 was measured for the E30-IA5. However, it was determined that the density values of all fuel samples were within the range (720-775 kg/m^3) specified in the EN 228 gasoline standard. The analysis shows that

the high density of iso-alcohols is a key factor limiting their incorporation into fuel blends. As a result, to comply with EN 228 density regulations, IA can be added to the E30 blend at a maximum volumetric ratio of 7%.
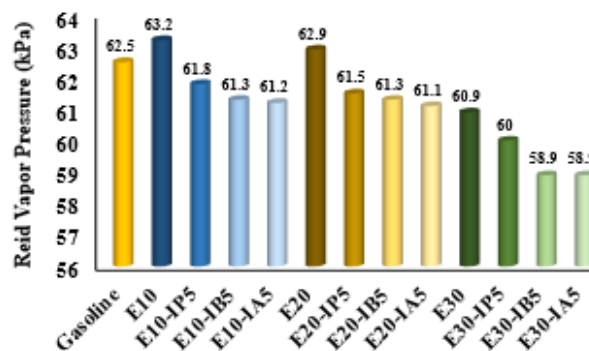
Figure 2. Effect of adding C3-C5 iso-alcohols on the vapor pressure of the ethanol-gasoline mixtures.
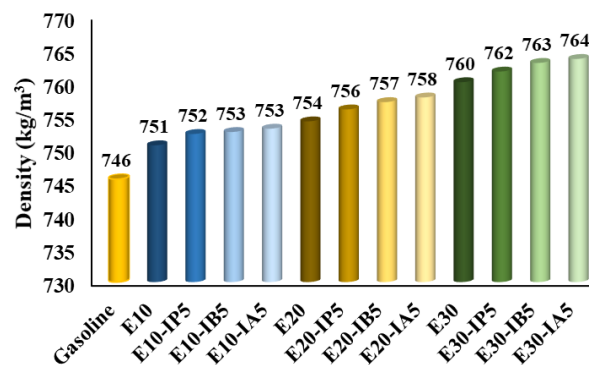
Figure 3. Density of fuel samples.

The lower heating values of fuel samples are given in Figure 4. Due to its oxygenated nature, ethanol has a heating value of 62% lower than gasoline. Therefore, the heating value of gasoline-ethanol mixtures was lower than that of gasoline, and the heating value decreased even more as the ethanol content in the mixture increased. Since C3-C5 iso-alcohols have a higher heating value than ethanol (see Table 1), the heating value of the fuel was increased by adding these alcohols to gasoline-ethanol mixtures. The heating value increases as the chain length of aliphatic alcohols increases [21]. Although the EN 288 gasoline specification does not regulate the lower heating value of engine fuels, a high heating value is a desired feature for engine fuels in terms of fuel economy and performance. Consequently, the addition of C3-C5 iso-alcohols not only reduced the vapor pressure but also increased the heating value of gasoline-ethanol mixtures, eventually reducing fuel consumption. This conclusion is

supported by the findings of Bharath and Selvan [22], who demonstrated that the increased fuel consumption associated with lower alcohols can be offset by incorporating higher alcohol additives.

The octane number is a fundamental fuel property for SI engines that characterizes fuel resistance to self-ignition. The higher the octane number, the lower the knock propensity. Figure 5 shows the octane number of fuel samples. Ethanol-gasoline blends and C3-C5 iso-alcohol-added fuels have slightly higher octane numbers than base gasoline. This is an expected result since C3-C5 iso-alcohols have a higher octane rating than gasoline (refer to Table 1). Thus, they offer high anti-knock performance [23]. With a slightly lower octane number than IP and IA, IB yielded only a slight increase or no change in the octane number of the ethanol-gasoline blends. However, IP and IA significantly improved the octane number. It is attributed to their molecular structures. Fuels with extensively branched carbon chains demonstrate enhanced resistance to knocking, leading to higher octane ratings [24]. The octane number analysis result aligns with the findings of Abdellatif et al. [25], who highlighted that isopropanol is a renewable octane booster with excellent physical and chemical properties.
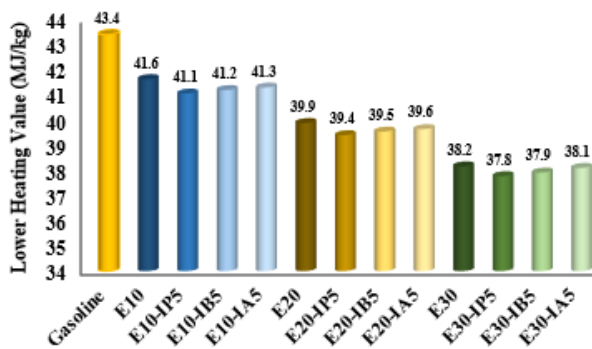
Figure 4: Lower heating value of fuel samples.

RVP is a key indicator of the volatility of the light fractions in gasoline. However, gasoline also contains high hydrocarbon fractions, whose volatility characteristics can be analyzed through distillation tests. Figure 6 displays the distillation curve of gasoline and ethanol-gasoline mixtures. Both gasoline and ethanol-gasoline blends exhibited almost the same distillation behavior from 5% to 30% distilled volume. However, their distillation curve remarkably differed beyond that point.
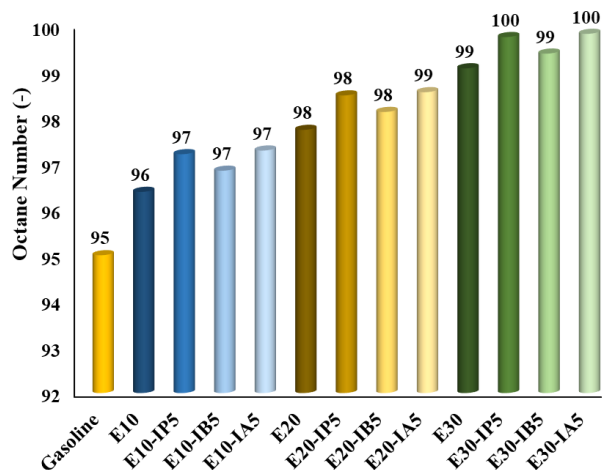
Figure 5: Octane number of fuel samples.

Specifically, the evaporating temperature of gasoline between 40% and 90% was affected by ethanol content. The main reason is that ethanol's boiling point temperature (78.5 °C) is close to the T50 (79.6 °C) and lower than the T90 (155.7 °C) distillation temperature of base gasoline. As the ethanol content in the mixture increases, the distillation curve of the fuel moves further away from the gasoline distillation curve. Similarly, Zhang et al. [26] observed that isobutanol significantly impacts gasoline's 50% evaporation temperature (T50). Such change is undesirable since it may negatively affect engine performance and fuel economy. Overall, ethanol addition to gasoline did not affect the front-end volatility (0-20 %, v/v), but it greatly impacted mid-range (20-80 %, v/v) and tail-end volatility (80-100 %, v/v). However, as seen in Figure 7, distillation curves improved when C3-C5 iso-alcohols with high boiling points were added to ethanol-gasoline mixtures. Among iso-alcohols investigated, isoamyl alcohol has the highest boiling point temperature compared to the others. Thus, it was superior to its counterparts in improving the distillation curve.
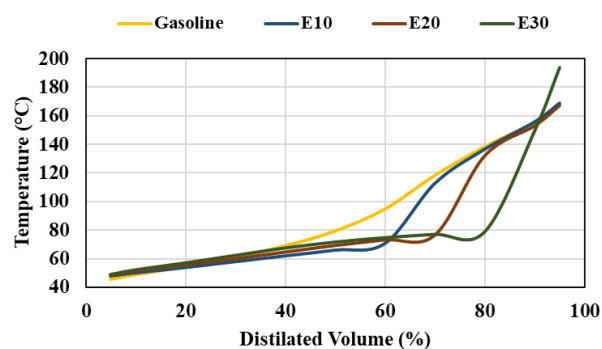
Figure 6: Distillation curve of gasoline and ethanol-gasoline mixtures.
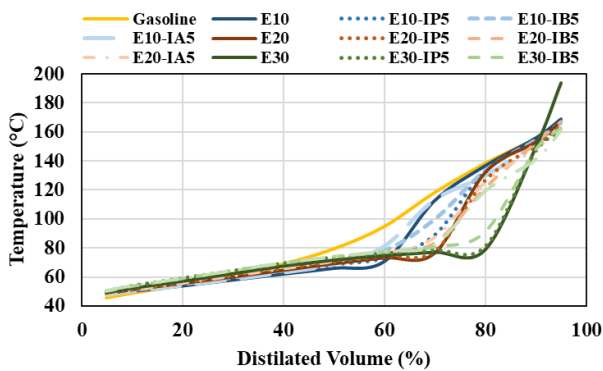
Figure 7: Distillation curve of fuel samples.

The distillation characteristics of the fuel samples were further investigated by analyzing changes in volatility, specifically in the E70, E100, and E150 distillation values. Table 4 lists the distillation values of fuel samples. They are initial boiling point (IBP) temperature in °C, final boiling point (FBP) temperature in °C, distillate fractions at specific temperatures, and residue (%,v/v). E70, E100, and E150 are the distilled volume fractions (%, v/v) at the temperature points of 70°C, 100°C, and 150°C, respectively. The volatility of fuel samples was evaluated considering the distillation values at the current minimum-maximum limits allowed by the EN 228 gasoline specification. The EN 228 regulation does not limit IBP, so the IBP row was colored yellow in Table 4. However, as specified in Table 4, it sets a range for E70 and E100 while limiting the minimum value of E150 and the maximum value of FBP and residue. All fuel samples meet the EN 228 regulation regarding E150, FBP, and residue values. However, some fuel samples exceeded the upper limit and did not comply with EN 228 regulations for E70 and E100 parameters. Due to the high volatility of the azeotropic ethanol-gasoline mixture, E10, E10-IP5, E10-IB5, E10-IA5, and E20 fuels yielded a high evaporated volume at 70°C. Fuel samples except for Gasoline, E10, and E10-IA5 exceeded the maximum limit for E100. The underlying reason for this outcome is the constant boiling point temperature of ethanol (≈78.5°C), which increased the evaporated volume at 100 °C. Since E10 constituted a lower ethanol fraction and E10-IA5 had the highest boiling point (132 °C) component (isoamyl alcohol), they met the E100 criteria. Isoamyl alcohol restricted the increase in volatility at 10% v/v ethanol fraction; however,

its effect weakened at higher ethanol fractions. However, ethanol (≈78.5°C), isopropanol (≈82.3°C), and isobutanol (≈108 °C) with boiling points closer to 100 °C caused the blends to exceed the maximum limit set for E100.

Table 4: Distillation values of fuel samples

	IBP	E70	E100	E150	FBP	Residue
Gasoline	36.4	41.5	63.4	87.6	189.2	1% v/v
E10	38.2	60.7	68.1	88.7	189.7	1% v/v
E10-IP5	39.4	53.7	72	89.2	188	1% v/v
E10-IB5	39.2	50.5	71.6	89.5	186.7	1% v/v
E10-IA5	38.8	52.3	66.7	89.7	186.7	1% v/v
E20	39.4	53.6	76.3	90.3	186.9	1% v/v
E20-IP5	38.2	49.2	78.7	90.7	185.5	1% v/v
E20-IB5	38.8	47	77.3	90.5	186.6	1% v/v
E20-IA5	37	48.4	73.2	91	187	1% v/v
E30	37.7	46.6	81.8	91.4	185.6	1% v/v
E30-IP5	39.5	41.4	83.5	91.6	186.1	1% v/v
E30-IB5	39.7	41.2	82.6	91.7	185.7	1% v/v
E30-IA5	39.5	41.2	78.4	92.3	186.6	1% v/v
EN 228 limit	-	22-50% v/v	46-71% v/v	Min. 75% v/v	Max. 210 °C	Max. 2% v/v

Fortunately, the efforts to upgrade EN 228 have been ongoing. For example, the European Automobile Manufacturers' Association (ACEA) members propose revising the current EN 228 regulation. That proposal introduces a carbon/hydrogen ratio limit to help reduce exhaust CO_2 and hydrocarbon (HC) emissions. Similarly, the proposal introduces a C9+ aromatics limit of 10% v/v and a C10+ aromatics limit of 2% v/v while retaining the total aromatics limits at 35% v/v to help reduce ultrafine particle emissions. The proposal lowers the minimum fuel density limit from 720 to 690 kg/m³ to reduce particulate matter (PM) emissions [27]. This proposal also offers new distillation points and extends the distillation range, as shown in Table 5.

Table 5. The gasoline distillation range outline proposed by ACEA [27].

	Unit	Current EN 228	Proposal
E50	% v/v, min	-	10.0
E100	% v/v, min	46.0	-
E130	% v/v, min	-	70.0
E150	% v/v, min	75.0	-
E170	% v/v, min	-	90.0

4. Conclusion

This study investigated the effects of adding C3-C5 iso-alcohols to ethanol-gasoline blends (E10, E20, and E30) on RVP and other fundamental fuel properties. The essential findings were summarized as follows:

1. E10 and E20 binary blends behaved like an azeotropic mixture, resulting in higher vapor pressure than gasoline and ethanol. However, adding C3-C5 iso-alcohols to ethanol-gasoline blends reduced RVP. The effectiveness of C3-C5 iso-alcohols in reducing RVP follows the order IA > IB > IP, which is related to their respective RVP values.

2. Dual-alcohol (E+C3/C4/C5)-gasoline blends offered enhanced density, heating value, and octane number.

3. Ethanol-gasoline blends resulted in a diverted distillation curve starting from 30% distilled volume compared to gasoline. However, adding C3-C5 alcohols to ethanol-gasoline blends slightly improved the fuel's distillation curve.

4. The determined fuel properties of all C3-C5 iso-alcohol-added ethanol-gasoline blends comply with EN 228 specifications except for some fuel samples' distilled volume at 70 °C (E70) and 100 °C (E100).

5. To comply with EN 228, gasoline regulation with maximum values of E70 and E100 can be relaxed, or the E228 regulation could be modified, including a higher ethanol fraction and C3-C5 alcohols.

6. Additionally, using higher alcohols in ethanol-gasoline blends may be advantageous in increasing the share of renewable/low-carbon fuel.

Although this study highlights a promising approach to reducing the vapor pressure of ethanol-gasoline blends, there are gaps in long-term fuel performance, compatibility with the engine, and broader environmental and economic assessments. Future research should address these limitations for a more complete analysis. Moreover, multi-alcohol blends should be investigated, and their type and concentration should be optimized.

Acknowledgments

CRediT authorship contribution statement

Nour Eddın BULBUL: Methodology, Investigation, Writing—Original Draft Preparation, Project Administration.
Abdülvahap ÇAKMAK: Conceptualization, Investigation, Formal Analysis, Writing—Review & Editing, Supervision.

Declaration of Competing Interest

The authors declare that they have no competing financial interests or personal relationships that could have appeared to influence the work reported in this paper.

Nomenclature

Abbreviations
C3   : Isopropyl alcohol
C4   : Isobutanol
C5   : Isoamyl alcohol
CO_2 : Carbon dioxide
DVPE : Dry vapor pressure equivalent
E   : Ethanol
E100   : Distillated vol. (%, v/v) at 100°C
E150   : Distillated vol. (%, v/v) at 150°C
E70   : Distillated vol. (%, v/v) at 70°C
EN 228: European Standards for Gasoline
FBP   : Final Boiling Point
G   : Gasoline
HC   : Hydrocarbon
IA   : Isoamyl Alcohol
IB   : Isobutanol
IBP   : Initial Boiling Point
IP   : Isopropanol
LHV   : Lover Heating Value
ON   : Octane Number
PM   : Particulate Number
RVP   : Reid Vapor Pressure
T50   : The temperature at which 50% of the fuel evaporates
T90   : The temperature at which 90% of the fuel evaporates

Symbols

ρ : Density (kg/m^3)
x : Volumetric fraction
Subscripts
f : Fuel
i : Fuel component

5. References

1. Malla FA, Bandh SA, Wani SA, Hoang AT, Sofi NA., "Biofuels: Potential Alternatives to Fossil Fuels BT - Biofuels in Circular Economy", In: Bandh SA, Malla FA, editors., Singapore: Springer Nature Singapore, p. 1–15, 2022. https://doi.org/10.1007/978-981-19-5837-3_1.

2. Çakmak A., "Improvement of exhaust emissions in a diesel engine with the addition of an oxygenated additive to diesel-biodiesel blends", Energetika, 68:79–90, 2022. https://doi.org/https://doi.org/10.6001/energetika.v68i1.4859.

3. Prasad S, Yadav KK, Kumar S, Pandita P, Bhutto JK, Alreshidi MA, et al., "Review on biofuel production: Sustainable development scenario, environment, and climate change perspectives − A sustainable approach", Journal of Environmental Chemical Engineering, 12:111996, 2024. https://doi.org/https://doi.org/10.1016/j.jece.2024.111996.

4. Pałuchowska M, St\kepień Z, Żak G., "The prospects for the use of ethanol as a fuel component and its potential in the reduction of exhaust emissions", Combust Engines, 53:80–92, 2014.

5. Gaspar DJ, Phillips SD, Polikarpov E, Albrecht KO, Jones SB, George A, et al., "Measuring and predicting the vapor pressure of gasoline containing oxygenates", Fuel, 243:630–44, 2019. https://doi.org/https://doi.org/10.1016/j.fuel.2019.01.137.

6. Andersen VF, Anderson JE, Wallington TJ, Mueller SA, Nielsen OJ., "Vapor Pressures of Alcohol−Gasoline Blends", Energy & Fuels, 24:3647–54, 2010. https://doi.org/10.1021/ef100254w.

7. Çakmak A, Özcan H., "Benzin İçin Oksijenli Yakıt Katkıları", Politek Dergisi, 21:831–40, 2018. https://doi.org/10.2339/politeknik.457956.

8. Gershon O, Asaolu K., "Evaporative quality of Nigeria's gasoline: truck loading perspective", Energy, Ecology and Environment, 6:307–15, 2021. https://doi.org/10.1007/s40974-020-00184-0.

9. Amine M, Barakat Y., "Effect of cyclohexanol on phase stability and volatility behavior of hydrous ethanol-gasoline blends", Egyptian Journal of Petroleum, 30:7–12, 2021. https://doi.org/https://doi.org/10.1016/j.ejpe.2021.04.001.

10. Awad OI, Zhou B, Chen Z, Kadirgama K, Mohammed MN, Ramasamy D., "Influence of PODE1 additive into ethanol-gasoline blends (E10) on fuel properties and phase stability", Heliyon, 9, 2023. https://doi.org/10.1016/j.heliyon.2023.e22364

11. Dash N, Tamilvendan D., "Effective Utilization of Ethanol-Blended Motor Gasoline by Addition of Co-solvent Isopropanol", Transactions of the Indian National Academy of Engineering, 8:379–87, 2023. https://doi.org/10.1007/s41403-023-00404-z.

12. Aghahossein Shirazi S, Abdollahipoor B, Martinson J, Windom B, Foust TD, Reardon KF., "Effects of dual-alcohol gasoline blends on physiochemical properties and volatility behavior", Fuel, 252:542–52, 2019. https://doi.org/https://doi.org/10.1016/j.fuel.2019.04.105.

13. Gong J, Cai J, Tang C., "A comparative study of emission characteristics of propanol isomers/gasoline blends combined with EGR", SAE International Journal of Fuels and Lubricants, 7:200–6, 2014.

14. Li D, Yu X, Guo Z, Zhang J, Wang T, Li Y., "Effects of isopropanol ratio at different excess air ratios on combustion and emissions characteristics of an isopropanol/gasoline dual-fuel combined injection SI engine", Fuel, 333:126507, 2023. https://doi.org/https://doi.org/10.1016/j.fuel.2022.126507.

15. Yusoff MNAM, Zulkifli NWM, Masjuki HH, Harith MH, Syahir AZ, Kalam MA, et al., "Performance and emission characteristics of a spark ignition engine fuelled with butanol isomer-gasoline blends", Transportation Research Part D: Transport and Environment, 57:23–38, 2017. https://doi.org/https://doi.org/10.1016/j.trd.20

17.09.004.

16. Yadav PS, Gautam R, Le TT, Khandelwal N, Le AT, Hoang AT., "A comprehensive analysis of energy, exergy, performance, and emissions of a spark-ignition engine running on blends of gasoline, ethanol, and isoamyl alcohol", Energy, 307:132548, 2024. https://doi.org/https://doi.org/10.1016/j.energy.2024.132548.

17. Coker AK., "Petroleum, Complex-Mixture Fractionation, Gas Processing, Dehydration, Hydrocarbon Absorption and Stripping: Part 2: Fractionation", Ludwig's Applied Process Design for Chemical and Petrochemical Plants, 269–344, 2010.

18. McCormick RL, Ratcliff MA, Christensen E, Fouts L, Luecke J, Chupka GM, et al., "Properties of Oxygenates Found in Upgraded Biomass Pyrolysis Oil as Components of Spark and Compression Ignition Engine Fuels", Energy & Fuels, 29:2453–61, 2015. https://doi.org/10.1021/ef502893g.

19. Calvin YL, Hariyanto PAT, Usman AI, Masuku M, Wibowo CS, Maymuchar, et al., "Volatility and physicochemical properties of gasoline-ethanol blends with gasoline RON-based 88, 90, and 92", Fuel, 307:121850, 2022. https://doi.org/https://doi.org/10.1016/j.fuel.2021.121850.

20. Gandolfo J, Lawler B, Gainey B., "Experimental study of high compression ratio spark ignition with ethanol, ethanol–water blends, and methanol", Fuel, 375:132528, 2024. https://doi.org/https://doi.org/10.1016/j.fuel.2024.132528.

21. Altun Ş, Adin MŞ, İlçin K., "Monohydric aliphatic alcohols as liquid fuels for using in internal combustion engines: A review", Proceedings of the Institution of Mechanical Engineers, Part E: Journal of Process Mechanical Engineering, 09544089231160472, 2023. https://doi.org/10.1177/09544089231160472.

22. Bharath BK, Arul Mozhi Selvan V., "Influence of Higher Alcohol Additives in Methanol–Gasoline Blends on the Performance and Emissions of an Unmodified Automotive SI Engine: A Review", Arabian Journal for Science and Engineering, 46:7057–85, 2021. https://doi.org/10.1007/s13369-021-05408-x.

23. Shirazi SA, Abdollahipoor B, Windom B, Reardon KF, Foust TD., "Effects of blending C3-C4 alcohols on motor gasoline properties and performance of spark ignition engines: A review", Fuel Processing Technology, 197:106194, 2020. https://doi.org/https://doi.org/10.1016/j.fuproc.2019.106194.

24. Olalere RK, Zhang G, Liu H, Ma X, Xu H., "Experimental study of combustion and emissions characteristics of low blend ratio of 2-methylfuran/ 2-methyltetrahyrofuran with gasoline in a DISI engine", Fuel, 382:133799, 2025. https://doi.org/https://doi.org/10.1016/j.fuel.2024.133799.

25. Abdellatief TMM, Ershov MA, Makhmudova AE, Kapustin VM, Makhova UA, Klimov NA, et al., "Novel variants conceptional technology to produce eco-friendly sustainable high octane-gasoline biofuel based on renewable gasoline component", Fuel, 366:131400, 2024. https://doi.org/https://doi.org/10.1016/j.fuel.2024.131400.

26. The members of the European Automobile Manufacturers Association, "ACEA Positiom Paper Revision of the Fuel Quality Directive (FQD)", 2022.
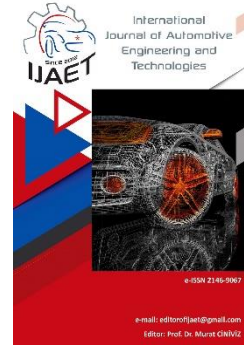
Original Research Article

Combustion of emulsified and non-emulsified biofuels

Sahaj Parkash [1] and Sam M. Dakka [2, *]

[1, 2 *] Department of Mechanical, Materials and manufacturing Engineering, University of Nottingham, Campus Park, NG7 2RD United Kingdom.

ARTICLE INFO

ABSTRACT

Greener aviation and automotive industry are needed in the fight against climate change. Targets set out by key organizations call for emissions to be reduced. Biofuels present an innovative route to achieving such targets. The goal of this study is to investigate a sunflower oil-based biofuel in its non-emulsified and emulsified form. The aim is to create an experimental setup that can be used to carry out simple droplet combustion experiments, capable of igniting biofuel droplets. In addition to providing an understanding of emulsified and non-emulsified biofuels. The methodology outlines how a literature review was conducted to investigate the current experimental setup, which was used to help design a simple low cost set up for this research undertaking. The methodology also states that by analyzing the behavior and data collected during the testing phase, an insight into the behavior of such biofuels is obtained. The key parameters to be measured were the ignition delay times, the total combustion time period and the ignition temperatures. The observation of any phenomena was also to be noted. The results showed that ignition temperatures, ignition time delays and the total combustion time for an emulsified sunflower oil droplet are significantly lower compared to non-emulsified sunflower oil droplet. This is because of the presence of water in the emulsion which lowers the boiling temperature, enables phenomena such a micro-explosion and puffing to occur easily. As a result of such phenomena occurring, an improved and efficient combustion is completed. The impact of this work shows that by emulsifying biofuels in the form of vegetable oils, their properties to be used as a fuel are improved. There is great potential for use in the aviation sector with more research to be conducted on the emulsification of droplets.

Keywords: Micro-explosion, Alternative fuels, Sunflower oil, Emulsified Biofuels.

1. Introduction

As a result of the growing threat from climate change, the aviation industry has been challenged to reduce the environmental impact

it creates. ACARE (Advisory Council for Aviation Research and Innovation in Europe) have outlined Flightpath Goals for 2050 which include: a 75% reduction in CO_2 emissions per passenger kilometer and 90% reduction in NOx emissions. [1]

Biofuels present an innovative opportunity that can be utilized to pursue a greener aviation industry. The European Commission 2050 report recognizes this, stating that the ability to generate liquid fuels and energy is a critical segment of the energy supply needed for the future. [2]

Biofuels in the form of non-emulsified and emulsified sunflower oil will be investigated in this project. Biofuels can be produced from a range of vegetable oils. One of the reasons why sunflower oil was selected is because of the potential it has shown in various studies, which suggests it could play a role in the new generation of innovative biofuels technology. [1, 2].

The water-in-oil emulsification of sunflower oil was chosen as it is a simple approach in making biofuel. The combustion characteristics of the emulsified biofuel were investigated to provide an insight into how emulsification could be used in further research to improve the combustion performance.

To complete the aims, three key stages were carried out. The primary stage involves the completion of a literature review. This determines the type of vegetable oil to be used. The literature review also reviews current experimental setups used.

Following the literature review, the secondary stage involves designing a simple low-cost combustion setup that could be used. Key components such as heating elements are tested, once final modifications are complete, the next steps are taken. Once the setup is constructed, testing of the droplets can begin.

The final phase involves carrying out experiments and accumulating results. Once accumulated, they are analyzed and presented to provide a greater understanding of the combustion of emulsified and non-emulsified sunflower oil.

2. Literature Review
2.1. Use of biofuels in aviation & automotive

Biofuels present a golden opportunity that can be investigated in the race to make a greener aviation and automotive industry, as recognized by The European Commission 2050 report. However, along with the great potential brought by biofuels there are some challenges that need to be addressed. [1]

Given that biofuels are derived from renewable sources their total carbon footprint is lower than the fossil fuel based equivalent. This is one of the main driving factors in pushing the industry towards biofuels [2-5]. However, according to Gegg et al. other driving factors include the constant threat of volatile oil prices, future carbon tax prices, energy security and the requirement for fuel that compatible with the current engines and available infrastructure. [2]

Not only are biofuels able to provide part of the solution to the concerns listed above, but they have also shown their ability to improve aspects of engine performance. Mazlan et al. investigated the effects via simulation on a two-spool engine between kerosene and biofuels. The type of biofuels tested were Bio Synthetic paraffinic Kerosene and Camelina Bio Synthetic Paraffinic. The results obtained clearly show an increase in engine thrust and a reduction as well in the amount of fuel consumed. The trend was linearly observed as the percentage of biofuel in the kerosene increased.[6]

Similarly, an investigation on a three-shaft engine similar to the RB211 - 524 carried out by Azami et al. incorporated computer software simulation, to analyze a group of biofuels used in flight tests. The biofuels were a blend of kerosene and Jatropha Biofuel and a blend of Kerosene and Cameline Biofuel. Positive results were obtained, which showed enhanced gross and net thrust. The results also showed better fuel flow and lower specific fuel consumption. Similarly to Mazlan et al. as the percentage of biofuel increased there was a linear change in the positive results. [7]

This demonstrated the potential that with further research and understanding, biofuels would be able to bring a further increase in engine performance.

However, in order to reap the benefits of biofuels there are some hurdles that need to be overcome. One of the concerns involves the infrastructure, as a European Commission environment report highlighted the European production of

biofuels for aviation relies on a small number of manufacturing plants. The biofuels produced by those plants equate to 5% of the aviation fossil fuel demand. This infrastructure concerns is also echoed by Prussi et al. who states that currently European biofuel industry is catered more for the road transportation market [3, 5].

Although European countries will need to address this, other countries may be able to provide more biofuel to help supply demand. For example, Cortez et al stated that due to the previous Brazilian experience in biofuels and the development of air transportation within the country, it presents a positive case for considering high production of biofuels [8].

Another key issue outlined by the European Commission and Wang et al is the cost of biofuels. The feedstock price and its volatility could create a supply issue. The European Commission stated that the price for aviation fossil fuel is €600 per ton, whilst certain biofuels could range from €950 to €1015 per ton. Wang et al also stated that one of the factors restricting biofuels to reach a commercial level is the high capital costs required [3, 4]. These are complex issues that need to be addressed on multiple levels. For example, partially addressing the cost issue, governments could be motivated to introduce subsidies for biofuels in exchange for more carbon tax credits.

2.2. Sunflower Oil

The biofuel emulsified and non-emulsified droplets in this study will use sunflower oil. This section will outline some of the characteristics of vegetable oils and sunflower oils in general. In general, there are many incentives to use vegetable oil to produce biofuels as they are: a renewable source of energy, widely available, biodegradable and has a low Sulphur content. With reference to sunflower crops, it has an efficient rooting system that allows it to make the most of the natural supplies of soil nitrogen and soil moisture. In addition to this, sunflower crops do not require lots of effort to cultivate. The crop is also able to provide economic output as an edible and non-edible resource [9 - 11].

Furthermore, Requena et al. conducted a comparative review of rapeseed, soybean and sunflower oil. They found that although sunflower crops require the most land use out of three, they have the most positive contribution to reduction of carbon dioxide. Due to the amount of carbon dioxide consumed by the plant [12]. After reviewing these sources, there is strong positive case to pursue further research and understanding into sunflower based oils.

Sunflower oil has already shown positive results in the automotive industry, where it has been blended and used with diesel to create Biodiesel. An investigation carried out by Hemanandh et al. tested the emissions and performance of a diesel engine. A hydro-treated refined sunflower oil was used to create the biodiesel. The investigation altered the loads, speed and blends of the hydro-treated refined sunflower oil. The results showed that emission such as Carbon Monoxide and Nitric Oxide were reduced, when the biodiesel was used. In addition to this, the brake thermal efficiency increased, and the brake specific fuel consumption decreased when the biodiesel was used [13].

Similarly, Amini-Nikai et al. compared the fuel and emission properties of sunflower based biodiesel and standard diesel fuel. Overall, the results showed that biodiesel had positive combustion characteristics, and a lower amount of pollution compared with regular diesel [14].

When analyzing the two investigations, it is clear that there are both performance and emission-based benefits to the diesel engine when the biodiesel is incorporated. The challenge would be to ensure that the same effects can be achieved or extrapolated for jet engines.

In order for sunflower crops to be used widely in the aviation industry they may need to utilize a technological boost. An analysis into the chemical properties of cultivated sunflower and silverleaf sunflower showed promising ability. The results showed that both types of sunflower crops hold the organic composition, that can be used to help form a better sunflower biofuel crop. The ideal crop could be formed from the two samples; it would have a higher biomass and more cellulose [15]. After reviewing the investigation, there is potential for bioengineering to provide an enhanced solution, however more research is needed.

An alternative to creating a new crop is adjusting the process that creates the biofuel. Zhao et al. has shown it is possible to convert sunflower residual waste to a bio jet fuel using a ZSM-5 catalyst. However, the conversion rate was relatively low at 30.1% as a result more refining steps were required [16]. Despite this, there were encouraging signs from both investigations that showed sunflowers can be used as bio-jet fuel. Additionally, future improvements in both methods would provide a better yield/conversation rate. Improvement is achievable given the results outcome and funding that is available. As a result, sunflower oil was chosen as the first-choice biofuel to be used in the study. As it is seen as a future aviation biofuel that will be needed to diversify the sources of fuel and biofuels.

2.3. Experiment setups used to carry out droplet combustion

This section will analyze and compare setups, to review which features would be compatible for the scope of this project.
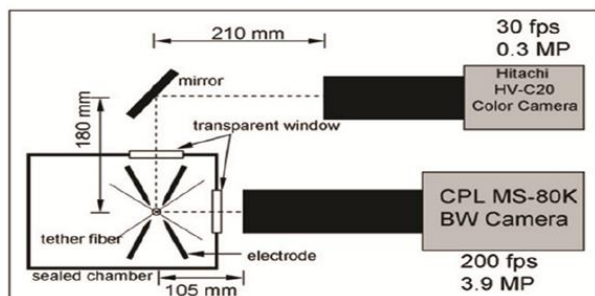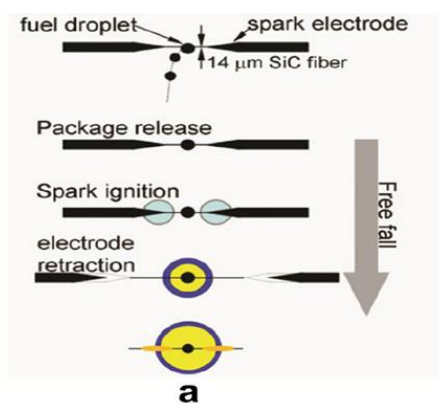

Fig. 1. Spark Electrode Experimental Setup [20]

One of the most popular experimental setups, used by Liu et al, makes use of four spark electrodes as shown in Figure 1. The spark electrodes are arranged in the shape of the letter 'X', poised to intersect on the Silicon Carbide fiber, also shaped in the form of the letter 'X'. The droplet is placed on the center of the fiber intersection typically using a piezoelectric generator. A piezoelectric droplet generator allows droplets to be created around 0.5mm in diameter. After the spark electrodes ignite the fuel droplet, they retract. The droplet goes into free fall and the behavior is measured by two cameras. The images recorded by the camera are then used to assess the droplet burning history [17 - 20].

This type of experimental setup involving spark electrodes seems much simpler than the one described by Ma et al, where a hydrocarbon fuel droplet was combusted in sub and super critical environments [21]. This type of setup required a lot more equipment as shown by figure 2 Analysis of the three experimental set ups discussed [19, 21, 22], show similar camera placement. For optimal images, the camera should record parallel or perpendicular views of the droplet combustion.
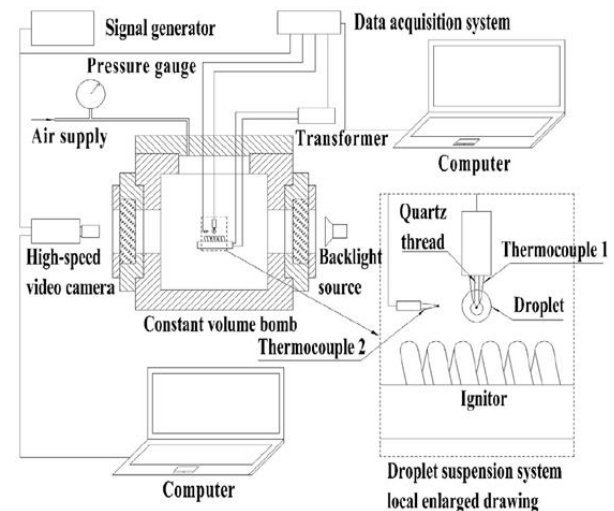
Fig. 2 Experimental setup [22]

However, when reviewing the two setups and the subsequent data, it is clear that elements of both setups could be useful for this study. The more popular method uses a piezoelectric droplet generator, which ensures consistency with the droplet size and shape for this project. Whereas the ignition method used by Ma et al and Liu et al. [19, 21], is a simpler and cheaper way of igniting the fuel droplet.

A droplet combustion method used by Rasid et al, is shown in Figure 3.

This method uses a boss, clamp and stand to hold the droplet and ignition source in a fixed position [22]. When comparing this experimental setup to the setup used Liu et al,

it becomes clear that a sealed chamber is not a necessity for experiment setup that can be conducted at room temperature under atmospheric pressure conditions.
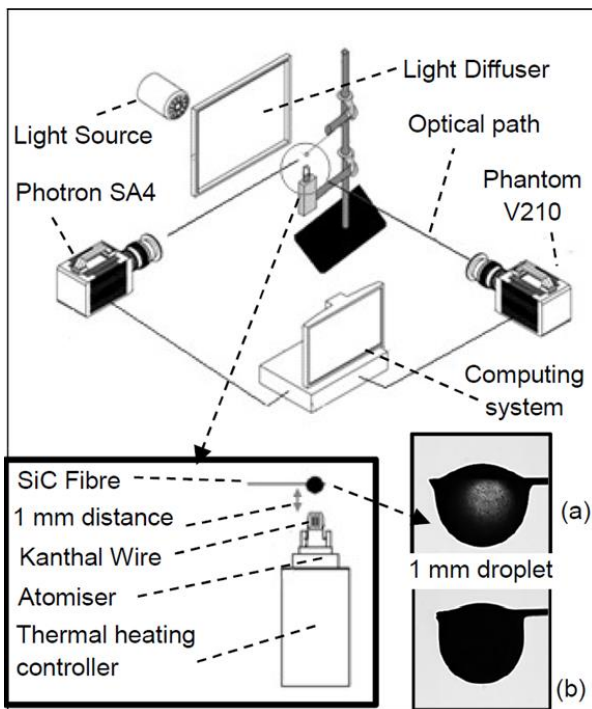
Fig. 3 Rasid et al experimental setup [2]

When analyzing the setups by Rasid et al and Ma et al [21, 22], the former uses a Kanthal Wire and a thermal heating atomizer to ignite the fuel droplet. This methodology is similar but simpler setup compared to Ma et al's. In this study, we utilized a Kanthal wire that's connected to a variable power pack. This experimental design would be a hybrid design of the two and would allow the heating element temperature to be controlled. This provides better control of the ignition temperatures.

Analysis of the three experimental set ups discussed [19, 21, 22], show similar camera placement. For optimal images, the camera should record parallel or perpendicular views of the droplet combustion.

2.4. Key Measurements and observation
2.4.1 Time – ignition delay

Reham et al's reserach on biofuel emulsions states ignition delay happens because of the water content in the fuel or emulsified fuel [23]. Debnath et al and Ithnin et al have shown agreement in stating ignition delay and micro explosion correlate to an improvement in the combustion efficiency for fuels which have been emulsified. In the investigation carried

out by Ithnin et al which analyzed the water in diesel emulsion fuels, against standard diesel fuel. The results showed an increase in thermal efficiency [24, 25]. Although the project scope does not cover analyzing the emissions, the delay times recorded ignition can be used to determine such effects in future work. Reham et al also states that the ignition delay of a biofuel emulsion can reduce the peak pressure at the lower loads. In addition to this it can also increase the heat release rate [23]. Reham et al and Liang et al find that in order to reduce the ignition time, oxygen concertation should be increased [23, 26]. This suggests although a longer ignition delay may not always be advantageous the ideal ignition time can be created by varying the oxygen concentration which can be useful.

The method employed by Kim et al to measure the ignition time is quite simple. Essentially an ignition point is set, in the examples of Kim et al a yellow flame was chosen. Then calculation of the time from the start of the experiment till that point, which equals the ignition delay [27, 28]. After reviewing the experimental setup and the implementation procedure, this task could be done manually using a stopwatch or by setting a timer on the high-speed cameras.

2.4.2 Thermal measurement and observation

In the investigation carried out by Ma et al and Rasid et al the key thermal measurements made were only based on the droplet temperature. However, in other more complex investigations the key temperatures noted included the air temperature within the chamber, or the temperature of the waterbed used to prevent excessive heating. This shows temperatures recorded would vary depending on the setup. In Hyemin et al's paper on combustion of an emulsion droplet in a rapid compressing machine was the only paper that really mentioned flame temperature, even though nothing numerical was specified it was briefly discussed. Across the four papers the flame behavior and image were more heavily discussed than the temperature [21, 22, 28, 29]. From analyzing the papers, it seems essential to record the droplet temperature in order to analyze its thermal behavior. In this study the droplet tetmperature will depict how the rate of temperature is affected by the biofuel emulsion

in comparison with the non-emulsified fuel.

2.4.3 Visual observation

An investigation carried out by Avulapati et al was based on diesel-biodiesel-ethanol blends. The combustion analysis showed through the use of a series of images how the flame and droplet varied. For example, it depicted images of smooth burning, puffing and explosion. Puffing refers to when vapor is released from a section of the droplet [30]. Similar to Avulapati et al, all droplet combustion experiments utilize cameras to take pictures of the droplet combusting. This is mainly due to the short combustion time of the droplets tested [22, 28-28]. It is clear that the droplet shape is a key part of assessing behavior.

Liu et al and Khan et al show images that can be used to find the diameter of the droplet [29, 31]. Whilst Hyemin uses a scale provided on the image to find the diameter, Liu et al utilized a software called 'Image Pro v6.3', which digitally measures the diameter [19, 29]. It is clear the digital measurement is more appealing as the accuracy is greater than using a scale provided.

3. Methodology

This study aims to measure the combustion characteristics of the emulsified and non-emulsified biofuels. The experimental phase formed a major part of the study.

Key measurements were identified and accurately recorded. It was important to ensure the methods employed to record the measurements allowed repeatability.

In addition to this, an equally important aspect of the study was creating a low-cost simple experimental setup. The success of the study was heavily determined by the ability of the experimental setup to deliver combustion results.

During the initial phases of the study, an experimental setup was devised. Given that the study was not based on previous research for a customer. An experimental setup was formed by reviewing the literature and it was driven by the budget and time constraints of the resources. For example, by reviewing Rasid et al [22], it was clear combustion droplets experiments do not have to be carried out in a sealed chamber, if there are no pressure or elevated temperature requirements. Given there is no such pressure and temperature required, an open setup was employed. A sealed chamber would also increase costs that cannot be justified. Therefore, the use of a boss, clamp and stand shown by Rasid et al [22] was employed. This setup allows the droplet to hold secured at a specific height. As shown by Liu et al [19] the droplet can be formed on a silicon carbide fiber wire. However, when analyzing this type of setup to hold the droplet and prevent it from being outside the field view of the camera, it became apparent that the experimental setup could have been further advanced. For example, instead of using a silicon carbide wire, a beaded thermocouple wire can be used. Onto which a droplet is deposited. The additional benefit of this approach is that a contact temperature can be recorded of the droplet throughout the combustion process.
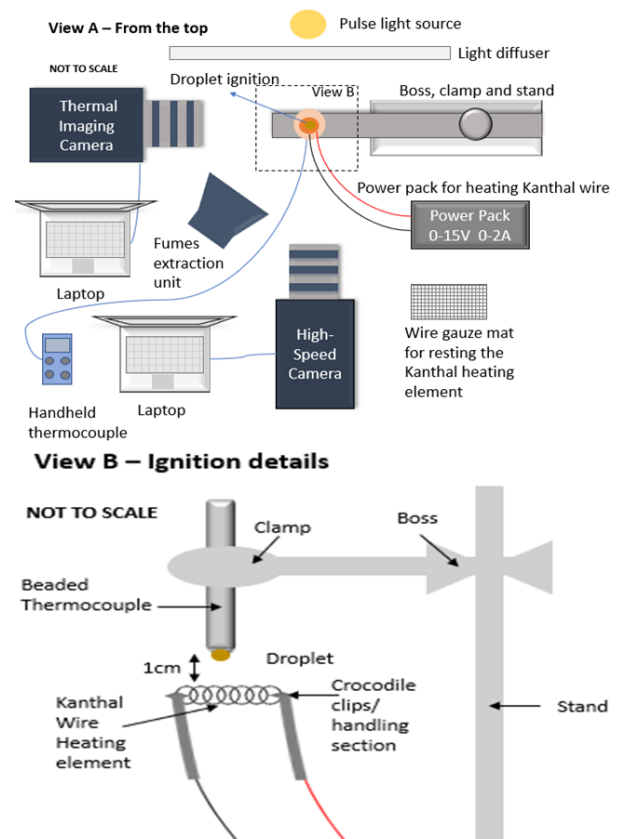

Fig. 4 Initial Experimental Setup Design

With regards to the heating aspect of the experimental setup. As shown by Liu et al and Ma et al [19, 21], there are two effective ways of igniting the fuel droplet. The spark electrode method is effective as the retractability after

ignition is advantageous. As any thermal imaging camera and thermocouples are not affected by the constant heat source. The use of a heat source using a wire shown by Rasid et al [22] is cheaper in comparison to the spark electrodes. Also, by adjusting the current and voltage the temperature can be altered, giving more control over ignition. However, a negative aspect was that the heating element was in a fixed condition. The heating design initially chosen involved using a wire heating element in the form of a Kanthal wire. However, a small piece of this wire was purchased to test the capability. Unfortunately, the kanthal wire couldn't ignite the sunflower oil droplet (this was accounted for in the planning and the setup was modified), due to the higher ignition temperatures. However, the Kanthal wire method could be used in the future for other vegetable oils with lower ignition temperatures. A butane gas burner was employed as it was more portable and able to easily reach the ignition temperatures of the sunflower oil. Although Figure 5, shows two butane burners, one was sufficient to carry out the experiment. Two can be used to allow for better image quality as the horizontal forces acting on the droplet cancel out.

In terms of the methods employed to time and record the droplet combustion stages, a review of current literature showed Rasid et al, Ma et al and Liu et al, as well as many others [19, 21, 22] all use software in combination with the high-speed camera for timing aspect. It was also noted that thermal imaging cameras and a high-speed camera were utilized to record the behavior and timeline of events. For this study a similar method was employed. A high-speed camera was used, the high-speed camera was positioned at right angle to the droplet, in order to record High quality images of the combustion. A digital stopwatch was placed in view of a standard camera which allowed the time to be measured.

The method employed by Liu et al and others [17-20] to deposit the droplet involves the use of a piezoelectric droplet generator. This was able to consistently create a small droplet. Due to the high cost of this, it was not feasible for the study. Therefore, a syringe was used to create droplets of 1.0mm ± 0.5mm.

In order to make the most appropriate and descriptive measurements and observations with the given time and budget constraints current papers were reviewed [18, 19, 21-31]. The two mains aspects that were measured included the time and temperatures. In addition to this, visual observations will need to be made of the images and recordings. These will provide a comprehensive description of the combustion experiment.
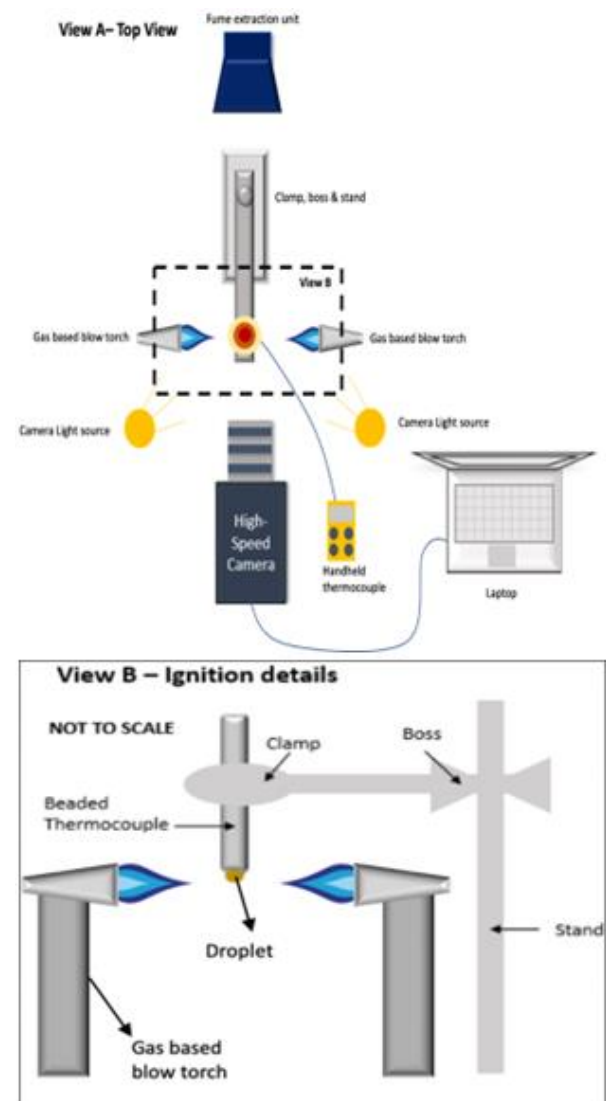
Fig. 5 Final Experimental Setup Design

The homogenization procedure used to emulsify the oil and water was based on the method of ultrasonication. Ultrasonication is the application of high frequency vibration implemented via sonotrode in order to reduce the interfacial tension between two immiscible liquids of an emulsion. Emulsified water in oil droplet samples were drawn from emulsification process which was optimized for stability enhancement and the experimental

apparatus is described in details in Sahota and Dakka [32] The composition of the emulsion, i.e., the percentage by mass of oil and water used, was chosen based on the recommendation of Mura, et al. [33], who tested the ignition properties of water in sunflower oil emulsions and suggested that this composition, 60% sunflower oil, 30% water and 10% surfactant per mass produces finely dispersed emulsions.

3.1 Experimental method and repeatability

The method of testing needed to ensure repeatability, and this was considered in simplifying the final design. Once the clamp, boss and stand are set up and the high-speed camera and fume extraction are positioned correctly, the biofuel droplet is deposited onto the beaded thermocouple. The syringe has volume markers along its length which are used to ensure the same droplet size is formed each time. The butane burner is ignited and positioned at a measured distance from the droplet and then the flame is slowly rotated, and ignition commences. Maintaining a constant distance is essential to ensure repeatability. In the experiments conducted the distance was 15cm. This was captured by the high-speed camera. A stopwatch is triggered once the flame starts to heat up the droplet to record the time period.

3.2 Assessments, requirements and assumptions

Throughout the experiment the key parameters that were recorded and assessed were the droplet temperature, time period, ignition delay time and the visual behavior of the emulsified and non-emulsified droplets.

The key requirements defined at the start of the project were to create and provide a framework that can be used to carry out simple droplet combustion experiments. In addition to providing an understanding into emulsified/non- emulsified biofuels.

By creating a working experimental setup that is able to record data, the first requirement was met. The assumptions made were, that the droplet size is constant, and the flame temperature of the butane gas burner is constant. The effect of the suspension heat transfer into the droplet is negligible.

The data recorded for the non-emulsified and emulsified biofuel included: Ignition delay time, Total combustion time and Ignition temperature. In total there were 6 sets of data. A statistical method was used to calculate the means for a 95% confidence level.

The equations used were:

$$\mu = M \pm Z \sqrt{\frac{s}{n}} \qquad (1)$$

Where μ = Population means, M = Sample means, Z = Z statistics determined by confidence level, s = standard deviation and n = sample size.

Table 1: Population Means for 95% Confidence Level

Data Set	μ	M	Z	s	n
NE 1	6.74 ± 0.1432	6.74	1.96	0.31	18
NE 2	9.66 ± 0.2864	9.66	1.96	0.62	18
NE 3	446.89 ± 7.6548	446.89	1.96	16.57	18
E1	2.12 ± 0.064	2.12	1.96	0.16	24
E2	3.45 ± 0.144	3.45	19.6	0.36	24
E3	114.02 ± 5.6171	114.02	1.96	14.04	24

In the left-hand column NE = Non-Emulsified Biofuel, E= Emulsified Biofuel, 1 = Ignition Delay, 2 =Combustion Time Period and 3 = Ignition Temperature.

Overall, when analyzing the table, the population mean range is low therefore there is high confidence in the method.

4. Results and Discussion

The second key aim of the study was to provide an understanding of emulsified/non-emulsified biofuels. This will be done in this section by analyzing the behavior and data collected during the testing phase. Given that the experimental setup was made with a low cost and simplicity in mind, the results retrieved are elementary at this phase. However, they do show some key areas which will be explored in this section. In future work, given that a setup has been established more advanced measurements and data could be collected.

The results recorded the time taken to complete the combustion cycle; the time taken to ignite the droplet from the moment heat is

applied – referred to as ignition delay. Lastly the ignition temperatures were recorded. Visual observations were also made. These parameters will now be explored. A key point to note is that the sample sizes for the two types of biofuels were different as shown by the methodology. For comparison purposes only the most important 18 datasets from the non-emulsified fuel were included. Corresponding sample numbers from each biofuel set do not have any meaning.

The ignition times and the total combustion times shown in Figure 6 illustrate the key difference between the emulsified and non-emulsified biofuels. The emulsified fuel has a lower ignition delay time and a lower total combustion time. In addition to this, it can be seen that the gaps between the two sets of line show that the non-emulsified fuel has a slow combustion phase after ignition. This suggests that pure sunflower oil, which is the non-emulsified biofuel essentially takes a long time to burn. As a result, the emulsified fuel burns faster and quicker. When analyzing figure 7 it becomes clearer as to why this is the case.
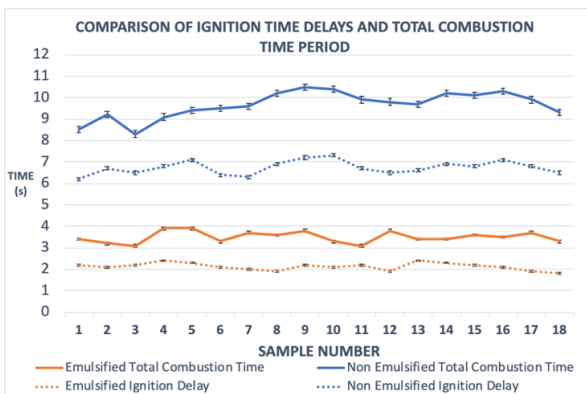

Fig. 6 Graph comparing the ignition and total combustion time for both types of biofuels

Ignition temperature naturally affects the ignition time delay which impacts figure 7 Figure 7 shows that the ignition temperatures for the emulsified fuel are significantly lower compared to the non-emulsified fuel. Figure 6 and Figure 7 both correlate with each other. They show the lower the ignition temperature the lower the ignition delay time, which is in line with what's expected. The large difference in temperature shown in Figure 7 accounts for the significant difference in time periods.

This suggests that emulsification makes the biofuel more flammable and hence it's able

to combust quicker. However, Figure 7 does not really explain the root reason why the combustion period is longer. For that, the composition of the biofuel and figure 8 provides a better understanding. The water in the emulsion is what causes the emulsified droplet to have a reduced ignition delay time and a lower combustion time period. As shown by figure 8, upon ignition the emulsion droplet has more explosive characteristics allowing it to spread out the particles - which set alight much faster in comparison to the non-emulsified fuel droplet. From this it can be concluded that the water in the emulsified droplet helps create this micro explosion phenomena, which in turn leads to a more efficient combustion process. In comparison, the non-emulsified fuel remains stagnant on the beaded thermocouple acting as one whole unit.
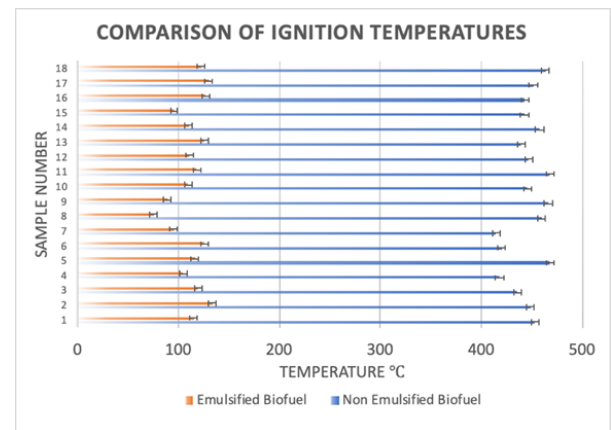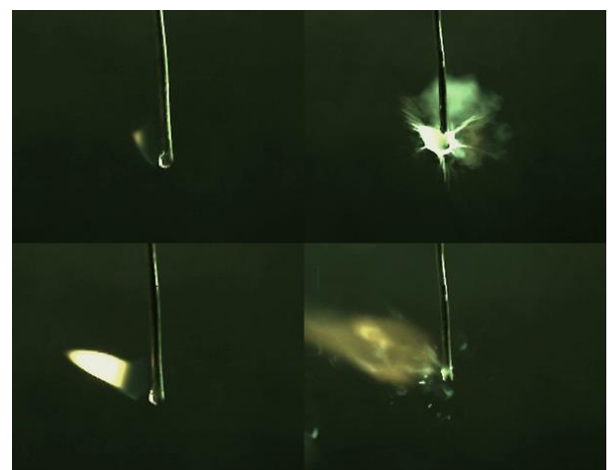

Fig. 7 Comparison of Ignition Temperatures

Fig. 8 Progression of combustion from initial ignition of Emulsified(R) and Non-Emulsified droplet(L)

Other phenomena picked up by the camera include puffing. Micro-explosions are rapid breakdown of emulsion droplet caused by explosive boiling of the liquid sub droplet which has a lower boiling point this case is

water. Whereas puffing is the bubble growth which leads to partial or full break-up of the main oil droplet. These definitions are derived from Shinjo et al [34]. When analyzing Figure 7 it can be seen that the ignition temperatures of the emulsified fields fluctuate around 110ºC mark, this is because water has a boiling point of 100 ºC. Once the water is approaching its boiling point, micro-explosions and puffing occur which cause faster combustion.

It becomes clear that most of the implications and results are validated. For example, the difference in ignition times is also shown in Reham et al [23] where an emulsified fuel has lower ignition delay times. This is due to water content in the fuel, also stated by Avulpati et al [30]. Similarly, Avulpati et al [30] results suggest the agreement with the fact that more water content in the fuel will lead to lower ignition temperatures. Although Liang et al [26] states that longer ignition time delay may have some benefits, its apparent in our experiment that the reverse is also true. A lower ignition time delay allowed quicker and more complete combustion of the fuel.

Furthermore, Shinjo et al [34] agrees with conclusion drawn about micro explosions. Shinjo et al [34] states that it has a positive effect on the combustion of fuels, which concurs with our results. As the combustion was more complete. This was noted particularly by the visual observations and picked up by the recordings and images. The images and recording show that the emulsified droplet burned quickly with there being little or no residue on the beaded thermocouple. However, the non-emulsified droplets combustion often left significant residue on the beaded thermocouple and the flame died out before fully completing the combustion of the remaining biofuel.

Avulapati et al and Shinjo et al [30, 34] also show that the puffing phenomena effect is positive as it leads to droplet rapid disintegration and complete combustion.

The tolerance for the time recorded is ±0.5 seconds, whereas the tolerance for the thermal data such as ignition temperatures is ± 0.05º C. The data for time was recorded using an internal clock on the camera, and the temperature data was given by a handheld thermocouple. This was recorded as part of the camera view, whilst the experiment was conducted. Given the weight of these tolerances, they have minimal implication on the results recorded. The digitalization of the equipment used helped to eliminate errors.

With reference to assumptions, it was assumed that the droplet size was the same for each experiment and the temperature of the flame from the gas burner was constant. In reality however, the droplet sizes did vary slightly, and the flame temperature would have varied with the amount of gas remaining in the burner. These may have had some effect on the results. For example, a lower flame temperature would have led to higher ignition delay times. However, these were addressed by ensuring the gas burner had plenty of fuel and that the size of the flame was constant. The burner had a flame size setting which made this possible. In addition to this, the syringe had volume marks which made it possible to ensure the same sized droplet could be obtained, 1.5mm ±0.5mm.

Puffing and micro-explosion in water/Fuel droplets increases the liquid fuel surface area considerably. This promotes the fuel evaporation rate and enhances fuel vapor air mixing. Consequently, leading in reduction of the inertia of ignition process ensuring complete combustion of the fuel vapor and reduction in emission. It is not surprising to note in figure 6, the ignition and complete combustion time is lower as compared to non-emulsified droplets [35].

During the fuel heating process of premixed and non-premixed water in fuel droplets, where a large number of small water droplets were evenly distributed inside a large fuel droplet, or a one large water droplet resides inside a fuel droplet respectively, demonstrated that prior to micro-explosion, the occurrence of coalescence of water sub droplets. The relative reduction in size of water sub droplets translates into an increase in the fuel droplet temperature just before micro-explosion, thus lowering the likelihood of micro-explosion. Changing the distribution of the dispersed phase sub droplets will impact on the probability of micro-explosions and therefore can be used as a design tool to control the fuel air mixing. This sub droplet distribution is also influenced by internal circulation due to the relative velocities between the droplet and

ambient air.

Furthermore, droplet heating will cause thermocapillary effects (Marangoni) responsible for the migration of the sub droplets towards the hot side promoting the mechanism of sub droplet coalescence. Because of this water sub droplet formation mechanism, a distinction between two micro explosion processes, for larger droplets in the millimeter range when complete phase separation between the water and oil can be observed typical of this experimental study as compared to typical fuel droplets sizes injected in engines with relatively small mean diameters in the order between 10-20 micro meters, where complete coalescence of the sub droplets is not achieved before micro-explosion. Explosive boiling of sub droplets is responsible for the break-up of the droplet.

Nucleation is the initial formation of bubble nucleus. Which later leads to explosive boiling. In general, nucleation is located at the interface between the water and the fuel. Surfactants are added to water in oil in order to enhance stability and the emulsion formation will depend on the HLB value (Hydrophilic-Lipophilic Balance). Low to medium HLB surfactant value is suitable for formation of W/O emulsion. Previous studies have shown that the occurrence of micro-explosion is dependent on the droplet Ohnesorge number which is defined as the ratio kinematic viscosity over the square root of the droplet density, droplet surface tension and droplet characteristic length. Lower surface tension will increase the Ohnesorge number and consequently less chance the droplet will experience micro-explosion [36]. In the study by Ballester et al., [37] water in oil emulsion was utilized in a pilot furnace, and the effects of water addition were analyzed.

Addition of water to oil significantly accelerated the evaporation of droplets in the flame and reduced the flame temperature. After non-emulsified droplet ignition, the classical droplet combustion period was observed. In this period, a stable flame was generated around the droplet, and droplet temperature rose continually with heat feedback from the flame. In the case of emulsified droplets, ignition occurred due to micro-explosion as indicated in figure 8, because as the droplet temperature increased superheated water sub droplets penetrated the fuel droplet surface, as a consequence of this a distorted flame sheet was created as compared with classical droplet combustion. This flame sheet distortion is due to the burning of the small child droplets that detached impulsively from the surface of the fuel droplet, this is illustrated in figure 8. Micro- explosion increases the contact area between the fuel and oxidizer, thus achieving better fuel vapor air mixing and higher combustion efficiency improving the combustion performance. Because micro-explosion consumes numerous heats for vaporization as the temperature of the droplet increases beyond the water boiling point. This makes the burning time lower as compared with non-emulsified fuels.

In this study sunflower oil was utilized without further processing, however the previous studies conducted in diesel engines utilized biodiesel and biodiesel blends with petroleum diesel fuels. Biodiesel is derived from vegetable oils such as sunflower oil through transesterifications. In general engine performance studies of biodiesel and its blends with diesel fuel yielded lower emissions for CO, CO_2 and HC but in some cases higher NOx emissions were recorded. The purpose of this study is preliminary investigation of emulsification of water in sunflower oil in order to tackle the issue of further reduction of NO_x emissions, thus achieving adequate results in reduction of exhaust gas emissions based on ASTM-D6751. The presence of water will lower the flame temperature and consequently reduce NO_x emissions. Water emulsification of Sunflower oil has low energy content. This has been demonstrated in figure 7, as compared with sunflower oil. However, biodiesel fuel derived from it has an energy content of around 37.5MJ/kg which is a bit lower than petroleum diesel fuel. This implies that efficiency and output is marginally lower for biodiesel compared with petroleum diesel. The energy content of the blends can be estimated [% diesel x 42.5+ % Bio-diesel x 37.5] which implies for 20% biodiesel the estimated energy output is 41.5MJ/kg. As a result, this fuel can be utilized in diesel engines with no engine modification with the advantages of lower emissions meeting the

regulation and specification of ASTM-D6751. As the aim to provide an understanding into emulsified/non- emulsified biofuels has been completed. Future work may focus on other vegetable oils or continue more detailed testing of emulsified biofuels.

5. Conclusions

Overall, both aims of the study were successfully completed. The first aim of creating an experimental setup which could carry out such testing was done by reviewing literature and designing a setup. Once the setup was designed, key components such as the heating elements were tested and substituted to ensure the experiment was able to meet the requirements of igniting sunflower oil droplets.

The results showed that ignition temperatures, ignition time delays and the total combustion time for an emulsified sunflower oil droplet is significantly lower compared to non-emulsified sunflower oil droplet.

This is due to the presence of water which lowers the boiling temperature, enabling phenomena such as m i c r o -explosion and puffing to occur. As a result of such phenomena occurring, the combustion for emulsified droplet was completed without any residue left on the beaded thermocouple, unlike the non-emulsified sunflower oil droplet. The impact of this work shows that by emulsifying biofuels in the form of vegetable oils, their ability to be used as a fuel potentially for the aviation and automotive industry are improved. Future work may concentrate on more in-depth testing of sunflower oils and a greater range of emulsions.

Nomenclature

μ = Population means
M = Sample meaning
Z = Z statistics determined by confidence level
s = standard deviation
n = sample size
W/O = Water in Oil

Conflict of Interest Statement

The research received no funding. Therefore, there is no conflict of interest.

CRediT Author Statement

The research was conducted in the framework of S. P. towards his MEng degree under the Supervision of Dr S.D.

6. References

1. Flight Path 2050 Europe's Vision for Aviation, https://transport.ec.europa.eu/system/files/2016-09/flightpath2050.pdf. 2011.
2. Gegg PK, Budd L, Ison S. The market development of aviation biofuel: Drivers and constraints. Journal of Air Transport Management, Jul 1, 39, 34–40, 2014. Available from: https://doi.org/10.1016/j.jairtraman.2014.03.003.
3. European Aviation Environmental Report 2019. https://op.europa.eu/en/publication-detail/-/publication/615da9d1-713e-11e9-9f05-01aa75ed71a1/language-en. 2017.
4. Wang M, Dewil R, Maniatis K, Wheeldon J, Tan T, Baeyens J, et al. Biomass-derived aviation fuels: Challenges and perspective. Progress in Energy and Combustion Science, Sep 1, 74, 31–49, 2019. Available from: https://doi.org/10.1016/j.pecs.2019.04.004.
5. Prussi M, O'Connell A, Laura L. Analysis of current aviation biofuel technical production potential in EU28. Biomass & Bioenergy, Nov 1, 130, 105371, 2019. Available from: https://doi.org/10.1016/j.biombioe.2019.105371.
6. Mazlan NM, Savill AM, Kipouros T. Effects of biofuels properties on aircraft engine performance. Aircraft Engineering, Sep 7, 87, 5, 437–42, 2015. Available from: https://doi.org/10.1108/aeat-09-2013-0166.
7. Azami MH, Savill AM. Comparative study of alternative biofuels on aircraft engine performance. Proceedings of the Institution of Mechanical Engineers Part G, Journal of Aerospace Engineering, Jun 22, 231, 8, 1509–21, 2016. Available from: https://doi.org/10.1177/0954410016654506.
8. Cortez LAB, Nigro FEB, Nogueira LAH, Nassar AM, Cantarella H, De Moraes MAFD, et al. Perspectives for sustainable aviation Biofuels in Brazil. International

Journal of Aerospace Engineering, Jan 1, 2015, 1–12, 2015. Available from: https://doi.org/10.1155/2015/264898.

9. Downey RK, Röbbelen G, Ashri A. Oil crops of the world: their breeding and utilization. Choice/Choice Reviews, Dec 1, 27, 04, 27–2107, 1989. Available from: https://doi.org/10.5860/choice.27-2107.

10. Barontini F, Simone M, Triana F, Am M, Ragaglini G, Nicolella C. Pilot-scale biofuel production from sunflower crops in central Italy. Renewable Energy, Nov 1, 83, 954–62, 2015. Available from: https://doi.org/10.1016/j.renene.2015.05.043.

11. Anastasi U, Santonoceto C, Giuffrè AM, Sortino O, Gresta F, Abbate V. Yield performance and grain lipid composition of standard and oleic sunflower as affected by water supply. Field Crops Research, Oct 1, 119, 1, 145–53, 2010. Available from: https://doi.org/10.1016/j.fcr.2010.07.001.

12. Sanz-Requena JF, Guimarães AC, Alpera SQ, Gangas ER, Hernández-Navarro S, Navas-Gracia LM, et al. Life Cycle Assessment (LCA) of the biofuel production process from sunflower oil, rapeseed oil and soybean oil. Fuel Processing Technology, Feb 1, 92, 2, 190–9, 2011. Available from: https://doi.org/10.1016/j.fuproc.2010.03.004

13. Hemanandh J, Narayanan KV. Emission and Performance analysis of hydrotreated refined sunflower oil as alternate fuel. Alexandria Engineering Journal Alexandria Engineering Journal, Sep 1, 54, 3, 389–93, 2015. Available from: https://doi.org/10.1016/j.aej.2015.04.004.

14. Amini-Niaki SR, Ghazanfari A. Comparison of fuel and emission properties of petro diesel and sunflower biodiesel prepared by optimized production variables. Fuel, Jul 1, 109, 384–8, 2013. Available from: https://doi.org/10.1016/j.fuel.2012.11.012.

15. B Ziebell A, Barb JG, Sandhu S, Moyers BT, Sykes R, Doeppke C, et al. Sunflower as a biofuels crop: An analysis of lignocellulosic chemical properties. Biomass & Bioenergy, Dec 1, 59, 208–17, 2013. Available from: https://doi.org/10.1016/j.biombioe.2013.06.009.

16. Zhao X, Wei L, Julson J, Qiao Q, Dubey A, Anderson GA. Catalytic cracking of non-edible sunflower oil over ZSM-5 for hydrocarbon bio-jet fuel. New Biotechnology, Mar 1, 32, 2, 300–12, 2015. Available from: https://doi.org/10.1016/j.nbt.2015.01.004.

17. Xu Y, Keresztes I, Condo AM, Phillips D, Pepiot P, Avedisian CT. Droplet combustion characteristics of algae-derived renewable diesel, conventional #2 diesel, and their mixtures. Fuel, Mar 1, 67, 295–305, 2016. Available from: https://doi.org/10.1016/j.fuel.2015.11.036.

18. Liu Y, Alam FE, Xu Y, Dryer FL, Avedisian CT, Farouk T. Combustion characteristics of butanol isomers in multiphase droplet configurations. Combustion and Flame, Jul 1, 169, 216–28, 2016. Available from: https://doi.org/10.1016/j.combustflame.2016.04.018.

19. Liu Y, Savas AJ, Avedisian CT. The spherically symmetric droplet burning characteristics of Jet-A and biofuels derived from camelina and tallow. Fuel, Jun 1, 108, 824–32, 2013. Available from: https://doi.org/10.1016/j.fuel.2013.02.025.

20. Alam FE, Liu Y, Avedisian CT, Dryer FL, Farouk T. n-Butanol droplet combustion: Numerical modeling and reduced gravity experiments. Proceedings of the Combustion Institute, Jan 1, 35, 2, 1693–700, 2015. Available from: https://doi.org/10.1016/j.proci.2014.06.043.

21. Ma Z, Li Y, Li Z, Du W, Yin Z, Xu S. Evaporation and combustion characteristics of hydrocarbon fuel droplet in sub- and super-critical environments. Fuel, May 1, 220, 763–8, 2018. Available from: https://doi.org/10.1016/j.fuel.2018.02.073.

22. Rasid AFA, Zhang Y. Combustion characteristics and liquid-phase visualisation of single isolated diesel droplet with surface contaminated by soot particles. Proceedings of the Combustion Institute, Jan 1, 37, 3, 3401–8, 2019. Available from: https://doi.org/10.1016/j.proci.2018.08.023.

23. Reham SS, Masjuki HH, Kalam MA, Shancita I, Fattah IMR, Ruhul AM. Study on stability, fuel properties, engine combustion, performance and emission characteristics of biofuel emulsion. Renewable & Sustainable Energy Reviews, Dec 1, 52, 1566–79, 2015.

Available   from: https://doi.org/10.1016/j.rser.2015.08.013.
24.   Debnath BK, Sahoo N, Saha UK. Adjusting the operating characteristics to improve the performance of an emulsified palm oil methyl ester run diesel engine. Energy Conversion and Management, May 1, 69, 191–8,   2013.   Available   from: https://doi.org/10.1016/j.enconman.2013.01.031.
25.   Ithnin AM, Nishihara H, Kadir HA, Jazair W. An overview of utilizing water-in-diesel emulsion fuel in diesel engine and its potential research study. Journal of the Energy Institute, Nov 1, 87, 4, 273–88, 2014. Available   from: https://doi.org/10.1016/j.joei.2014.04.002.
26.   Liang Y, Wei H, Zhang W. Effect of oxygen enriched combustion and water–diesel emulsion on the performance and emissions of turbocharged   diesel   engine.   Energy Conversion and Management, Sep 1, 73, 69–77,   2013.   Available   from: https://doi.org/10.1016/j.enconman.2013.04.023.
27.   Kim HM, Baek SW, Chang D. Auto-Ignition characteristics of Singlen-Heptane droplet in a rapid compression machine. Combustion Science and Technology, May 28, 186, 7, 912–27, 2014. Available from: https://doi.org/10.1080/00102202.2014.890598.
28.   Kim HM, Baek SW. Combustion of a single emulsion fuel droplet in a rapid compression machine. Energy, Jul 1, 106, 422–30,   2016.   Available   from: https://doi.org/10.1016/j.energy.2016.03.006.
29.   Kim H, Won J, Baek SW. Evaporation of a single emulsion fuel droplet in elevated temperature and pressure conditions. Fuel, Aug 1, 226, 172–80, 2018. Available from: https://doi.org/10.1016/j.fuel.2018.04.010.
30.   Avulapati MM, Ganippa L, Xia J, Megaritis A. Puffing and micro-explosion of diesel–biodiesel–ethanol blends. Fuel, Feb 1, 166,   59–66,   2016.   Available   from: https://doi.org/10.1016/j.fuel.2015.10.107.
31.   Khan MY, Karim ZAA, Aziz A, Tan IM.   Experimental   Investigation   of Microexplosion Occurrence in Water in Diesel Emulsion Droplets during the Leidenfrost Effect. Energy & Fuels, Oct 30, 28, 11, 7079–

84,   2014.   Available   from: https://doi.org/10.1021/ef501588z.
32.   Sahota R.   and Dakka S.M. Investigating the Stability of Biofuels Using Sunflower Oil, Chem Engineering, 4, 2, 36, 2020.   Available   from: https://www.mdpi.com/2305-7084/4/2/36.
33.   Mura, E.; Massoli, P.; Josset, C.; Loubar, K.; Bellettre, J. Study of the micro-explosion temperature of water in oil emulsion droplets during the Leidenfrost effect. Exp. Therm. Fluid Sci., 43, 63–70, 2012.
34.   Shinjo J, Xia J, Ganippa L, Megaritis A. Physics of puffing and microexplosion of emulsion fuel droplets. Physics of Fluids [Internet]. 2014 Oct 1;26(10). Available from: https://doi.org/10.1063/1.4897918.
35.   D.V. Antonov, P.A. Strizhak, R.M. Fedorenko, Z. Nissar, S.S. Sazhin. P Puffing/micro-explosion of two closely spaced composite droplets in tandem: experimental results and modelling. International Journal of Heat and Mass Transfer, 121449, September 2021.
https://doi.org/10.1016/j.ijheatmasstransfer.2021.121449.
36.   Mura. E., Josset. C., Loubar. K., Huchet. G., Bellettre. J. Effect of dispersed water   droplet   size   in   micro-explosion phenomenon for water in oil emulsion. Atomization and Sprays, Vol. 20, pp. 791-799, 2010.
37.   Javier M. Ballester, Norberto Fueyo, César Dopazo, Combustion characteristics of heavy oil-water emulsions, Fuel. Volume 75, Issue 6, Pages 695-705, May 1996. https://doi.org/10.1016/0016-2361(95)00309-6.
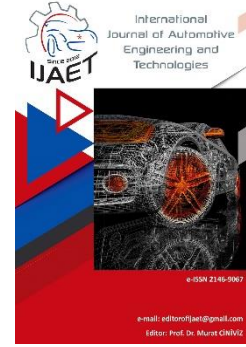
Original Research Article

Thermodynamic performance comparison of a mobile air conditioning system for various HFO and HC alternative refrigerants to replace R134a

Eren Kabak [1] and Murat Hoşöz [2, *]

[1, 2 *] Department of Automotive Engineering, Kocaeli University, Kocaeli, 41001, Türkiye.

ARTICLE INFO

ABSTRACT

The thermodynamic performance of a mobile air conditioning (MAC) system with R134a was compared with the performance offered by some Hydrofluoroolefin (HFO) and Hydrocarbon (HC) refrigerants, namely R1234yf, R1234ze(e), R152a, R290 and R600a. Both the energy and exergy performance merits of the MAC system, including the COP, the rates of exergy destroyed in the components and the exergetic efficiency, were taken into account. In this comparison, the cooling load of the evaporator was varied between 3 kW and 7 kW, both the superheat and subcooling at the outlets of the heat exchangers were assumed to be 5 °C. The refrigerant properties were determined using the REFPROP 9.1 software for a typical evaporating temperature of −2 °C, condenser temperatures of 40 and 50 °C and compressor isentropic efficiency of 55%. Then, the proposed performance parameters of the MAC system were calculated. R1234yf, R1234ze(e) and R290 yielded on average 4.41%, 0.20% and 1.69% lower COP, respectively, whereas R600a and R152a resulted in on average 2.45% and 3.39% higher COP, respectively, relative to R134a. In agreement with the COP findings, R1234yf, R1234ze(e) and R290 provided on average 4.34%, 0.22% and 1.64% lower exergetic efficiency, while R600a and R152a yielded on average 2.38% and 3.35% higher exergetic efficiency, respectively than R134a.

Keywords: Air conditioning, mobile, R1234yf, R1234ze(e), R134a, R152a, R290, R600a

1. Introduction

Mobile air conditioning (MAC) systems were developed in the 1930s [1], and they have been employed in automobiles since then. The first MAC systems used R12, a refrigerant from the Chlorofluorocarbon (CFC) family. However, upon realizing that the chlorine atoms in the CFC refrigerants harmed the stratospheric ozone layer, the use of refrigerants containing chlorine was restricted by the 1987 Montreal Protocol [2]. Consequently, starting in 1994, MAC systems used R134a, a Hydrofluorocarbon (HFC) refrigerant, to replace R12. The ozone-depleting potential (ODP) of R134a is zero but with a global warming potential (GWP) of 1430 [3], it significantly contributes to global warming.

Therefore, in line with the 1997 Kyoto Protocol [4], the European Union put into effect the F-Gas Regulation [5], which mandates that the MAC systems in the new vehicles on the EU market must employ refrigerants with a GWP not exceeding 150. Because R134a could not meet this criterion, R1234yf from the Hydrofluoroolefin (HFO) family was developed as an alternative and employed in the MAC systems of the new vehicles. The operating pressures of R1234yf are close to those of R134a and it has a GWP of only 4 [3]. However, the cooling capacity and coefficient of performance (COP) provided by R1234yf are lower than R134a. Furthermore, it is much more expensive than R134a and it is a refrigerant from the lower-flammability family [3,6]. Although another HFO refrigerant, namely R1234ze(e), was also developed, it was not used in the MAC systems commercially. R1234ze(e) has a GWP of 1, an ODP of zero and is also a refrigerant from the lower-flammability family [7]. In addition to these HFO refrigerants, refrigerants from the Hydrocarbon (HC) family such as R600a (isobutane), R290 (propane) and R152a (difluoroethane) can be used as R134a alternatives. Although all these HC refrigerants have zero ODP, the GWP of both R600a and R290 are 3, while the GWP of R152a is 124. However, R600a and R290 have higher flammability, whereas R152a has lower flammability but not as low as R1234yf and R1234ze(e).

The performance of R1234yf replacing R134a in MAC systems has been studied extensively using theoretical or experimental methods. In these studies, the performance parameters considered were usually obtained from the energy (first law) analysis of the system components.

Many studies showed that R1234yf usually yielded a lower evaporator cooling load and a lower coefficient of performance (COP) [3, 8−11]. As a remedy to this low-performance problem, some studies considered employing an internal heat exchanger (IHX) for transferring heat between the liquid and vapour lines of the MAC system using R1234yf. Thus, the liquid refrigerant passing through the IHX cools down and enters the expansion device at a lower enthalpy. Consequently, the refrigerant entering the evaporator with low enthalpy absorbs more heat from the air stream to be cooled, thereby improving the cooling capacity. Investigators using an IHX in the R1234yf MAC system obtained cooling capacity and COP values close to the values in the R134a system [12−17]. Alkan and İnan [18] observed that the R1234yf MAC system caused higher compressor and expansion device exergy destruction rates but lower evaporator and condenser exergy destruction rates relative to the R134a one. Aral et al. [19] investigated the performance of a MAC/heat pump system using R1234yf and R134a. According to their findings, the cooling load, COP and exergetic efficiency of the R1234yf system were 5.5%, 11.9% and 17.6% lower, respectively than the R134a one in the cooling mode.

A study concluded that the use of R1234yf in a MAC system caused a lower compression ratio, compressor discharge temperature and COP but a higher compressor power relative to R134a [20]. Yataganbaba et al. [21] theoretically investigated the exergy performance of a refrigeration circuit for R134a, R1234yf and R1234ze(e) and determined that both HFO refrigerants are appropriate replacements for R134a. Devecioğlu and Oruç [7] presented a theoretical performance comparison of refrigeration systems using R134a alternatives, namely R1234yf, R1234ze(e), R513a, R445a and R450a. They determined that R450a resulted in comparable COPs with R134a and the best exergetic efficiency was provided by R445a.

The literature survey shows that although the performance of MAC systems with R1234yf was widely investigated, other R134a alternatives were not thoroughly studied. In most of these studies, the performance merits considered were usually the energetic ones and the comparisons were usually based on experimental work. Besides the energy performance, this investigation theoretically evaluates the exergy performance of a MAC system for not only R1234yf but also the other four R134a alternatives, namely R1234ze(e), R152a, R290 and R600a. Then, the results obtained with the alternative refrigerants were compared with those of R134a.

2. Materials and Methods
2.1. The sketch and operation of the MAC system

The sketch of the refrigeration cycle of the MAC system is presented in Figure 1. Its primary elements are the compressor, condenser, expansion device and evaporator.
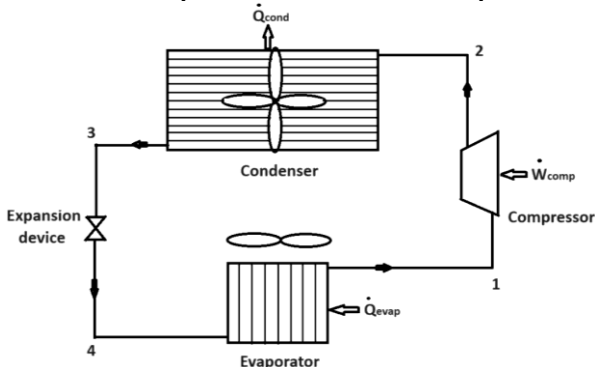

Figure 1. Schematic view of the MAC system

The air stream is pulled from either the ambient (fresh air operation) or passenger compartment (recirculated air operation) and passed over the evaporator by a centrifugal fan. Heat transfers from the air stream to the refrigerant because the refrigerant evaporates at a lower temperature, thus cooling down the air stream. Due to the concurrent condensation of the moisture, a low-temperature air stream with a low moisture content is obtained at the evaporator outlet. This conditioned air stream is sent to the passenger compartment by the centrifugal fan, thus providing thermal comfort inside the compartment. Upon gaining heat from the air stream, the refrigerant evaporates and becomes saturated vapour. Then, it superheats, leaves the evaporator and is drawn into the compressor. Accompanying the pressure rise, the refrigerant temperature rises during the compression. Then, the high-pressure refrigerant leaving the compressor goes into the condenser and transfers heat to the ambient air. As a result, the refrigerant first cools to the condensing temperature and becomes a saturated vapour. Then, it condenses and becomes a saturated liquid, and finally, it subcools below the condensing temperature and exits the condenser. The movement of the ambient air over the condenser is accomplished by an axial fan. Next, the liquid refrigerant enters the expansion device. When the refrigerant is forced to flow through a narrow cross-section

in the expansion device, its pressure drops to the evaporating pressure. Accompanying the pressure decrease, the temperature also drops and a low-quality refrigerant with a temperature usually just below 0 °C is obtained at the outlet. Next, the refrigerant leaves the expansion device, passes through the evaporator, and the cycle starts over.
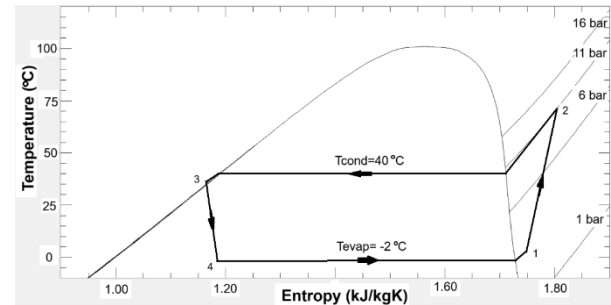
Figure 2. T-s diagram of the refrigeration cycle of the MAC system for R134a
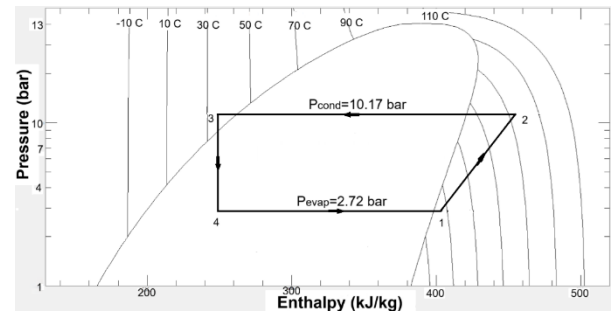
Figure 3. P-h diagram of the refrigeration cycle of the MAC system for R134a

The T-s and P-h diagrams of the refrigeration cycle of the MAC system for the case of using R134a are indicated in Figures 2 and 3, respectively. They were plotted for −2 °C evaporating temperature, 40 °C condensing temperature, 5 °C evaporator superheat, 5 °C condenser subcooling and 55% compressor isentropic efficiency, which were the main input parameters for all refrigerants in this study.

2.2. Energy and exergy analysis of the MAC system

Before analysing the system, the assumptions below are made:
- The operation is in a steady state.
- The kinetic and potential energy variations are negligible.
- The pressure does not change in the evaporator, condenser and refrigerant lines.
- The heat transfer in the refrigerant lines, compressor and expansion device are negligible.

- The dead state of the refrigerants is P_0 = 1.013 bar and $T_0 = T_{cond} - 10$ °C.

By applying the conservation of energy law to its elements, various energetic performance parameters of the MAC system can be determined. If the refrigerant enthalpies entering and exiting the evaporator and the cooling load are known, the refrigerant mass flow rate is

$$\dot{m}_r = \frac{\dot{Q}_{evap}}{h_1 - h_4} \qquad (1)$$

The compressor power transferred to the refrigerant is

$$|\dot{W}_{comp}| = \dot{m}_r(h_2 - h_1) \qquad (2)$$

The condenser heat rejection rate can be found from

$$|\dot{Q}_{cond}| = \dot{m}_r(h_2 - h_3) \qquad (3)$$

Since the expansion device operates adiabatically, the refrigerant enthalpy stays constant in it, i.e.

$$h_4 = h_3 \qquad (4)$$

The energy effectiveness of the MAC system can be determined by evaluating its COP from

$$COP = \frac{\dot{Q}_{evap}}{|\dot{W}_{comp}|} \qquad (5)$$

To identify the components leading to thermodynamic inefficiencies along with their magnitudes, an exergy analysis of the MAC system can be performed. For this aim, the following equation [22] can be used.

$$\sum \left(1 - \frac{T_0}{T_j}\right)\dot{Q}_j - \dot{W}_{cv} + \sum \dot{m}_{in}\psi_{in} - \sum \dot{m}_{out}\psi_{out} = \dot{E}x_d \qquad (6)$$

where $\dot{E}x_d$ is the exergy destruction rate and ψ is the specific flow exergy defined below.

$$\psi = (h - h_0) - T_0(s - s_0) \qquad (7)$$

where subscript 0 represents the dead state.

Because of the heat transfer from the outgoing to the incoming refrigerant streams and friction, exergy is destroyed in the compressor, whose rate can be determined from Equation (6) as

$$\dot{E}x_{d,comp} = \dot{m}_r(\psi_1 - \psi_2) + |\dot{W}_{comp}| \qquad (8)$$

As a result of the heat transfer, exergy is destroyed in the condenser, whose rate can be evaluated from [23]

$$\dot{E}x_{d,cond} = \dot{m}_r(\psi_2 - \psi_3) - \left(1 - \frac{T_0}{T_3}\right)|\dot{Q}_{cond}| \qquad (9)$$

As a result of the heat transfer, exergy is destroyed in the evaporator, whose rate can be evaluated from [23]

$$\dot{E}x_{d,evap} = \dot{m}_r(\psi_4 - \psi_1) + \left(1 - \frac{T_0}{T_1}\right)\dot{Q}_{evap} \qquad (10)$$

Exergy is destroyed in the expansion device due to the sudden expansion of the refrigerant. Assuming that the expansion device operates adiabatically, its rate can be evaluated from

$$\dot{E}x_{d,exp} = \dot{m}_r(\psi_3 - \psi_4) \qquad (11)$$

The summation of exergy destructions in its components yields the rate of total exergy destructed in the MAC system, i.e.

$$\dot{E}x_{d,tot} = \dot{E}x_{d,comp} + \dot{E}x_{d,cond} + \dot{E}x_{d,evap} + \dot{E}x_{d,exp} \qquad (12)$$

Then, the exergetic efficiency of the MAC system can be evaluated from

$$\eta_{ex} = 1 - \frac{\dot{E}x_{d,tot}}{\dot{E}x_{in}} \qquad (13)$$

In this equation, $\dot{E}x_{in}$ is the exergy entering the system, i.e. the compressor power given in Eq. (2).

2.3. Properties of the refrigerants

Important thermodynamic, environmental and safety properties of the considered refrigerants are listed in Table 1. R1234yf and R152a have boiling points close to that of R134a. On the other hand, R600a, R290 and R152a have latent heat of vaporization values considerably higher than R134a, while R1234yf and R1234ze(e) have slightly lower latent heat of vaporization values than R134a. All considered refrigerants have zero ODP values, while all alternative refrigerants except for R152a provide very low GWP values in comparison to R134a. Although R152a has a GWP of 124, it is still below the maximum value allowed by the EU F-Gas Regulation, which is 150.

The most important disadvantage of the considered alternative refrigerants is their flammability. The ASHRAE safety group of R134a is A1, meaning that there is no flame propagation in R134a. The ASHRAE safety

group of both R1234yf and R1234ze(e) is A2L, meaning that these refrigerants have lower flammability. The ASHRAE safety group of both R600a and R290 is A3, indicating that these refrigerants are highly flammable. Finally, the safety group of R152a is A2, meaning that it is less flammable than R600a and R290 but has a maximum burning velocity exceeding 10 cm/s. Although A2 and A3 safety group refrigerants can be used in stationary systems, it is risky to employ them in MAC systems, which pose a fire risk during traffic accidents.

2.4. Comparison procedure

The thermodynamic performance of the MAC system operating with the considered refrigerants was evaluated at an evaporating temperature of −2 °C, which is a typical value for most MAC systems. In the evaluation, the evaporator cooling load varied from 3 kW to 7 kW with 1 kW intervals, which are typical loads of MAC systems employed in automobiles. It was assumed that the condenser subcooling and evaporator superheat are both 5 °C. A compressor isentropic efficiency of 55% is accepted as a typical value. Then, the refrigerant properties at various points of the refrigeration circuit were obtained from the REFPROP 9.1 software [26] for the condenser temperatures of 40 and 50 °C. Finally, the performance parameters were determined from Equations (1−13) for all considered refrigerants and operation conditions.

3. Results and Discussion

The performance parameters of the MAC system for R134a and its two HFO and three HC alternatives, namely R1234yf, R1234ze(e), R152a, R290 and R600a, are shown in Figures 4–15 as a function of the evaporator cooling load (cooling capacity) for

two condenser temperatures. Moreover, the thermodynamic specifications of the refrigerants at various points are presented in Table 2 for the evaporator cooling load of 5 kW, evaporating temperature of −2 °C and 50 °C condenser temperature as sample results.

The mass flow rate of the refrigerant is exhibited in Figure 4. It tends to increase with the evaporator load and condensing temperature for all refrigerants. As seen in Table 1, R290 has the highest latent heat of vaporization among the considered refrigerants, which is followed by R600a, R152a, R134a, R1234ze(e)and R1234yf in decreasing order. The flow rate is inversely proportional to the latent heat of vaporization of the refrigerant for a fixed evaporator cooling load. As a result, the curves in Figure 4 are in reverse order, i.e. R600a yields the lowest flow rate while R1234yf results in the highest one. Furthermore, to meet the cooling demand, the flow rate gets higher with the rising evaporator cooling load. It also gets higher with the rising condensing temperature for a constant evaporating temperature because of the rising compression ratio, which promotes refrigerant circulation. The average R134a flow rate is 34.47 g/s, while the average R1234yf flow rate is 44.97 g/s, which is 30.44% higher than that of R134a. Furthermore, the average R1234ze(e) flow rate is 37.94 g/s, which is 10.07% higher than that of R134a. R600a yields an average flow rate of 19.00 g/s, which is 44.79% lower than that of R134a. R290 results in an average flow rate of 18.29 g/s, which is 46.93% lower than that of R134a. Finally, R152a yields an average flow rate of 20.88 g/s, which is 39.40% lower than that of R134a. The R1234yf and R134a mass flow rate results of this investigation agree with Alkan et al. [9], Prabakaran et al. [11], Cho and Park [12] and Aral et al. [19].

Table 1. Thermodynamic, environmental and safety properties of the considered refrigerants [7, 19, 24−26]

Refrigerant	R134a	R1234yf	R1234ze(e)	R152a	R290	R600a
Boiling point at 101.325 kPa (°C)	-26.07	-29.45	-18.97	-24.02	-42.11	-11.75
Critical temperature (°C)	101.06	94.70	109.4	113.30	96.68	134.7
Critical pressure (kPa)	4059	3382	3635	4520	4248	3640
Liquid density at 0°C (kg/m³)	1294.8	1176.3	1240.1	959.11	528.59	580.58
Vapour density at 0°C (kg/m³)	14.428	17.647	11.714	8.359	10.351	4.257
Latent heat of vaporization at 0 °C (kJ/kg)	198.60	163.29	184.18	307.11	374.87	354.34
ODP	0	0	0	0	0	0
GWP	1430	4	1	124	3	3
ASHRAE Safety Group	A1	A2L	A2L	A2	A3	A3

Table 2. The thermodynamic specifications of the refrigerants for Q_{evap} = 5 kW, T_{evap} = −2 °C and T_{cond} = 50 °C

Location	Pressure (bar)	Temperature (°C)	Enthalpy (kJ/kg)	Entropy (kJ/kg K)	Flow exergy (kJ/kg)
		Specifications for R134a ($\dot{m}_r$ = 36.24 g/s)			
1	2.72	3.0	401.86	1.7444	26.55
2	13.18	85.0	463.26	1.8244	62.91
3	13.18	45.0	263.90	1.2134	54.79
4	2.72	-2.0	263.90	1.2358	47.80
		Specifications for R1234yf ($\dot{m}_r$ = 47.92 g/s)			
1	2.95	3.0	366.58	1.6143	25.74
2	13.02	69.7	415.78	1.6807	54.16
3	13.02	45.0	262.23	1.2075	48.72
4	2.95	-2.0	262.23	1.2296	41.80
		Specifications for R1234ze(e) ($\dot{m}_r$ = 40.01 g/s)			
1	2.01	3.0	387.20	1.6903	17.31
2	9.97	75.4	443.05	1.7649	49.82
3	9.97	45.0	262.25	1.2084	43.20
4	2.01	-2.0	262.25	1.2297	36.53
		Specifications for R152a ($\dot{m}_r$ = 21.71 g/s)			
1	2.46	3.0	511.15	2.1475	36.42
2	11.77	102.8	609.35	2.2704	96.16
3	11.76	45.0	280.82	1.2701	80.72
4	2.46	-2.0	280.82	1.2982	71.93
		Specifications for R290 ($\dot{m}_r$ = 19.26 g/s)			
1	4.46	3.0	581.27	2.4061	88.80
2	13.69	83.34	699.09	2.5599	158.47
3	13.69	45.0	321.63	1.4029	143.16
4	4.46	-2.0	321.63	1.4488	128.78
		Specifications for R600a ($\dot{m}_r$ = 19.95 g/s)			
1	1.46	3.0	559.73	2.3265	19.90
2	6.85	73.4	668.22	2.4725	82.69
3	6.85	45.0	309.09	1.3659	69.93
4	1.46	-2.0	309.09	1.4024	58.49

They all obtained similar tendencies and found that R1234yf yielded a greater flow rate than R134a.

The compressor power is exhibited in Figure 5. It increases with the evaporator load and condensing temperature for all refrigerants. The compressor power depends on the compressor pressure ratio, refrigerant mass flow rate and refrigerant type. As a result of the combined effect of these parameters, R152a absorbs the least compressor power while R1234yf absorbs the greatest power. Because the pressure ratio gets higher with rising condensing temperature, so does the compressor power for all refrigerants. Since the refrigerant flow rate rises with the evaporator cooling load, the compressor power also rises.

The average compressor power for R134a is 1.95 kW. R1234yf, R1234ze(e) and R290 yield on average 4.95%, 0.26% and 1.78% more compressor power, respectively, in comparison to R134a.
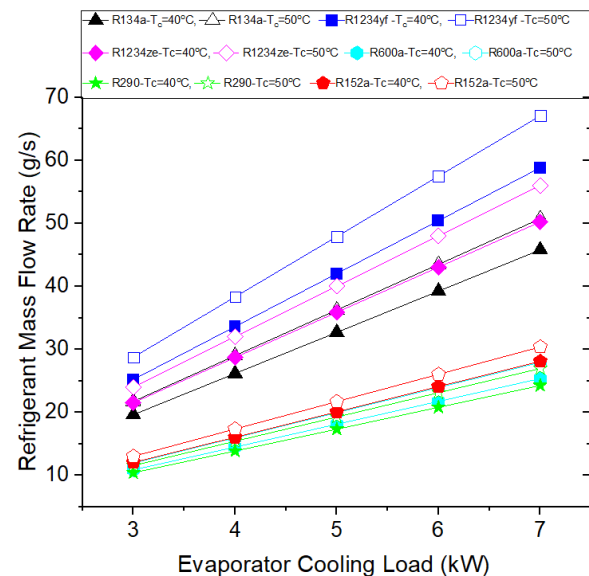
Furthermore, R600a and R152a yield on

Figure 4. Refrigerant mass flow rate vs. evaporator cooling load

average 2.48% and 3.50% less compressor power than R134a, respectively. The compressor power results obtained for R1234yf and R134a are in line with Alkan et al. [9] and Aral et al. [19]. They also found that, compared to R134a, R1234yf absorbed more

compressor power.

The COP, the ratio of the evaporator cooling load to the compressor power, is presented in Figure 6. The COP stays constant for a specific refrigerant and condensing temperature since the compressor power increases at the same ratio as the cooling load for all refrigerants, no matter what the cooling load is. However, the COP decreases with the rising condensing temperature due to the increasing compressor power. The average COP for R134a is determined as 2.61. R1234yf, R1234ze(e) and R290 yield on average 4.41%, 0.20% and 1.69% lower COP, respectively, whereas R600a and R152a result in on average 2.45% and 3.39% higher COP, respectively, in comparison to R134a. Higher COP values provided by R600a and R152a mean that these two refrigerants are more energy efficient than R134a and other R134a alternatives. The R1234yf and R134a COP findings are in agreement with Devecioğlu et al. [7], Alkan et al. [9], Prabakaran et al. [11], Cho and Park [12], Aral et al. [19] and Mota-Babiloni et al. [24]. They all determined that R1234yf yielded lower COP values than R134a. Furthermore, in agreement with our study, Devecioglu et al. [7] and Mota-Babiloni et al. [24] also obtained that the COP for R1234ze(e) was lower than R134a but higher than R1234ze(e).
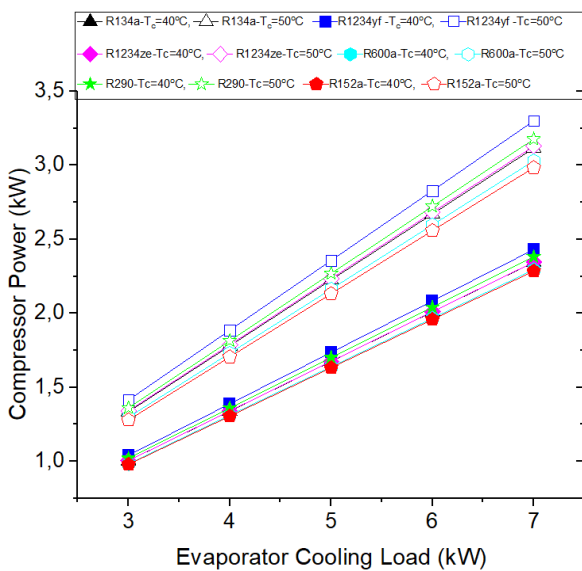

Figure 5. Compressor power vs. evaporator cooling load

The condenser heat rejection rate, the summation of the evaporator cooling load and compressor power, is reported in Figure 7. It increases with the evaporator cooling load and condensing temperature for all refrigerants.
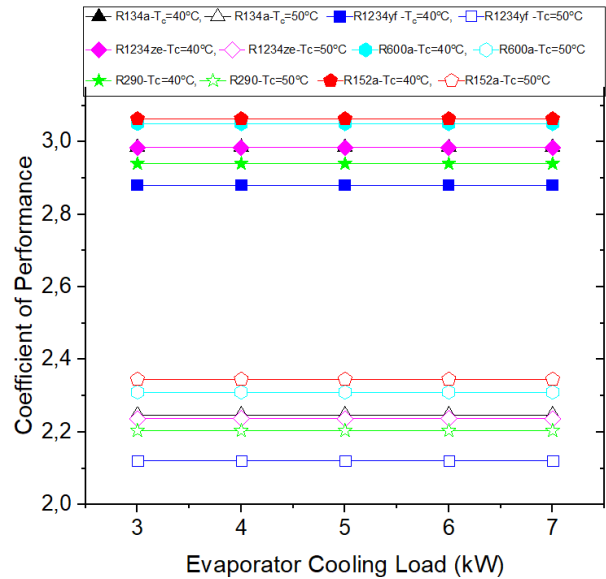

Figure 6. COP vs. evaporator cooling load

Because R1234yf employs the highest compressor power while R152a employs the lowest one, R1234yf rejects the highest heat while R152a rejects the lowest one in the condenser. Because the operation at a high condensing temperature requires more compressor power, the condenser heat rejection rate increases with rising condensing temperature. The average condenser heat rejection rate for R134a is 6.95 kW. R1234yf, R1234ze(e) and R290 yield on average 1.38%, 0.07% and 0.49% more condenser heat rejection rate, respectively, while R600a and R152a reject on average 0.69% and 1.38% less heat in the condenser, respectively, than R134a.

The compressor discharge temperature is indicated in Figure 8. It rises with rising condensing temperature for all refrigerants and the evaporator cooling capacity does not affect it. The refrigerant pressure at the compressor outlet also increases with rising condensing temperature, which in turn increases the compressor discharge temperature. The average compressor discharge temperature for R134a is 78.16°C. R1234yf, R1234ze(e), R600a and R290 yield on average 14.16°C, 8.82°C, 10.52°C and 1.52°C lower compressor discharge temperature, respectively, whereas R152a yields on average 16.36°C higher discharge temperature than R134a. Because high discharge temperatures reduce the lifetime of the compressor oil, they are not welcomed. On the other hand, low discharge temperatures reduce the heat transfer in the
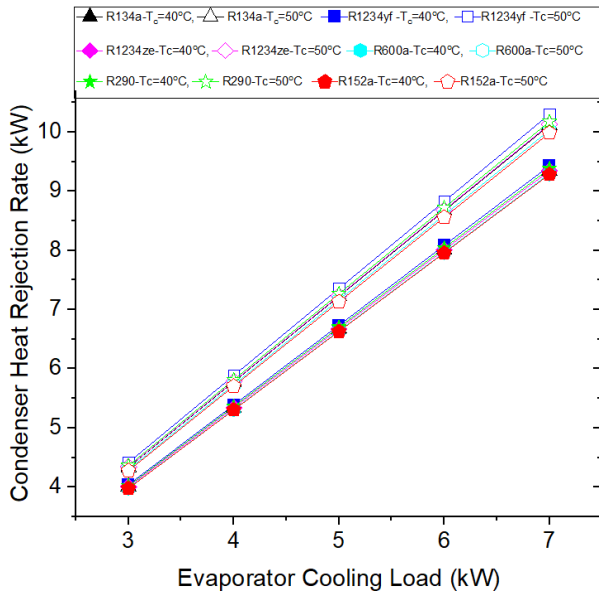
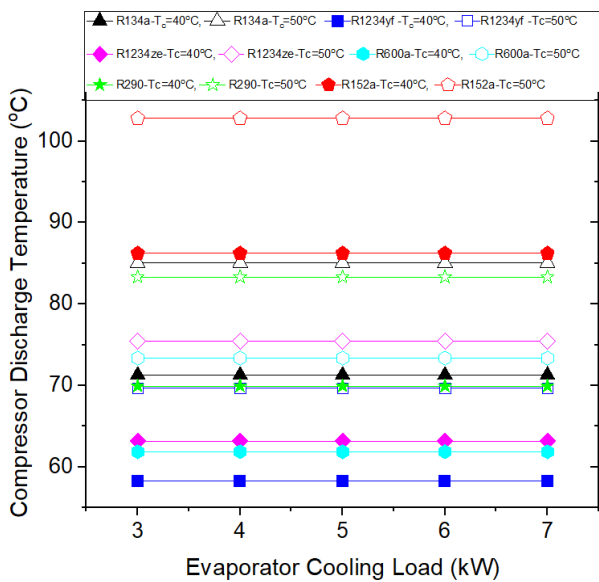Figure 7. Condenser heat rejection rate vs. evaporator cooling load

Figure 8. Compressor discharge temperature vs. evaporator cooling load

condenser, thus requiring a larger condenser heat transfer area. The compressor discharge temperature results obtained for R1234yf and R134a are in line with Alkan et al. [9], Prabakaran et al. [11], Cho and Park [12], Aral et al. [19] and Mota-Babiloni et al. [24]. They also found that R1234yf yielded lower compressor discharge temperatures than R134a. Moreover, in line with our investigation, Mota-Babiloni et al. [24] also determined that R1234ze(e) caused discharge temperatures lower than R134a but higher than R1234yf.

The compressor exergy destruction rate is presented in Figure 9. This rate gets higher with the evaporator load and condensing

temperature for all refrigerants. The compressor exergy destruction depends on the refrigerant flow rate, compressor pressure ratio and refrigerant type. Because the mass flow rate of R1234yf is higher than other refrigerants, it dominates other factors and causes the greatest destruction rate. Although R152a is not the refrigerant offering the lowest flow rate, the thermodynamic properties and compressor pressure ratio of R152a cause the lowest compressor exergy destruction rates for this refrigerant. The average compressor exergy destruction rate for R134a is 0.796 kW. R1234yf, R1234ze(e), R600a and R290 destroy on average 8.52% 2.64%, 0.50% and 2.01% more exergy in the compressor, respectively, while R152a destroys on average 7.07% less exergy in the compressor in comparison to R134a.

Figure 9. The rate of exergy destroyed in the compressor vs. evaporator cooling load

The condenser exergy destruction rate is shown in Figure 10. It gets higher with the evaporator cooling load and condensing temperature for all refrigerants. The condenser exergy destruction depends on the temperature difference between the fluids passing through and over the condenser, the refrigerant flow rate and the refrigerant type. Because R152a operates with the highest compressor discharge temperatures, it enters the condenser at a high temperature. This causes the highest temperature difference between the fluids and yields the greatest condenser exergy destruction rate. On the other hand, R1234yf and R600a operate with the lowest compressor

discharge temperatures, thus causing the lowest condenser exergy destruction rate. The average value of this rate for R134a is determined as 0.168 kW. R1234yf, R1234ze(e), R600a and R290 destroy on average 18.00%,14.60%, 18.85% and 0.27% less exergy in the condenser, respectively, while R152a destroys on average 21.3% more exergy in the condenser in comparison to R134a.
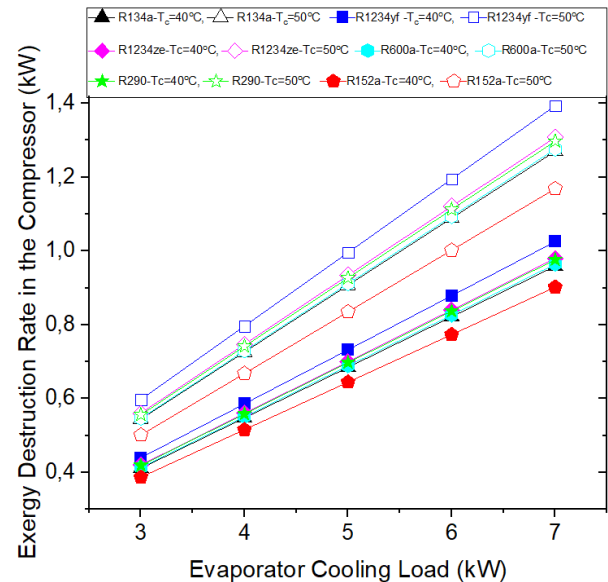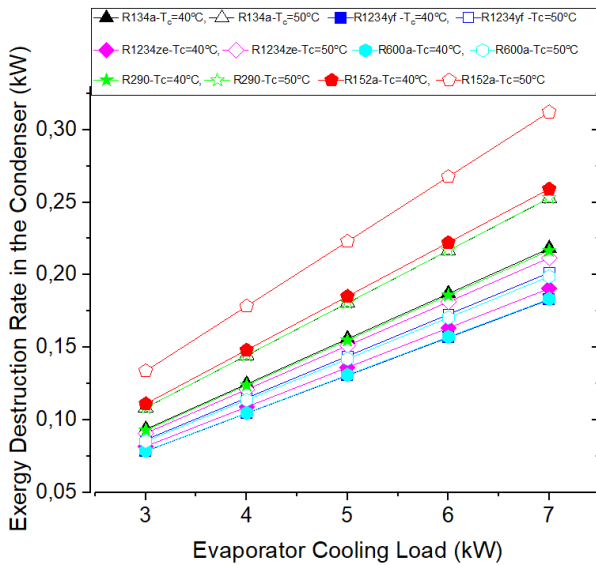

Figure 10. The rate of exergy destroyed in the condenser vs. evaporator cooling load

The evaporator exergy destruction rate is indicated in Figure 11. This rate gets higher with rising evaporator load and condensing temperature for all refrigerants. The evaporator exergy destruction depends on the temperature difference between the fluids passing through and over the evaporator, the refrigerant flow rate and the refrigerant type. Because the evaporating temperatures of all refrigerants are assumed to be −2 °C, the average temperature differences between the fluids are almost identical. Consequently, all refrigerants yield very close evaporator exergy destruction rates. The average value of this rate for R134a is 0.0982 kW. R1234yf, R1234ze(e), R600a and R290 destroy on average 0.50%, 0.79%, 0.19% and 0.08% less exergy in the evaporator, respectively, while R152a destroys on average 0.75% more exergy in the evaporator than R134a.

The expansion device exergy destruction rate is exhibited in Figure 12. This rate increases with the evaporator load and condensing temperature. It depends on the pressure decrease across the expansion device, the
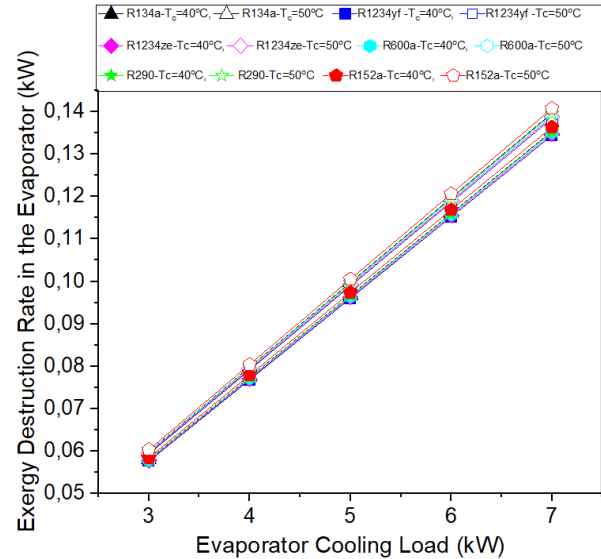
Figure 11. The rate of exergy destroyed in the evaporator vs. evaporator cooling load
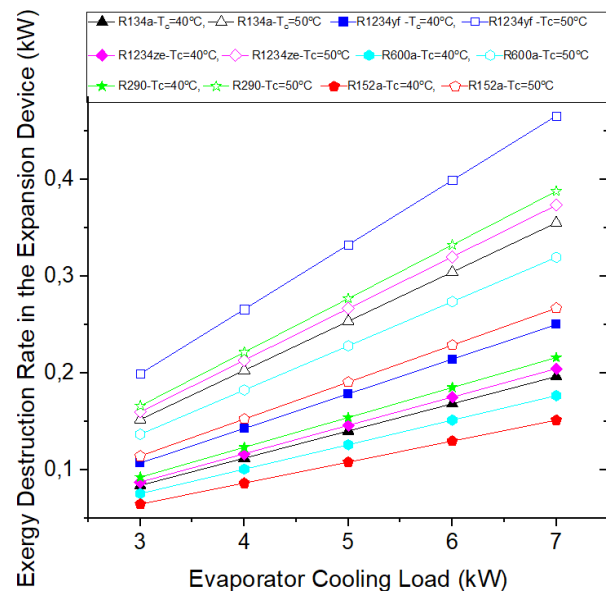
Figure 12. The rate of exergy destroyed in the expansion device vs. evaporator cooling load

refrigerant flow rate, and the refrigerant type. Therefore, the tendency of the expansion device exergy destruction curves is highly similar to the compressor exergy destruction curves. The average exergy destruction rate in this component for R134a is determined as 0.196 kW. R1234yf, R1234ze(e) and R290 yield on average 29.50%, 4.77% and 9.46% more exergy destruction, respectively, whereas R152a and R600a resulted in on average 24.09% and 10.03% less exergy destruction in the expansion device, respectively, than R134a.

The total exergy destruction rate in the MAC system is shown in Figure 13. Similar to the tendencies of its constituents, this rate increases with the evaporator load and

condensing temperature. The average total exergy destruction rate for R134a is 1.259 kW. R1234yf destroys on average a total exergy of 1.354 kW, which is 7.54% more than that for R134a. R1234ze(e) destroys on average 1.264 kW total exergy, which is 0.40% more than the exergy destruction of R134a. R600a destroys on average 1.211 kW total exergy, which is 3.77% less than that of R134a. R290 destroys on average 1.293 kW total exergy, which is 2.71% more than R134a. Finally, R152a destroys on average 1.192 kW total exergy, which is 5.33% less than R134a. The results obtained for R1234yf and R134a are in line with Alkan et al. [9] and Yataganbaba et al. [21], who determined that R1234yf caused greater total exergy destruction than R134a. Furthermore, in agreement with our investigation, Yataganbaba et al. [21] reported that the total exergy destroyed by R1234ze(e) is smaller than R1234yf but greater than R134a.
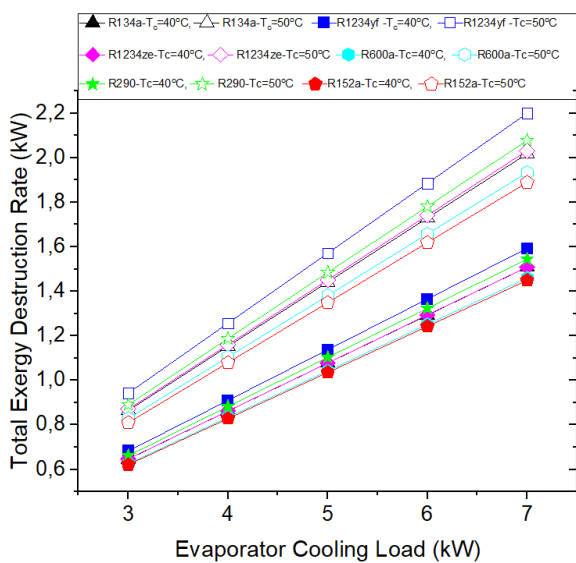
Figure 13. The rate of total exergy destroyed in the MAC system vs. evaporator cooling load

The exergetic efficiency of the MAC system is indicated in Figure 14. The tendencies of the exergetic efficiency curves are similar to the COP curves. In agreement with the higher COP values provided by R152a and R600a, they yield higher exergetic efficiencies than R134a and other alternatives. The average exergetic efficiency for R134a is determined as 35.44%. R1234yf, R1234ze(e) and R290 yield on average 4.34%, 0.22% and 1.64% lower exergetic efficiency, respectively, than R134a. On the other hand, R600a and R152a result in on average 2.38% and 3.35% higher exergetic

efficiency, respectively, than R134a. Similar to these findings, Cho and Park [12] determined that R1234yf yielded a lower second-law efficiency than R134a. Furthermore, Yataganbaba et al. [21] reported that R1234yf yielded a lower exergetic efficiency than R134a and that R1234ze(e) provided an exergetic efficiency lower than R134a but higher than R1234yf.
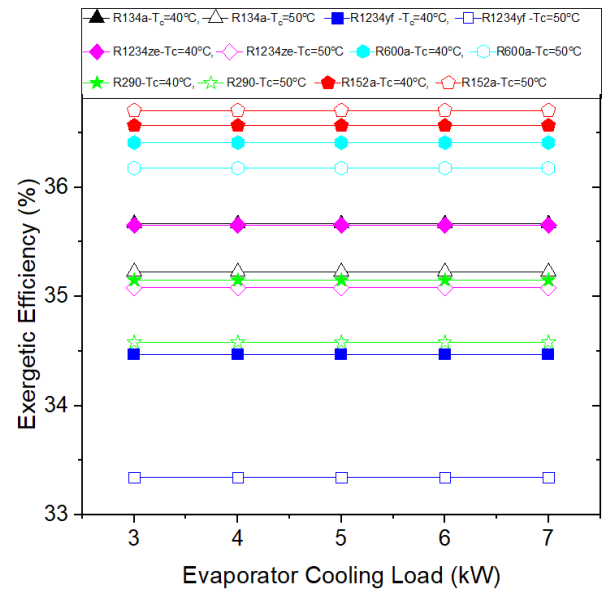
Figure 14. Exergetic efficiency of the MAC system vs. evaporator cooling load

Figure 15 indicates the percent distribution of the destructed exergy in the elements of the MAC system for 5 kW evaporator cooling capacity, −2 °C evaporating temperature and 50 °C condenser temperature.
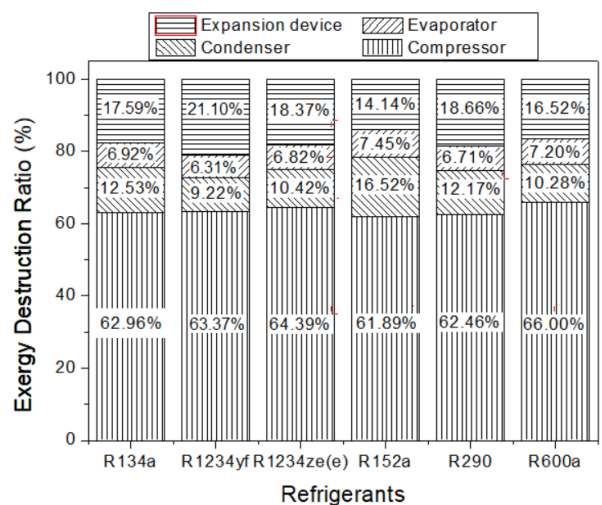
Figure 15. The percent distribution of the destructed exergy in the elements of the MAC system for $Q_{evap} = 5$ kW, $T_{evap} = −2$ °C and $T_{cond} = 50$ °C

The greatest exergy destruction occurred in the compressor while the smallest exergy destruction occurred in the evaporator for all

refrigerants. For R152a, the condenser destroys more exergy than the expansion device while the expansion device destroys more exergy than the condenser for the other five refrigerants. Because R1234yf, R1234ze(e), R290 and R600a cause less condenser exergy destruction percent than R134a, a smaller condenser will be sufficient for them in comparison to R134a.

Moreover, R152a requires a larger condenser than R134a to decrease the condenser exergy destruction percent. Yataganbaba et al. [21] also reported that the compressor was the component destroying the highest exergy and the evaporator was the component destroying the lowest exergy for a refrigeration cycle using R134a, R1234yf and R1234ze(e).

4. Conclusions

The thermodynamic performance of an R134a MAC system was compared with those of various R134a alternatives from HFO and HC family, namely R1234yf, R1234ze(e), R152a, R290 and R600a. The comparison was made for typical values of −2 °C evaporating temperature, 40 °C and 50 °C condensing temperatures, 5 °C evaporator superheat, 5 °C condenser subcooling and 55% compressor isentropic efficiency. Then, the performance parameters were evaluated from the conservation of energy and exergy rate balance equations for the typical evaporator cooling loads of 3, 4, 5, 6 and 7 kW. The main conclusions are extracted below.

- The average mass flow rates of R1234yf and R1234ze(e) are 30.45% and 10.07% higher than those of R134a, respectively. On the other hand, R600a, R290 and R152a yield on average 44.79%, 46.93% and 39.40% lower mass flow rates than R134a, respectively.

- R1234yf, R1234ze(e) and R290 yield on average 4.95%, 0.26% and 1.78% more compressor power, respectively, while R600a and R152a result in on average 2.48% and 3.50% less compressor power, respectively, than R134a.

- R1234yf, R1234ze(e) and R290 yield on average 4.41%, 0.20% and 1.69% lower COP, respectively, whereas R600a and R152a result in on average 2.45% and 3.39% higher COP, respectively, compared to R134a.

- R1234yf, R1234ze(e), R600a and R290 yield on average 14.16°C, 8.82°C, 10.52°C and 1.52°C lower compressor discharge temperature, respectively, whereas R152a yield on average 16.36°C higher compressor discharge temperature than R134a.

- R1234yf, R1234ze(e) and R290 destruct on average 7.54%, 0.40% and 2.71% more total exergy, while R600a and R152a destruct 3.77% and 5.33% less total exergy in the MAC system, respectively, relative to R134a.

- R1234yf, R1234ze(e) and R290 yield on average 4.34%, 0.22% and 1.64% lower exergetic efficiency, whereas R600a and R152a result in on average 2.38% and 3.35% higher exergetic efficiency, respectively, in comparison to R134a.

- The compressor causes the greatest exergy destruction, while the evaporator causes the smallest destruction for all refrigerants.

- R1234yf, R1234ze(e), R290 and R600a cause less condenser exergy destruction while R152a cause more condenser exergy destruction than R134a. Therefore, R152a requires a larger condenser while other refrigerants require a smaller condenser in comparison to R134a.

These findings reveal that the performance of R600a and especially R152a surpasses the performance of R134a, R1234yf and R1234ze(e), while R290 shows poorer performance than R134a, and even poorer than R1234yf. Considering that R152a has a GWP of 124, lower than the EU limit value of 150, and is classified in the ASHRAE Safety Group of A2 (lower flammability), it can be employed as an alternative refrigerant in future MAC systems. However, its performance should also be investigated experimentally before using it in MAC systems.

CRedit authorship contribution statement

Eren Kabak: Investigation, Formal analysis, Writing.
Murat Hoşöz: Conceptualization, Methodology, Supervision, Writing, Review&Editing.

Declaration of Competing Interest

The authors declare that they have no known

competing financial interests or personal relationships that could have appeared to influence the work reported in this paper.

5. References

1. Bhatti, M.S., "Riding in Comfort Part II: Evolution of Automotive Air Conditioning", ASHRAE Journal, 41, 44-50, 1999.
2. UNEP, "Montreal Protocol on substances that deplete the ozone layer, final act", United Nations Environment Programme, 1987.
3. Lee, Y. and Jung, D., "A brief performance comparison of R1234yf and R134a in a bench tester for automobile applications", Applied Thermal Engineering, 35, 240-242, 2012.
4. UNEP, "Kyoto Protocol to the United Nations Framework Convention on Climate Change", United Nations Environment Programme, 1997
5. EU, "Regulation (EU) No 517/2014 of the European Parliament and of the Council of 16 April 2014 on fluorinated greenhouse gases and repealing Regulation (EC) No 842/2006", Official Journal of European Union, L 150/195, 2014.
6. Zhang, Z., Wang, J., Feng, X., Chang, L., Chen, Y. and Wang, X., "The solutions to electric vehicle air conditioning systems: A review", Renewable and Sustainable Energy Reviews, 91, 443-463, 2018.
7. Devecioğlu, A.G. and Oruç, V., "A comparative energetic analysis for some low-GWP refrigerants as R134a replacements in various vapor compression refrigeration systems", Journal of Thermal Sciences and Technology, 38, 51-61, 2018.
8. Zilio, C., Brown, J.S., Schiochet, G. and Cavallini, A., "The refrigerant R1234yf in air conditioning systems", Energy, 36, 6110-6120, 2011.
9. Alkan, A., Kolip, A. and Hosoz, M., "Energetic and exergetic performance comparison of an experimental automotive air conditioning system using refrigerants R1234yf and R134a", Journal of Thermal Engineering, 7, 1163-1173, 2021.
10. Tasdemirci, E., Alptekin, E. and Hosoz, M., "Experimental performance comparison of R1234yf and R134a automobile air conditioning systems employing a variable capacity compressor", International Journal of Vehicle Design, 90, 1-18, 2022.
11. Prabakaran, R., Lal, D.M. and Kim S.C., "Thermodynamic analysis of air conditioning system for a passenger vehicle with suction line heat exchanger using HFO-1234yf", Heat Transfer Engineering, 814-832, 2023.
12. Cho, H., Lee, H. and Park, C., "Performance characteristics of an automobile air conditioning system with internal heat exchanger using refrigerant R1234yf", Applied Thermal Engineering, 61, 563-569, 2013.
13. Direk, M., Kelesoglu, A. and Akin, A., "Drop-in performance analysis and effect of IHX for an automotive air conditioning system with R1234yf as a replacement of R134a", Strojniski Vestnik – Journal of Mechanical Engineering, 63, 314-319, 2017.
14. Wantha, C., "Analysis of heat transfer characteristics of tube-in-tube internal heat exchangers for HFO-1234yf and HFC-134a refrigeration systems", Applied Thermal Engineering, 157, 1-10, 2019.
15. Prabakaran, R., Sidney, S., Iyyappan, R. and Lal, D.M., "Experimental studies on the performance of mobile air conditioning system using environmental friendly HFO-1234yf as a refrigerant", Proceedings of the Institution of Mechanical Engineers Part E-Journal of Process and Engineering, 235, 735-742, 2019.
16. Gungor, U. and Hosoz, M., "Performance comparison of a mobile air conditioning system using an orifice tube as an expansion device for R1234yf and R134a", Science and Technology for the Built Environment, 30, 588-598, 2024.
17. Gungor, U. and Hosoz, M., "Experimental performance evaluation of an R1234yf automobile air conditioning system employing an internal heat exchanger", International Journal of Automotive Engineering and Technology, 10 (1), 50-59, 2021.
18. Alkan, A. and İnan, M.S., "Experimental investigation of the effects of compressor types on the performance of an automobile air conditioning system using R1234yf", International Journal of Refrigeration, 155, 58-66, 2023.

19. Aral, M.C., Suhermanto, M. and Hosoz, M., "Performance evaluation of an automotive air conditioning and heat pump system using R1234yf and R134a", Science and Technology for the Built Environment, 27, 44-60, 2021.

20. Hosoz, M. and Karabektas, M., "Comparative performance of an automotive air conditioning system using R1234yf and R134a", 13th International Conference on Sustainable Energy Technologies (SET 2014), Paper ID: SET2014-E40082, Geneva, Switzerland, August 25-28, 2014.

21. Yataganbaba, A., Kilicarslan, A. and Kurtbas, I., "Exergy analysis of R1234yf and R1234ze as R134a replacements in a two evaporator vapour compression refrigeration system", International Journal of Refrigeration 60, 26-37, 2015.

22. Moran, M.J. and Shapiro, H.N., "Fundamentals of Engineering Thermodynamics", West Sussex, England: John Wiley and Sons, 2006.

23. Cho, H. and Park, C., "Experimental investigation of performance and exergy analysis of automotive air conditioning systems using refrigerant R1234yf at various compressor speeds", Applied Thermal Engineering, 101, 30-37, 2016.

24. Mota-Babiloni, A., Navarro-Esbri, J., Barragan-Cervera, A., Moles, F. and Peris, B., "Drop-in energy performance evaluation of R1234yf and R1234ze(e) in a vapour compression system as R134a replacements", Applied Thermal Engineering, 71, 259-265, 2014.

25. Hodnebrog, Ø., Etminan, M., Fuglestvedt, J.S., Marston, G., Myhre, G., Nielsen, J.C., Shine, K.P. and Wallington, T.J., "Global warming potentials and radiative efficiencies of halocarbons and related compounds: A comprehensive review". Reviews of Geophysics 51, 300-378, 2013.

26. Lemmon, E.W., Huber, M.L. and McLinden, M.O., "Reference Fluid Thermodynamic and Transport Properties (REFPROP), Version 9.1, in NIST Standard Reference Database 23, National Institute of Standards and Technology, Gaithersburg, 2013.
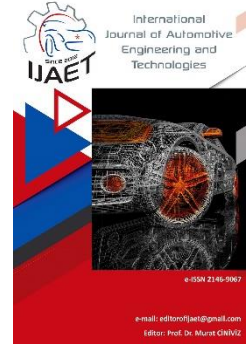
Original Research Article

Design and structural analysis of a mechanism for positioning heavy vehicle chassis

hosted by Turkish JournalPark ACADEMIC

Tolga Güney[1], Sinan Düzenli[2], Kasım Serbest[3, *]

[1, 2] YEKTAMAK Engineering and Machinery, Sakarya, Türkiye.
[3, *] Sakarya University of Applied Sciences, Department of Mechatronics Engineering, Sakarya, Türkiye.

ABSTRACT

Proper and secure positioning of heavy vehicle chassis is crucial in ensuring efficiency and safety, particularly in painting, manufacturing, and maintenance processes. This study focuses on the structural analysis and prototype production of a positioning system capable of rotating heavy vehicle chassis across three axes and setting them in an upright position. To achieve this, a scissor platform was developed to facilitate three-axis rotation, and a dedicated mechanism was designed for upright positioning. Initially, a 3D model of the system was created, and structural strength was evaluated through Finite Element Analysis (FEA), assessing stress distribution under load and deformation during rotation. The analysis revealed a maximum stress value of 190.2 MPa in the chassis tilting mechanism and 204.2 MPa in the scissor platform, with a maximum displacement of 3.1 mm observed in the scissor platform. Following optimization based on these results, a prototype was produced and tested under real working conditions. The findings validate the system's durability and functionality, demonstrating a reliable and effective solution for the positioning of heavy vehicle chassis.

Keywords: Finite Element Analysis (FEA), Structural Optimization, Three-Axis Rotation, Machine Design

1. Introduction

Due to their excessive weight and large dimensions, the precise positioning of heavy vehicle chassis is a challenging process. Accurate positioning of these chassis is essential for ensuring efficiency and meeting quality requirements in painting, manufacturing, and maintenance processes. Existing systems in the literature typically operate by combining mechanical and hydraulic components to safely and accurately lift, position, and stabilize heavy loads. These systems aim to optimize load distribution, thereby enhancing structural strength and operational efficiency.

The literature surrounding the design and analysis of scissor lift mechanisms is extensive, particularly in the context of heavy vehicle chassis positioning systems. The importance of structural integrity and stability in lifting platforms is underscored by various studies that highlight the critical role of finite

element analysis (FEA) in evaluating stress distribution and deformation underload. For instance, Chen et al. conducted a mechanical analysis and finite element simulation of scissor transmission mechanisms, emphasizing the impact of partial loads on the service life and security of these systems [1]. Similarly, Zhang et al. explored the static stability of scissor lifts, providing insights into the energy methods and modeling techniques used to assess stability under operational conditions [2]. When designing a mechanism for positioning heavy vehicle chassis, the integration of robust structural components and optimized load distribution is considered extremely important [3]. These findings are crucial for validating the structural strength of the proposed positioning system.

The development of scissor lift platforms has also seen innovations aimed at enhancing their operational efficiency and durability. For example, Solmazyigit et al. discussed the design and prototype production of a scissor lift platform with a capacity of 25 tons, which incorporated advanced materials to minimize wear and improve stability [4]. This aligns with the findings of Petru et al., who noted that the symmetrical distribution of forces on lifting platforms is essential for reducing bending moments and enhancing overall stability during operation [5]. Such design considerations are vital for ensuring that the positioning system can withstand the stresses encountered during the rotation and upright positioning of heavy vehicle chassis. Therefore, the successful design and implementation of a mechanism for positioning heavy vehicle chassis require a comprehensive understanding of fundamental principles and a thorough addressing of structural and operational challenges [6].

Moreover, the integration of hydraulic systems in scissor lifts has been shown to significantly improve their functionality. Kart's research on hydraulic walking power steering-controlled scissor lift platforms highlights the advantages of hydraulic systems in enhancing the mobility and control of lifting mechanisms [7]. This is particularly relevant for the proposed system, which requires precise control during the three-axis rotation and upright positioning of heavy vehicle chassis. The optimization of hydraulic components can lead to improved performance, as noted by Yimer and Wang, who explored the design and manufacturing of hydraulic cylinder-based scissor lifts, demonstrating their effectiveness in the automotive sector [8]. In summary, the design and development of a mechanism for positioning heavy vehicle chassis requires a multifaceted approach, encompassing structural analysis, stability considerations, and the integration of advanced hydraulic systems.

Unlike previous studies that primarily focus on the design, analysis, or operational improvements of scissor lift mechanisms in isolation, this study aims to develop a comprehensive positioning system specifically tailored for heavy vehicle chassis. By integrating a scissor lift platform capable of precise three-axis rotation and an upright positioning mechanism, this research addresses the challenges posed by the excessive weight and large dimensions of heavy vehicle chassis. The proposed system is designed not only to optimize load distribution and structural strength but also to enhance maneuverability, operational efficiency, and stability during positioning operations. Through finite element analysis (FEA) and prototype testing, the study validates the system's structural integrity, ensuring its capacity to handle significant mechanical stresses and deformations. Additionally, the system's modular design facilitates easier maintenance and future upgrades, contributing to long-term operational reliability. The incorporation of hydraulic components further enhances precision, enabling seamless control during chassis rotation and positioning tasks. The findings of this research provide a practical and scalable solution for automotive and heavy vehicle industries, potentially setting a benchmark for similar applications in the manufacturing and maintenance sectors. By addressing key engineering challenges such as load distribution, structural resilience, and system adaptability, this study contributes a novel and efficient approach to heavy vehicle chassis positioning technology.

2. Materials and Methods
2.1. 3D modeling and system design
The 3D modeling process was carried out

using CAD software, which enabled the creation of precise models for all components of the system. The software allows detailed geometric accuracy and facilitated assembly and motion analysis to ensure compatibility between parts. During this phase, the system was also simulated under different conditions to anticipate and address potential issues. In the system design phase, key factors such as functionality, durability, and ease of use were prioritized. The design focused on structural integrity, with components arranged to withstand the forces encountered during operation. Modular structures were used to simplify maintenance and repairs, while ergonomic considerations were made to ensure operator's safety and comfort. Energy efficiency was another critical aspect, particularly in the hydraulic systems that powered the three-axis rotation and upright positioning. By optimizing fluid dynamics and system layout, the design aimed to improve operational efficiency while reducing energy consumption. The final design also emphasized safety, ensuring that all components were capable of withstanding high loads without failure. The 3D model of the system was refined through an iterative review process, resulting in an optimized design ready for prototype production. The complete model, shown in Figure 1, includes all key components such as the chassis tilting mechanism and scissor lift platform.

2.2. Finite element analysis for structural integrity

The Finite Element Analysis (FEA) was conducted to evaluate the structural integrity of the system under operational conditions. In this analysis, standard gravitational acceleration (9.81 m/s²) was applied to simulate real-world loading conditions. Steel material properties were assigned to all components, with an elasticity modulus of 210 GPa, Poisson's ratio of 0.3, and a density of 7850 kg/m³, which are typical for structural steel used in heavy machinery applications [9].

In this study, the structural analyses of the developed system were performed using a nonlinear finite element model. The Second Piola-Kirchhoff stress method was utilized to model deformations. The Piola-Kirchhoff

tensor is used to represent stress in the reference configuration for finite deformations. The force in the reference configuration is expressed in relation to the relative orientation between the direction of the force and the normal vector of the surface. The Second Piola-Kirchhoff stress is expressed as follows.
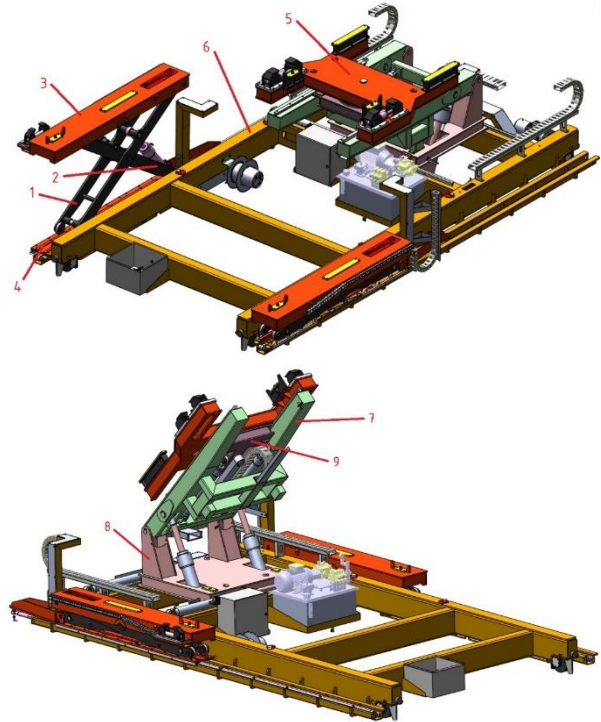
1; outer scissors, 2; inner scissors, 3; scissor lift upper platform, 4; scissor lift lower platform, 5; chassis bracing upper platform, 6; lower chassis, 7; vertical positioner, 8; horizontal positioner, 9; rotation group.
Figure 1. 3D model of the proposed system.

$$S = \frac{FL_0}{A_0 L} = \frac{\sigma_E}{(1+\epsilon_E)} = \frac{\sigma_E}{\lambda} \qquad (1)$$

where F represents the force, L_0 denotes the original length of the part, L represents the final length of the part, A_0 indicates the initial cross-sectional area, σ_E refers to the engineering stress, ε_E represents the engineering strain, and λ denotes the stretch ratio.

Additionally, the matrix compression method [10] was used to reduce the degrees of freedom of each element and optimize the calculations. Mesh convergence analysis was conducted to ensure the accuracy and reliability of the structural analysis results for the chassis positioning mechanism. The analysis aimed to refine the mesh size and increase the number of elements, as shown in Table 1. Despite these refinements, the observed stress values

exhibited minimal differences. For instance, the difference in stress values between the 7 mm and 8 mm mesh sizes was less than 1%. This indicates that the solution is effectively converged. The mesh convergence process was applied to all analyzed components to ensure consistency and optimize computational efficiency.

Table 1. Mesh and stress variations for the model

Mesh size (mm)	Stress value (MPa)	Number of elements
15	198	400
13	212	736
11	215	1404
9	220	3036
8	221	3496
7	221	3956

The system was evaluated in two separate load groups to simulate different operational scenarios. For the chassis tilting mechanism, a distributed load of 5000 kg was applied, considering the weight of the chassis during tilting. For the scissor platform, which operates symmetrically, a distributed load of 2500 kg was applied to each platform. These loads were carefully chosen to reflect the real working conditions of the system.

To ensure the accuracy of the analysis, the structural components were meshed using both 3D and 2D grids, depending on the thickness of the parts. Quadrilateral elements were used for meshing, which are particularly suited for thin-walled components and provide precise results. For the analysis of critical components, triangular elements were preferred for more precise analysis on cylindrical surfaces. Additionally, RBE2 and RBE3 elements were used to model welds and bolt connections, ensuring that the structural integrity of these critical junctions was properly represented [11]. Some examples of the developed finite element model and its mesh structure are presented in Figure 2. The component subjected to the highest load in the developed system is the axle shown in Figure 3. Mesh optimization was performed on this axle, and a mesh size of 8 mm was selected for structural analyses. The results of this optimization were also applied to other critical structural components.

The loading and boundary conditions required for the FEA were defined based on the mechanism's limit position. Figure 4 illustrates the limit loading position of the mechanism. Here, the load was determined using a point mass of 5000 kg concentrated at the center of gravity of heavy vehicle chassis. Boundary conditions were defined by considering the operational characteristics of the components. For the moving parts, single-degree-of-freedom rotational and translational motions were assigned to accurately simulate their functional behavior under real-world conditions. All other parts of the system were assumed to be fixed to ensure stability and represent their stationary nature during operation. A distributed load was applied across the entire system to simulate the external forces acting on the mechanism.
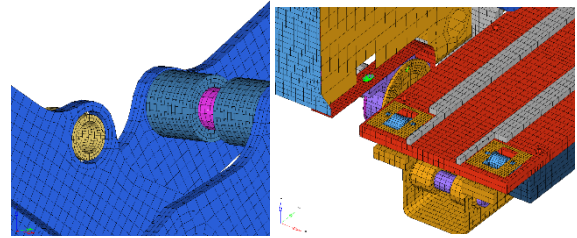

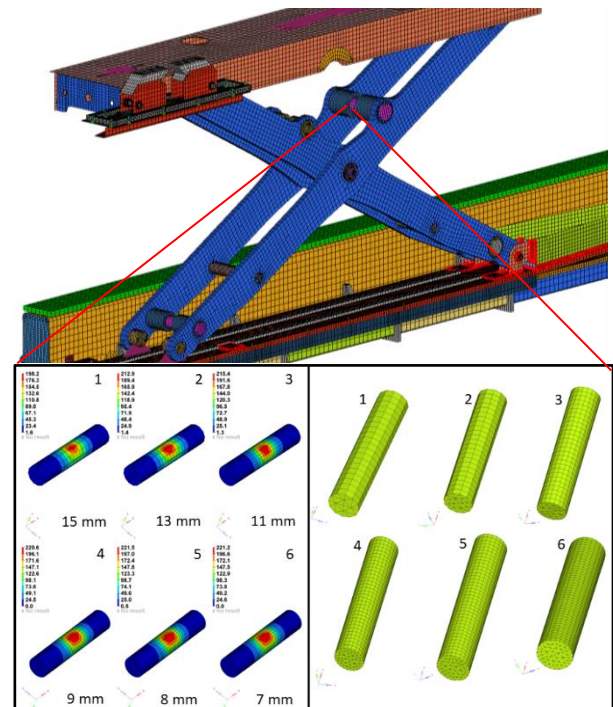Figure 2. Finite element model and mesh types.

Figure 3. Mesh optimization for the critical component.

The FEA results identified key stress concentrations and potential failure points, which will guide the design improvements needed for enhanced durability and safety. By analyzing stress distribution across various

components, such as the chassis tilting mechanism, the scissor platform, and the connecting joints, the FEA provides invaluable insight into the system's performance underload. The results from this analysis form the basis for further optimization of the system's design to improve its strength, reduce material fatigue, and ensure safe operation.
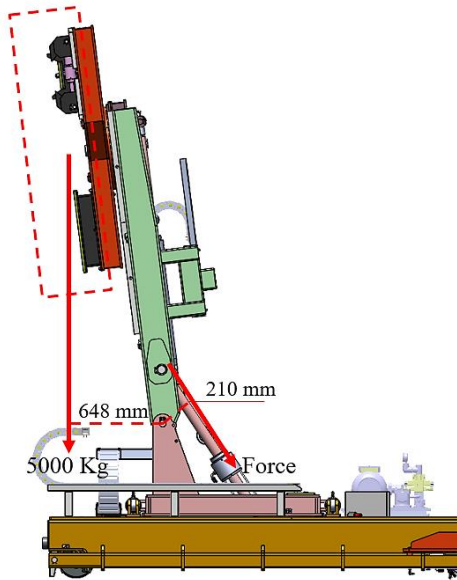

Figure 4. Limit position and loading conditions.

2.3. Prototype production

The prototype production phase was essential for validating the design and functionality of the system developed during the design and modeling phases. This phase involved the physical manufacturing of the components and their integration into a working system. Various production techniques were employed, including CNC machining for precision component fabrication, welded manufacturing for structural integrity, and hydraulic assembly to simulate operational conditions.

CNC machining was used to produce components with high accuracy and tight tolerances, ensuring that the parts fit together seamlessly during assembly. The use of welded manufacturing provided a strong and durable connection for structural parts, particularly for areas subjected to high stress, such as the chassis tilting mechanism and the scissor lift platform. Hydraulic systems were integrated to simulate the real operational conditions of the lift mechanism, allowing for testing of the system's functionality and performance underload.

Once the individual components were produced, the system was assembled, and a series of functional and structural tests were carried out. These tests were designed to assess the system's performance under various operational conditions, ensuring that it met the required standards for stability, durability, and safety. Durability tests involved subjecting the system to repetitive loading and unloading cycles to evaluate wear resistance, while safety tests focused on the performance of the system under extreme loads and operational stresses.

The findings from these prototype tests provided valuable insights into the system's behavior, highlighting areas where design improvements were needed. Modifications were made to enhance the system's performance, such as reinforcing critical stress points and optimizing the hydraulic components for better efficiency and control. An illustration of the prototype and testing processes is shown in Figure 5, highlighting the real-world implementation and functionality of the system.
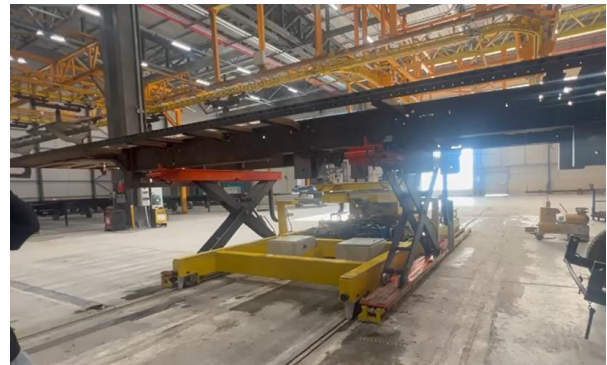
Figure 5. Final version of the system for positioning heavy vehicle chassis.

3. Results and Discussion

This section presents the structural analysis results of the developed system, conducted using the finite element method. The structural analysis results of the developed system, conducted using the FEM, reveal critical stress points in various components of the chassis tilting mechanism. The highest stress observed in the upper structure of the chassis tilting mechanism was 31.4 MPa, as shown in Figure 6(a), indicating a key point that affects overall stability. In the chassis rotation structure, the highest stress value of 32.8 MPa, presented in Figure 6(b), highlights the importance of optimizing this area for improved rotational

stability. The tilting arm experienced a stress of 152.6 MPa, shown in Figure 6(c), which suggests a need for reinforcement to prevent deformation under heavy loads.

design optimization to enhance wear resistance. Finally, the fixed chassis module, exhibiting the highest stress of 190.2 MPa as depicted in Figure 6(e), underscores the need for strengthening to ensure stability and prevent failure under operational conditions. These results provide valuable insights into future design adjustments to improve the system's performance and durability.

Figure 6. Stress analysis results.

The horizontal sliding module, with a maximum stress of 185.0 MPa as seen in Figure 6(d), also indicates a potential area for
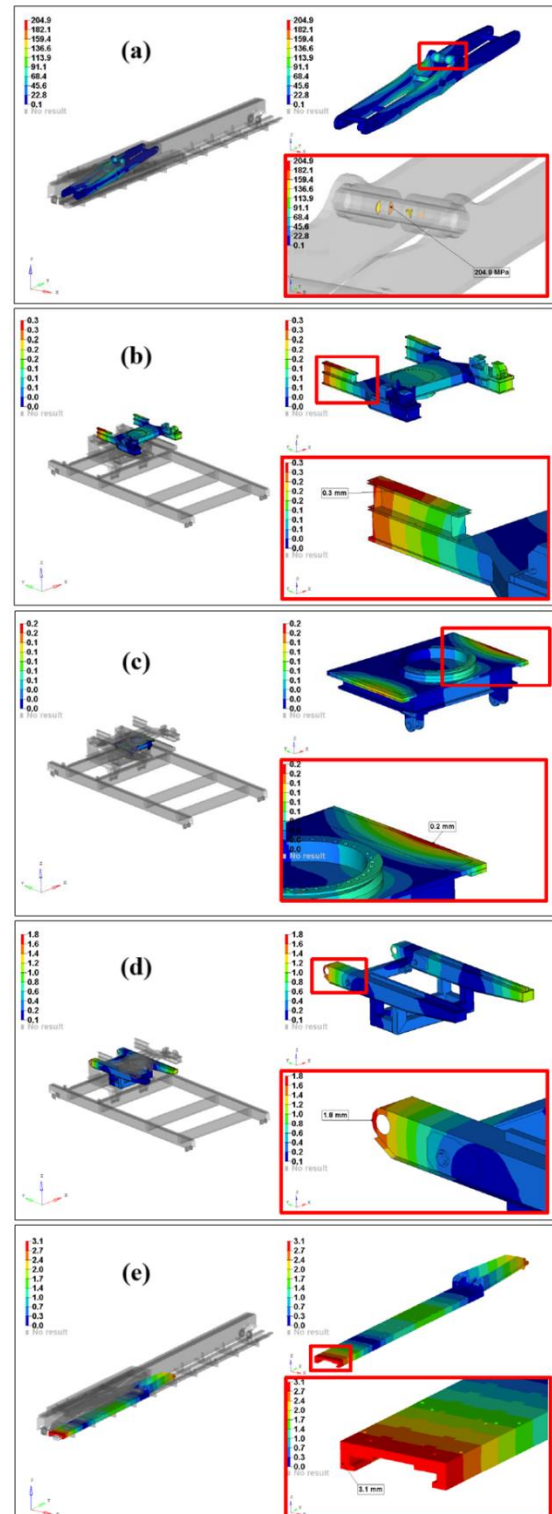
Figure 7. Stress and displacement analysis results.

The structural analysis results also revealed key displacement values observed in various components of the system. The highest stress observed in the outer scissor module of the scissor platform was 204.9 MPa, located at the position indicated in Figure 7(a). Regarding displacement, the highest value in the upper structure of the chassis tilting mechanism was 0.3 mm, as shown in Figure 7(b). The highest displacement in the chassis rotation module of the chassis tilting mechanism was 0.2 mm, located at the position indicated in Figure 7(c). In the tilting arm of the chassis tilting mechanism, the maximum displacement value was 1.8 mm, as shown in Figure 7(d). Finally, the highest displacement observed in the module where the scissor platform slides was 3.1 mm, located at the position indicated in Figure 7(e). These displacement values highlight areas of potential movement and deformation, which are critical for ensuring the system's stability and performance underload.

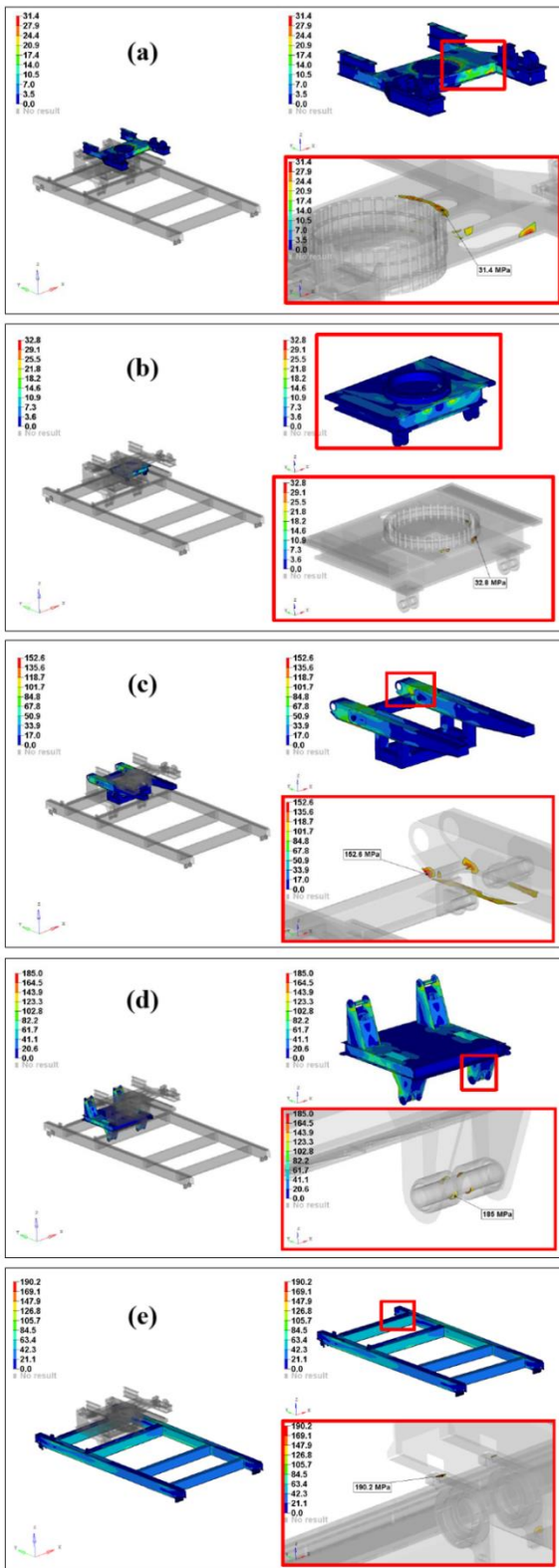The results obtained from the FEA and prototype testing provide valuable insights into the performance and structural integrity of the proposed heavy vehicle chassis positioning system. The FEA results revealed critical stress points in various components of the system, such as the chassis tilting mechanism, scissor platform, and connecting modules. These findings align with previous studies on scissor lift systems, which emphasize the importance of optimizing load distribution and stress concentration to ensure the system's durability and safety under operational conditions.

In particular, the high stress observed in the fixed chassis module (190.2 MPa) and the tilting arm (152.6 MPa) indicate that these components are subjected to significant forces during operation. These results suggest that the design of these parts should be reinforced to prevent potential failures due to excessive stress. The stress values in other components, such as the horizontal sliding module (185.0 MPa) and the chassis rotation structure (32.8 MPa), also highlight areas where optimization could reduce wear and enhance long-term reliability [12].

The displacement analysis further corroborates the findings from stress analysis, with areas of the system, such as the scissor platform sliding module (3.1 mm displacement), exhibiting noticeable movement underload. This displacement is within acceptable limits for functionality but could lead to long-term issues if not addressed, particularly in terms of wear and potential misalignment over time. The displacement observed in the tilting arm (1.8 mm) and upper structure (0.3 mm) also provides useful data for assessing the system's operational stability and guiding future design improvements [13].

The prototype production phase was crucial for testing the real-world applicability of the design. The functional and structural tests confirmed the system's ability to handle the stresses and displacements predicted by the FEA, but they also revealed areas where further refinements were needed. The feedback from the prototype tests highlighted the importance of optimizing hydraulic components to improve performance and reduce operational inefficiencies. Additionally, reinforcing critical components, such as the tilting arm and the fixed chassis module, could further enhance the system's longevity and load-bearing capacity.

One notable contribution of this study is the development of a comprehensive positioning system that integrates both scissor lift mechanisms and an upright positioning mechanism. This integrated system addresses the unique challenges posed by heavy vehicle chassis, which require precise, stable, and reliable positioning during various operational tasks [14]. The ability to rotate and position the chassis along three axes adds versatility and control, making the system an effective solution for industries such as manufacturing, maintenance, and painting, where accurate positioning of large, heavy components is essential.

Despite the promising results, some limitations were identified during testing. For instance, the system's overall efficiency could be improved by further optimizing the hydraulic and mechanical components to reduce energy consumption and enhance operational speed. Additionally, long-term testing under varied conditions is required to assess the system's performance in real-world environments and ensure its reliability over time.

4. Conclusion

This study presents the design and analysis of

a positioning system for heavy vehicle chassis, incorporating a scissor lift platform with three-axis rotation and upright positioning mechanisms. Finite element analysis (FEA) identified critical stress points and displacement values, guiding design improvements for structural integrity and performance. Prototype testing confirmed the system's functionality, with minimal deformation under load, ensuring operational efficiency and safety. The prototype tests were based on field trials under the system's actual working conditions. Observation-based results were obtained after extended periods of operation. One of the future studies involves preparing an appropriate experimental setup to compare experimental data with FEA results.

The results validate the proposed system's effectiveness, providing a reliable solution for heavy vehicle chassis positioning. In another future work, additional improvements could focus on reducing the weight of the system's components, increasing modularity for easier maintenance, and enhancing the user interface for better control and monitoring of the system during operation. Further research could also explore alternative materials for component fabrication, which could reduce wear and improve energy efficiency. Ultimately, the goal is to refine the system to offer a more sustainable and cost-effective solution for heavy vehicle chassis positioning.

CRediT authorship contribution statement

Tolga Güney: Conceptualization, Investigation, Methodology, Writing-Original Draft.
Sinan Düzenli: Conceptualization, Investigation, Methodology, Writing-Original Draft.
Kasım Serbest: Conceptualization, Investigation, Writing-Final Draft, Supervision.

Declaration of Competing Interest

The authors declare no conflict of interest.

Acknowledgement

5. References

1.   Chen, J., Xue, Y., and Zhang, F., Mechanical analysis and finite element simulation of scissor transmission mechanism under partial load, Key Engineering Materials, 667, 518-523, 2015.
2.   Zhang, W., Zhang, C., Zhao, J., and Du, C., A study on the static stability of scissor lift, The Open Mechanical Engineering Journal, 9(1), 954-960, 2015.
3.   Podkowski, K., Okruch, Ł., Jasiński, P., and Stańko-Pająk, K., Strength numerical analyses of the construction of the PAWO autonomous high mobility platform, XII International Science-Technical Conference Automotive Safety, 2020.
4.   Solmazyiğit, İ., Başkurt, R., Ovalı, İ., and Tan, E., Design and prototype production of scissor lift platform 25 tons capacity, The European Journal of Research and Development, 2(4), 326-337, 2022.
5.   Petrů, M., Lepšík, P., Novák, O., and Lufinka,A., Numerical modelling and experimental measurement of lifting platform construction for car relocation, Applied Mechanics and Materials, 732, 219-222, 2015.
6.   Zhao, X., Li, T., Fang, X., Liang, P., Yang, Z., Liu, J., and Yang, Y., Design Optimization of an Electric Positioning Mechanism, Journal of Engineering Mechanics and Machinery, 7(4), 44-52, 2022.
7.   Kart, S., Conceptual design and prototype production of innovative hydraulic walking power steering controlled scissor lift platform, The European Journal of Research and Development, 3(4), 195-204, 2023.
8.   Yimer, W., and Wang, Y., Design, analysis and manufacturing of double scissors lift elevated by one hydraulic cylinder, International Journal of Engineering Research & Technology, 8(11), 709-713, 2019.
9.   Dao, N.D., and Ryan, K.L., Computational simulation of a full-scale, fixed-base, and isolated-base steel moment frame building tested at E-defense, Journal of Structural Engineering, 140(8), A4014005, 2014.
10.   Chang, S., Liu, K., Yang, M., and Yuan, L., Theory and implementation of sub-model method in finite element analysis, Heliyon, 8(11), 2022.
11.   Legrain, G., Geuzaine, C., Remacle, J.F., Moës, N., Cresta, P., and Gaudin, J., Numerical simulation of CAD thin structures

using the eXtended Finite Element Method and Level Sets, Finite Elements in Analysis and Design, 77, 40-58, 2013.

12. Wang, W., Huang, B., Du, J., and Cheng, S., Structural optimization for stiffness and stochastic fatigue life improvement of a sport utility vehicle chassis, IOP Conference Series: Materials Science and Engineering, 692(1), 012030, 2019.

13. Tang, C., He, L., and Khajepour, A., Design and analysis of an integrated suspension tilting mechanism for narrow urban vehicles, Mechanism and Machine Theory, 120, 225-238, 2018.

14. Cui, Z., Xu, H., Chen, Z., Yang, H., Huang, S., and Gong, M., Design of a novel AGV with automatic pick-and-place system based on scissor lifting platform, Chinese Automation Congress (CAC), 4435-4440, 2020.
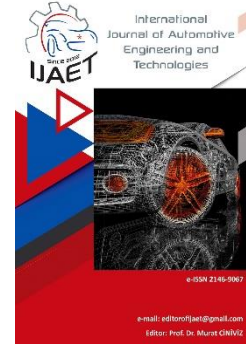
Original Research Article

Investigation of the effect of bath temperature on Ni-W/Al$_2$O$_3$ nanocomposite coatings produced by electrodeposition method

hosted by
Turkish JournalPark ACADEMIC

Yusuf Aybacı[1], Fatih Yalyanç[2], Fatma Nur Kocabuğa[3], Ömer Hükümdar[4, *], Umut Kumlu[5], Ali Keskin[6], Mustafa Atakan Akar[7]

[1,2,3,4*,5,6,7] Çukurova University, Department of Automotive Engineering, 01330, Adana, Türkiye.

ARTICLE INFO

ABSTRACT

In this study, Ni-W/Al$_2$O$_3$ nanocomposite coatings were applied via the direct current electrolysis method on the St-37 steel substrate using a Watts bath. Ni-W alloy coating was obtained by adding sodium tungsten dihydrate as a tungsten source to a Watts-type nickel bath, and then aluminum oxide (Al$_2$O$_3$) ceramic nanoparticles were added to this solution to obtain a nanocomposite coating. The effect of different temperatures (25ºC, 60ºC) on Ni-W and Ni-W/Al$_2$O$_3$ coatings was investigated and detailed research was carried out on the hardness, surface morphology and wear resistance of the coatings. When the raw information of this study was examined in a logical order, the changes in the hardness of the material and the changes in its mechanical properties showed the effect of temperature on the coating. In general, the surface morphologies of the nanocomposite coatings exhibited a smooth and homogeneous distribution. According to the wear analysis results, with the addition of tungsten element to the main matrix, the average friction coefficient decreased by 36.51% at 25ºC and 46.03% at 60ºC compared to pure nickel. With the addition of Al$_2$O$_3$ nanoparticle to Ni-W alloy, the average friction coefficient increased by 12.5% at 25ºC and 2.94% at 60ºC compared to Ni-W alloy. Microhardness results showed that the hardness values increased with the increase in bath temperature. The hardness value of the Ni-W alloy coating obtained at the bath temperature of 60ºC increased by 6.43% compared to the coating obtained at 25ºC. The hardness value of the Ni-W/Al$_2$O$_3$ nanocomposite coating obtained at 60ºC increased by 8.72% compared to the coating obtained at 25ºC.

Keywords: Electrodeposition, Nanocomposite, Microhardness, Aluminum oxide, Wear

1. Introduction

The exposure of metallic parts to abrasion and corrosion in industrial environments has led to the need to improve the mechanical properties of materials. There are many solutions for this, but the most effective one is the electroplating process [1]. Electroplating is a process of electrodeposition whereby a dense, uniform and adherent coating is produced on a surface, typically comprising metals or alloys [2].

Nickel-based coatings, one of the metals widely used in electroplating, stand out with their good corrosion properties, wear resistance, and ductility [3]. Nickel-based coatings are frequently preferred in industrial areas such as automotive, aircraft, space, and mining due to the advantages they offer [4]. Nickel coatings are strengthened by metallic particles added to the solution during electrolysis. The coatings formed because of this process are called alloy coatings. Composite coatings are obtained by adding ceramic particles to this alloy coating. Composite coatings have superior mechanical properties to simple metal or metal alloy coatings [5]. Alloy coatings include varieties such as Ni-P [6], Ni-B [7], Ni-Cu [8], Ni-Fe [9], Ni-Ag [10]. In addition, Ni-W coatings attract attention due to the high wear resistance and hardness they offer [11]. Due to these properties, Ni-W coatings stand out in the industry [12]. However, the use of second-phase particles is also important to increase coating efficiency. Silicon carbide (SiC) [13], zirconium oxide (ZrO_2) [14], titanium nitride (TiN) [15], titanium oxide (TiO_2) [16], cerium oxide (CeO_2) [17], titanium carbide (TiC) [18], boron carbide (B_4C) [19], silicon nitride (Si_3N_4) [20], silicon oxide (SiO_2) [21] are widely used nanoparticle types. Another particle widely used in recent years is Al_2O_3 due to its resistance to corrosion and the hardness it adds to the material [22]. Sridhar et al. [23] employed an electrolytic coating process on Ni-W alloys, modifying the temperature parameters. The coating thickness exhibited a 22% increase at the maximum temperature tested. Conversely, an increase in tungsten content in the alloy was observed in the experiment conducted by increasing the current at room temperature, reaching a value of 31%. Fan et al. [24] studied electroplated Ni-W alloy and Ni-W/Al_2O_3 composite coatings. The current density was determined as 5 A/dm^2, temperature as 50ºC, and pH value as 8. As a result, no cracks or damage had lower hardness but better elastic modulus. Sangeetha et al. [25] produced Ni-W/BN nanocomposite coatings on mild steel substrate using direct current and pulse current. The electrolytic process was carried out by adding 2-8 g/L BN nanoparticles to the nickel sulfate bath. BN improved the corrosion resistance and tribological properties of the nanocomposite coatings in the bath. Compared to the coatings produced using pulse current, the corrosion resistance, microhardness, and surface properties of the coatings produced with DC current showed less improvement. Beltowska-Lehman et al. [26] produced Ni-W/ZrO_2 nanocomposite coatings by electrochemical deposition method in a sulfite-citric electrolysis solution. Researchers investigated the bath parameters by changing the bath parameters, such as ZrO_2 particle bath content, current density, hydrodynamic conditions, and frequency. Researchers used approximately 5 g/L nanoparticle content in the coating bath, 600 RPM cathode rotation speed, DC current, and 11 A/dm^2 current density combinations. As a result, the coatings were found to have an approximate hardness value of 8 GPa, wear value of 1.4 10^{-6} mm³/Nm, and corrosion value of 6 µA/cm². Gyawali et al. [27] produced Ni-W/Si_3N_4 nanocomposite coatings with different amounts of tungsten content. Researchers evaluated the wear and microhardness values of nanocomposite coatings by EDS, SEM, XRD and wear test. The researcher's findings showed that the addition of Si_3N_4 and high tungsten addition improved the wear resistance and hardness of the coatings. Also, the coatings with 12.7% W and 2.1% Si_3N_4 content showed the best wear resistance. Liu et al. [28] produced Ni-W/TiN composite coatings using the pulsed current electrolysis method. Researchers investigated the hardness, wear, and microstructure of TiN concentrations prepared using 4, 8, 12, and 16 g/L amounts. Researchers observed that the densest surface structure, the highest microhardness (897.6 HV), and the best wear resistance were observed in the concentration prepared with 8 g/L. They measured the TiN content in this composite as 8.1%. Shakoor et al. [7] Ni–B/Al_2O_3 composite coatings were synthesised via an electroplating process, whereby Al_2O_3 particles were added to a Ni–B matrix. The addition of Al_2O_3 to the Ni–B matrix resulted in a notable enhancement in the crystallinity of the structure. The surface morphology study revealed the formation of a smooth, dense and fine-grained deposit on both the Ni–B and Ni–

B/Al$_2$O$_3$ composite coatings. However, the addition of Al$_2$O$_3$ particles to Ni–B coatings result in a notable increase in surface roughness. Nanoindentation results demonstrate that the incorporation of Al$_2$O$_3$ into the Ni–B matrix significantly enhances the mechanical properties (hardness and elastic modulus) of the composite, which can be attributed to the dispersion hardening of the Ni–B matrix by the Al$_2$O$_3$ particles. In this study, the effects of direct current electroplating of Ni-W reinforced with Al$_2$O$_3$ were investigated. As a result of this experiment, Ni-W composite coatings reinforced with Al$_2$O$_3$ were produced in baths at different temperatures, and the hardness values, wear resistance, and surface quality were investigated. The expected benefits of Al$_2$O$_3$ reinforcement particles used in electroplating include extending the service life of the part, increasing impact resistance, and creating a more wear-resistant surface. The primary goal is to improve material quality and investigate the effect of temperature on the coating.

2. Experimental Section

In this experimental study, St-37 steel was used as the cathode, graphene rod as the anode, and a reference electrode. Anode and cathode materials were placed vertically in the bath to be coated, with a distance of 20-30 mm between them, and the surface area of the sample to be coated was set as 4 cm^2. The electrodeposition device arrangement is given in Figure 1.
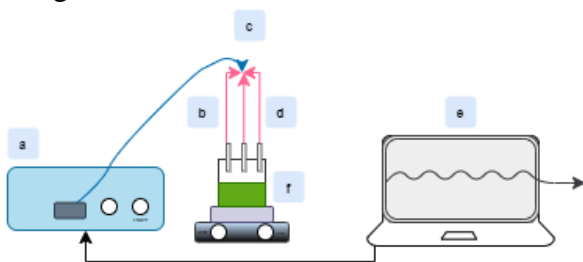
Figure 1. Electrodeposition device arrangement (a) Potentiostat/galvanostat, b) Graphene rod, c) St-37 plate, d) reference electrode, e) computer, f) magnetic stirrer)

Aluminum oxide particles were used with 99% purity and 180 nm size. To make the mixture homogeneous, first, Al$_2$O$_3$ nanoparticles and sodium dodecyl sulfate (SDS) were added to pure water and mixed for 30 minutes; then

other bath components were added and mixed in an ultrasonic mixer for another 30 minutes. Bath concentrations and parameters are given in Table 1 and Table 2.

Table 1. Bath Components

Bath Components (Chemicals)	Amount
Nickel-Sulphate-Hexahydrate	16 g/L
Sodium Tungsten	46 g/L
Ammonium Chloride	26 g/L
Sodium Bromide	15 g/L
SDS	0.5 g/L
Tri Sodium Citrate	142 g/L
Aluminum Oxide (Reinforcement Particle)	5 g/L

Table 2. Operational parameters

Working Conditions	Parameters
Electrolyte Bath pH	9 ± 0.1
Temperature	25°C and 60°C
Bath Shaking Using a Magnetic Stirrer	300 ± 50 rpm
Time (Coating Deposition)	30 min
DC Current Density	50 mA/cm^2

Boric acid or NaOH solution was used to adjust the pH of the electrolytic bath to 9. The temperature of the bath solution was set at 25 ºC and 60 ºC. Before electroplating, St-37 steel material was sanded with 320-600-1200-2000 grit sandpapers, respectively, and then the sample was cleaned in an ultrasonic bath with 20% acetone solution for 30 minutes to remove chemical oils. For the etching process, it was kept in a 10% HCl acid solution for 1 minute. After these processes, the cathode sample was rinsed with pure water and immersed in the electrolyte bath, and the magnetic stirrer was operated at 300 ± 50 rpm to prevent agglomeration of ceramic particles during electrolysis. The current density and pH were kept constant throughout the coating process, and the mechanical properties of the coated samples were analyzed. The number of samples coated, and the bath concentrations of these samples are given in Table 3.

3. Characterization Techniques

The coated samples were examined under the Dino-Lite AM7115MZT model microscope (250x) given in Figure 2.
The homogeneity, smoothness and possible surface defects of the coating were observed.

Table 3. Number of samples coated and their corresponding bath concentrations

Sample (Code Names)	Composition	Temperature (ºC)
N	Pure Nickel	60
NW25	Ni-W	25
NW60	Ni-W	60
NWA25	Ni-W/Al$_2$O$_3$	25
NWA60	Ni-W/Al$_2$O$_3$	60

Figure 2. Optical microscope testing device

The wear performance of the samples was tested using the ball-disc method and the alternating motion test module. 100Cr6 stainless steel was used as the ball material and the ball diameter was selected as 6 mm. The test was carried out with 2 N load and 2 Hz speed, and the wear test was carried out using the UTS Tribology test device, which can perform tests in accordance with ASTM G133M, ASTM-G99, DIN-50324 standards. The wear test device is shown in Figure 3.
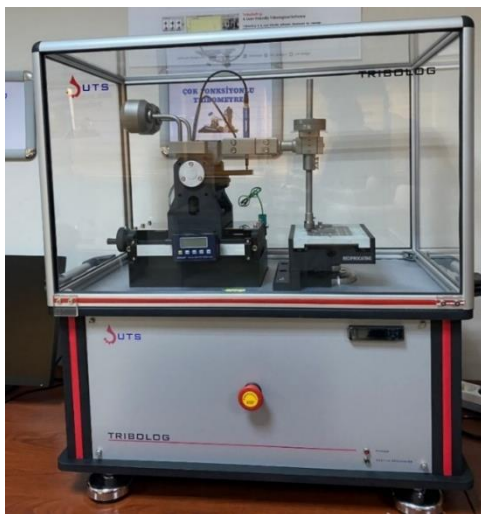
Figure 3. Tribology testing device

For the hardness test, 500 g load was applied to each sample from 10 different points and the hardness value was obtained for 10 seconds. The average of the obtained results was taken and accepted as the Vickers hardness value. Figure 4 demonstrates the Vickers hardness testing device.
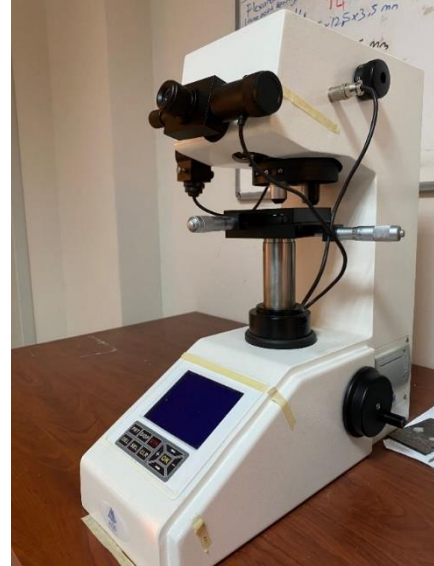
Figure 4. Hardness testing device

4. Results and Discussion
4.1. Surface morphology

Figure 5 shows surface images obtained with a Dino-Lite AM7115MZT model microscope at 250x magnification.

According to the surface morphology findings obtained from the images, the effect of different temperature conditions on the surface properties was observed. While the surface morphology of pure nickel in Figure 4a shows a smooth surface quality, surface defects such as certain roughness and darkening are seen in the surface images obtained from other coatings. In Figure 4b, the surface image of the Ni-W coating produced at 25ºC exhibits a relatively smoother surface structure compared to Figure 4c, while the metallic particles accumulated on the surface show a more homogeneous distribution. This situation showed that the particles added to the Ni main matrix increased the surface roughness. When compared in terms of the effect of Al$_2$O$_3$ nanoparticles, it was clearly seen that the surface morphology of Ni-W/Al$_2$O$_3$ composite coating performed at 60ºC was more scattered and rougher compared to Ni-W coating performed at 60ºC, thus revealing the effect of added Al$_2$O$_3$ particles on the coating.
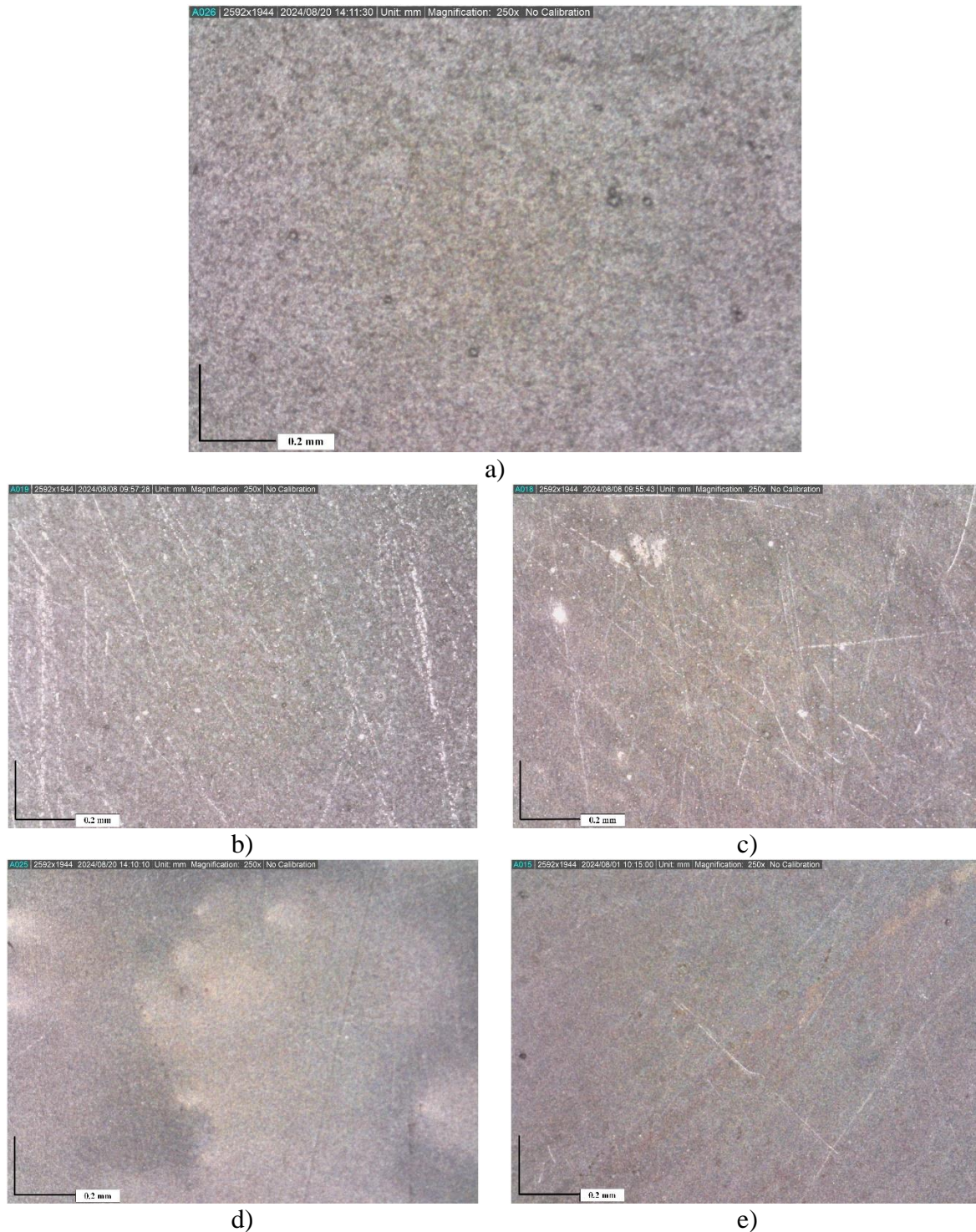
Figure 5. Optical microscope images of the coatings (a) N, b) NiW25, c) NiW60, d) NiWA25, e) NiWA60)

When compared in terms of temperature, a rough surface was seen according to Figure 4d and Figure 4e. The data indicates that elevated temperatures facilitate a more manageable surface during the coating process, thereby reducing the incidence of defects. In general, these findings indicate that coatings at higher temperatures provide better surface quality and minimize surface roughness, and Al_2O_3 additive affects the surface smoothness. All the findings show that the effect of temperature during the coating process plays an important role on the surface morphology. Shakoor et al. [7] demonstrated that the incorporation of Al_2O_3 particles into Ni–B/Al_2O_3 composite coatings resulted in the formation of a smooth, dense, and fine-grained deposit on the surface morphology of both Ni–B and Ni–B/Al_2O_3 composite coatings. Nevertheless, the incorporation of Al_2O_3 particles into Ni–B coatings led to a considerable enhancement in surface roughness.

4.2. Microhardness analysis

The hardness values of Ni-W and Ni-W/Al_2O_3 electroplating obtained at different temperatures are given in Figure 6 for comparison.
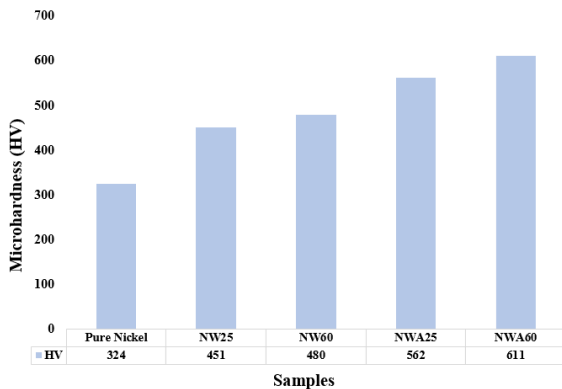
Figure 6. Microhardness values

Microhardness values clearly reveal the effect of temperature on the coated materials. The hardness result of pure nickel was measured as 324 HV. However, tests conducted on Ni-W coating showed that while the hardness value was 451 HV at 25ºC, this value increased to 480 HV when the bath temperature was increased to 60ºC. According to these results, increasing the bath temperature in Ni-W coating leads to an increase in the hardness value. According to these results, a 6.5% increase in the hardness value is observed when the temperature is increased from 25°C to 60°C in Ni-W alloy coating. In addition, a more significant increase in hardness was observed with the increase in temperature in Ni-W/Al_2O_3 nanocomposite coatings. The hardness value of the nanocomposite coating at 25ºC was found to be 562 HV, while when the temperature was increased to 60ºC, the hardness value increased to 611 HV. Accordingly, the hardness values of Ni-W/Al_2O_3 nanocomposite coatings at 60°C increased by 8.72% compared to 25°C. If all the results are compared with pure nickel, with the addition of tungsten element to the pure nickel structure, the microhardness value increased by 39.20% at 25ºC, while a hardness increase of 48.20% was observed at 60ºC. Similarly, when pure nickel is compared with Ni-W/Al_2O_3 composite coatings, a 73.5% increase was observed at 25ºC compared to pure nickel, while an 88.6% increase was observed at 60ºC. These findings show that

nanocomposite coatings are more sensitive to bath temperature and hardness data increase more significantly as temperature increases. Temperature sensitivity of Ni-W/Al_2O_3 nanocomposite coatings shows that these materials can provide high performance and durability in industrial applications. As a result, positive effects of increasing bath temperature on the hardness values of coating materials are shown.

4.3. Wear analysis

According to the wear analysis findings, the effects of modifications formed with Al_2O_3 nanoparticles and tungsten at different temperatures on the material performance were remarkable. All these results are given in Figure 7, while the average friction coefficient values are given in Figure 8.
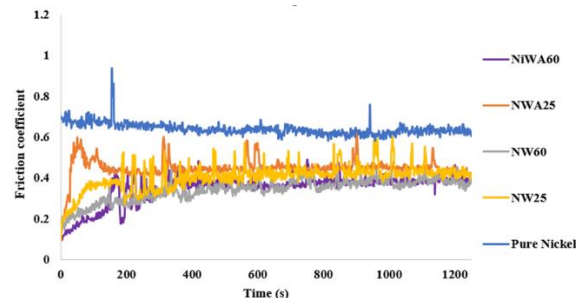
Figure 7. Wear analysis graph of produced samples
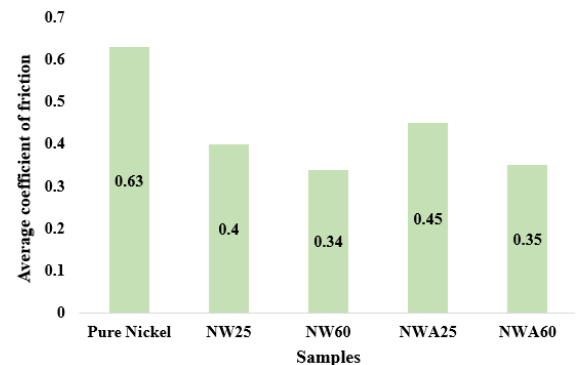
Figure 8. Average Friction Coefficients of Samples

When the results are compared with pure nickel, a significant decrease in the average friction coefficient was achieved with the addition of tungsten to the main matrix. While it was seen that the addition of tungsten reduced the average friction coefficient by 36.51% at 25ºC, these decreases increased to 46.03% at 60ºC. These findings show that tungsten provides a significant improvement in friction and wear and the performance of the material is better improved under high temperature conditions. On the other hand, the

addition of Al_2O_3 nanoparticles to the Ni-W alloy increased the average friction coefficient at both temperatures, showing an increase of 12.5% at 25ºC and 2.94% at 60ºC. This increase means that Al_2O_3 nanoparticles do not reduce the average friction coefficient but rather increase it. The integration of Al_2O_3 nanoparticles with the Ni-W alloy caused the average friction coefficient to change to less than 60ºC. In general, while the addition of tungsten increased the average friction coefficient of the material with wear, the addition of Al_2O_3 nanoparticles increased the friction coefficient at different temperature conditions and revealed a different effect profile. In line with these results, it provides important information to understand the effects of different temperature values on material performance and to determine the compatible material according to the usage conditions.

5. Conclusion

The main goal of this study is to compare the mechanical and wear qualities of samples produced at different bath concentrations by the electrodeposition method. Microhardness results, wear test results and optical microscope examinations of pure nickel, Ni-W alloy and Ni-W/Al_2O_3 composite coatings were comparatively analyzed.

• When the surface appearance of composite coatings is evaluated, it is seen that generally smooth surface coatings are produced. In Ni-W coatings, the surface defects of the coating produced at 60ºC are relatively more than those at 25ºC. When looking at Ni-W/Al_2O_3 composite coatings, the surface of the coatings produced at 60ºC is smoother. As a result, increasing temperature has positive results on the surface morphology of composite coatings.

• In nanocomposite coatings, when microhardness values are examined, the effect of temperature on the coating is clearly seen. The increase in temperature resulted in an increase in the hardness value. When we compare NW25, NW60, NWA25 and NWA60 coatings with pure nickel, an increase in hardness was detected. The best hardness value was the Ni-W/Al_2O_3 nanocomposite coating applied at 60ºC.

• When the wear analysis results are

examined, it is seen that the average friction coefficients of NW25, NW60, NWA25 and NWA60 coatings decrease compared to the pure nickel coating. Accordingly, it was seen that the average friction coefficient was significantly affected by the addition of W and Al_2O_3 to the Ni structure.

As a result of these findings, it is seen that the most optimum coating is the NWA60 coded coating.

Credit Authorship Contribution Statement

The authors' contribution to the study is equal.

Authors' Conflicts of Interest

There are no financial interests or personal relationships that could have influenced the work presented in this article.

6. References

1. M. B. Sohrabi, H. Tavakoli, H. Koohestani, and M. Akbari, "Utilization of Ni-Cu/Al_2O_3 co-deposition composite coatings on mild steel surface via electroplating method and evaluation of its tribological, electrochemical properties", Surface Coating Technology, 475, 2023.

2. K. H. Hou and Y. C. Chen, "Preparation and wear resistance of pulse electrodeposited Ni-W/Al_2O_3 composite coatings", Applied Surface Science, 257(15), 6340–6346, 2011.

3. K. O. Nayana, S. Ranganatha, H. N. Shubha, and M. Pandurrangappa, "Effect of sodium lauryl sulphate on microstructure, corrosion resistance and microhardness of electrodeposition of Ni–Co_3O_4 composite coatings," Transactions of Nonferrous Metals Society of China, 2371–2383, 2019.

4. Ünal, E., Yaşar, A., Karahan, İ.H., "Ni-B Alaşım Kaplamaların Kristal Yapı ve Sertlik Özelliklerine Akım Yoğunluğunun Etkisi", Çukurova Üniversitesi, Mühendislik Fakültesi Dergisi, 37(2), 439-447, 2022.

5. N. P. Wasekar, L. Bathini, L. Ramakrishna, D. S. Rao, and G. Padmanabham, "Pulsed electrodeposition, mechanical properties and wear mechanism in Ni-W/SiC nanocomposite coatings used for automotive applications", Applied Surface Science, 527, 2020.

6. Y. Zhu, J. Wang, H. Liu, P. Ren, and F.

Yan, "Improvement in the corrosion and wear properties of monel 400 alloy by electroless Ni-P deposition in seawater", Material Chemical Physics, 324, 2024.

7. R. A. Shakoor, R. Kahraman, U. Waware, Y. Wang, and W. Gao, "Properties of electrodeposited Ni-B-Al$_2$O$_3$ composite coatings", Material Design, 64, 127–135, 2014.

8. X. Cheng, Y. He, S. Yan, R. Songa, Z. Li, L. Yan, H. Lie, K. Wei, Q. Yuan and S. Xu, "Effect of ZrB$_2$ on the wear resistance and corrosion properties of nanocrystalline Ni-Cu coatings fabricated by electrodeposition", Vacuum, 228, 2024.

9. Y. Li, X. Cai, G. Zhang, C. Xu, W. Guo, and M. An "Optimization of electrodeposition nanocrytalline Ni-Fe alloy coatings for the replacement of Ni coatings", Journal Alloys and Compounds, 903, 2022.

10. D. A. Romanov, V. V. Pochetukha, K. V. Sosnin, S. V. Moskovskii, V. E. Gromov, V. A. Bataev, Y. F. Ivanov and A. P. Semin, "Increase in properties of copper electrical contacts in formation of composite coatings based on Ni-C-Ag-N system", Journal of Materials Research and Technology, 19, 947–966, 2022.

11. Z. Fan, Y. Yang, F. Ba, Z. Chai, L. Zhao, X. Han, Z. Zhang and G. We "Wear mechanisms of Ni–W and Ni–W/Al$_2$O$_3$ composite coatings sliding against Si$_3$N$_4$ and AISI 52100 steel counterbodies", Wear, 554–555, 2024.

12. C. F. Baldessin, T. C. de M. Nepel, and A. F. de A. Neto, "The influence of Ni and Co concentration in the electroplating bath on Ni-Co-W alloys properties", Canadian Journal of Chemical Engineering, 96(6), 1284–1289, 2018.

13. H. Ogihara, H. Wang, and T. Saji, "Electrodeposition of Ni-B/SiC composite films with high hardness and wear resistance", Applied Surface Science, 296, 108–113, 2014.

14. R. A. Shakoor, R. Kahraman, U. S. Waware, Y. Wang, and W. Gao, "Properties of Electrodeposited Ni-B-ZrO$_2$ Composite Coatings", International Journal of Electrochemical Science, 2371−2383, 2015.

15. F. Doğan, M. Uysal, E. Duru, H. Akbulut, and S. Aslan, "Pulsed electrodeposition of Ni-B/TiN composites:

effect of current density on the structure, mechanical, tribological, and corrosion properties", Journal of Asian Ceramic Societies, 8(4), 1271–1284, 2020.

16. Y. Wang, S. J. Wang, X. Shu, W. Gao, W. Lu, and B. Yan, "Preparation and property of sol-enhanced Ni-B-TiO$_2$ nano-composite coatings", Journal Alloys and Compounds, 617, 472–478, 2014.

17. R. A. Shakoor, R. Kahraman, U. S. Waware, Y. Wang, and W. Gao, "Synthesis and properties of electrodeposited Ni-B-CeO$_2$ composite coatings", Material Design, 59, 421–429, 2014.

18. E. Ünal, A. Yaşar, İ. H. Karahan. "Ni-B/TiC Nanokompozit Kaplamaların Korozyon Dayanımlarının Elektrokimyasal Empedans Spektroskopisi (EES) Yöntemi ile Analizi",Çukurova Üniversitesi, Mühendislik Fakültesi Dergisi, 38(1), 115-129, 2023.

19. O. Fayyaz, M. M. Yusuf, S. Bagherifard, M. F. Montemor, and R. A. Shakoor, "Probing into the properties of B$_4$C reinforced nickel phosphorus-based nanocomposite coating", Journal of Materials Research and Technology, 20, 2323–2334, 2022.

20. G. Gyawali, B. Joshi, K. Tripathi, and S. W. Lee, "Preparation of Ni–W–Si$_3$N$_4$ composite coatings and evaluation of their scratch resistance properties", Ceramics International, 42(2), 3497–3503, 2016.

21. Y. Wang, Q. Zhou, K. Li, Q. Zhong, and Q. B. Bui, "Preparation of Ni-W-SiO$_2$ nanocomposite coating and evaluation of its hardness and corrosion resistance", Ceramics International, 41(1), 79–84, 2015.

22. F. Xia, P. Yan, C. Ma, Y. Zhang, and H. Li, "Pulse-electrodeposited Ni/W-Al$_2$O$_3$ nanocomposites at different current densities", Journal of Nanoparticle Research, 25(10), 2023.

23. T. M. Sridhar, N. Eliaz, and E. Gileadi, "Electroplating of Ni$_4$W", Electrochemical and Solid-State Letters, 8(3), 2005.

24. Z. Fan, Y. Yang, F. Ba, Z. Chai, L. Zhao, X. Han, Z. Zhang, G. Wei, "Wear mechanisms of Ni–W and Ni–W/Al$_2$O$_3$ composite coatings sliding against Si$_3$N$_4$ and AISI 52100 steel counterbodies", Wear, 554–555, 2024.

25. S. Sangeetha and G. P. Kalaignan,

"Tribological and electrochemical corrosion behavior of Ni–W/BN (hexagonal) nano-composite coatings", Ceramics International, 41(9), 10415–10424, 2015.

26.   E. Beltowska-Lehman, A. Bigos, P. Indyka, A. Drewienkiewicz, S. Zimowski, M. Kot, M. J. Szczerba, "Optimisation of the electrodeposition process of Ni-W/ZrO_2 nanocomposites", Journal of Electroanalytical Chemistry, 813, 39–51, 2018.

27.   G. Gyawali, B. Joshi, K. Tripathi, and S. W. Lee, "Preparation of Ni–W–Si_3N_4 composite coatings and evaluation of their scratch resistance properties", Ceramics International, 42(2), 3497–3503, 2016.

28.   H. Liu, H. Wang, W. Yu, Y. He, F. Xia, C. Ma and A. Shakoor, "Effect of TiN concentration on microstructure and properties of Ni/W–TiN composites obtained by pulse current electrodeposition", Ceramics International, 47(17), 24331–24339, 2021.
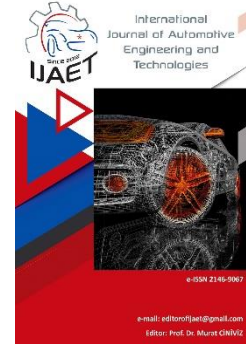
Original Research Article

Evaluation of key fuel properties of three generation biodiesel fuels: an experimental investigation of feedstock type

Hüseyin Şanlı[1], Fevzi Yaşar[2, *]

[1]Tekirdag Namik Kemal University, Corlu Vocational School, Department of Automotive Technology, Tekirdağ, Türkiye.

[2, *] Batman University, Vocational School of Technical Sciences, Department of Refinery and Petro-chemistry, Batman, Türkiye.

ARTICLE INFO

ABSTRACT

Transportation sector is one of the most important causes of environmental problems such as global warming and acid rain. To reduce transportation's negative impacts on the environment, it should be made carbon neutral. Although electrification has been very popular in recent years, internal combustion engines will continue to dominate transportation for a long time. Biodiesel can be produced from varios feedstocks and is classified into three generation according to its feedstock origin. However, the fuel properties of biodiesel fuels of different generations vary significantly depending on feedstock. Biodiesel fuels' physico-chemical fuel properties greatly influence the engine characteristics and exhaust emissions. In this experimental study, 13 different biodiesel fuels' (including three generations) some key fuel properties such as kinematic viscosity, density, flash point, cold filter plugging point and cetane index were determined and compared with each other. The highest and the lowest kinematic viscosities were measured for Waste Cooking Oil Biodiesel and Soybean Oil Biodiesel, respectively. Among the biodiesel fuels, only Waste Cooking Oil Biodiesel and Waste Chicken Fat Biodiesel could not meet the viscosity specification in EN 14214. The density values of test fuels were very similar (between 875.83 kg.m^{-3} and 891.46 kg.m^{-3}) and all were within the required specification range. The lowest flash point (142 °C) was measured for Algae Oil Biodiesel. It was considerably lower than other fuels. The highest flash point (184 °C) belonged to Hazelnut Oil Biodiesel. Waste Fleshing Oil Biodiesel and Waste Cooking Oil Biodiesel had the highest (58.80) and lowest (50.54) cetane values, respectively. However, all biodiesels met the minimum cetane value given in European biodiesel standard. The most significant differences (ranged from -10 °C and 10 °C) between the fuel properties of biodiesels of different origins were observed in CFPP. The viscosity and poor cold flow properties of waste feedstock-based biodiesels may cause critical problems in diesel engines. Nevertheless, they can be blended with other biodiesels or petro-diesel in certain amounts. Among the biodiesel fuels of different origins tested in this study, algae oil biodiesel has the best physico-chemical fuel properties and technical potential.

Keywords: Transportation, carbon neutrality, biodiesel, fuel properties, feedstock.

1. Introduction

Energy can be defined as the ability to do work in its most fundamental meaning.

Nevertheless, energy is the most basic input for many different sectors and a critical requirement for sustainable development, and

it is as important as life itself in today's conditions. Because of the rapid increase in the world population, rising living standards, growing industrial production and logistics needs, world energy consumption is constantly increasing. By the end of 2035, total world energy consumption is estimated to be 779 EJ [1]. Despite important academic and industrial scale studies on many different alternative energy sources, most of the world's energy needs are still met by fossil energy sources and petroleum is still the primary energy source. However, fossil energy resources are generally obtained from certain regions of the world and countries like Türkiye, which do not have sufficient fossil resources, have to spend large amounts of money for energy imports. When today's world is thought geo-politically and geo-strategically, considering the effects of energy dependency in terms of only economically is insufficient. Countries exporting fossil energy sources may use these advantages as a means of blackmail in international relations. In addition to the economic and geopolitical effects of increasing fossil energy consumption, its environmental impact should also be strongly highlighted. Intensive energy usage causes vital environmental problems including global warming, acid rain, etc. These environmental problems are getting worse every year and cause consequences that directly affect human life, such as climate change and decreasing water resources.

Energy consumption is mainly driven by three sectors: industry, households and transportation. In spite of many economic and geopolitical uncertainties in the world, energy demand of the transport sector has been increasing each year, accounting for about 30% of all energy consumed globally. To satisfy this energy need of transportation is crucial for the continuity of the people's mobility and the global supply chain. As an inevitable result of this huge energy consumption, the transport sector accounts for more than a third of CO_2 emissions from end-use sectors and is one of the biggest GHG emissions reasons [2]. According to Net Zero Emissions by 2030 Scenario, CO_2 emissions from transport must be decreased by about a quarter, even though transport demand continues to increase. To achieve this target (sustainable and environmentally friendly transportation), policies need to encourage shifting to less carbon-intensive transport options. Nowadays, electrification of transportation is a very popular issue, and electric vehicles are generally considered as the key technology for the decarbonization of transport sector, especially road transport that accounts for about one-sixth of global emissions. Nevertheless, there are many technical problems and economic uncertainties that should be solved for the widespread electrification of transportation. Because of these reasons, electric vehicles are not yet a global phenomenon in the transport sector. For example, the share of electric cars (battery electric vehicles and plug-in hybrid vehicles combined) in total car sales was about 14% in 2022 (about 10 million worldwide) [3]. One of the most important issues to be emphasized in terms of electrification of transportation is that the electrical energy, which is used to charge the vehicle battery, should be obtained from domestic, renewable, sustainable and environmentally friendly sources. The production of electricity used in battery charging from imported fossil resources by polluting the environment will have a positive effect on reducing imported energy dependency nor on environmental pollution. Considering IEA report stating that only 29% of electricity used for transport sector in 2023 was obtained from renewable sources [4], it can be said that electromobility powered by renewable sources will not be able to solve this problem on its own. It should be strongly stressed that the electrification of transport sectors other than road transport (such as aviation, maritime, rail and even medium- and heavy-duty road vehicles) is very difficult and in some cases impossible. Thus, a very big portion of transportation depends substantially on internal combustion engines running generally on fossil fuels. Among internal combustion engines, diesel engines have higher torque and better thermal efficiency superiorities over gasoline engines. Thus, in comparison to gasoline engine vehicles, diesel engine vehicles have been dominantly used in all transportation sectors. Apart from transport, diesel engines are also used extensively in

many different areas such as construction machinery and generators. Because of this situation, diesel fuel consumption is much higher than that of gasoline.

Taking into consideration these conditions, the importance of renewable, environmentally friendly, sustainable and domestically producible alternative diesel fuel is clearly seen. Biodiesel, which is an alternative diesel fuel, can be utilized in all areas of transport sector including railway, seaway and airway. It is compatible with the existing fuel distribution and station network and does not require significant modification in the engine and fuel injection system of the vehicle [5]. When considered on an industrial scale, factory and infrastructure investment can be realized with smaller budgets compared to other alternative energy types. Since biodiesel fuels can be produced from domestic feedstocks, it can alleviate the dependence on the import energy sources causing account deficit problems. Moreover, biodiesel fuels of all generations, regardless of its feedstock type, have better exhaust emission profile (apart from NO_x) than petro-diesel [6-8]. At finally yet importantly, biodiesel fuel contains carbon absorbed by plants through photosynthesis. When this biodiesel fuel is used in a diesel engine, the carbon released during combustion returns to the atmosphere. Therefore, biodiesel can be accepted as a near zero-emission fuel, and it can be stated that biodiesel fuel will not increase the carbon footprint of the transportation sector [9].

Powering a diesel engine with biodiesel is not a new concept. Considering that Rudolph Diesel, the inventor of the diesel engine, powered his engine on peanut oil, it can be said that the history of biodiesel as a diesel engine fuel is as old as the diesel engine itself. Although powering a diesel engine with crude vegetable oils gave positive results in the short term, serious engine problems were encountered when the operating times were prolonged [10]. The most important reason for these vital engine failures is the unacceptably high viscosity of vegetable oils. The viscosity values of vegetable oils are approximately 15 times higher than that of petro-diesel. This unacceptably high viscosity negatively affects the fuel injection process, resulting in incomplete combustion [11]. In addition, glycerin in the chemical structure of vegetable oil causes the injector needle to stick to the injector nozzle. Coking occurs in the injector and the injector nozzle becomes clogged over time. Cooked and clogged injector nozzles lead to poor atomization quality [12]. Especially during cold starts, unburned fuel adheres to the cylinder walls and as it flows under the cylinder wall, it washes the lubricating oil film here and breaks the lubricating film. As a result of dry friction on the cylinder walls, scratches and abrasions occur on the cylinders over time [13]. Furthermore, unburned fuel goes down to the crankcase and mixes with the lubrication oil and deteriorates the chemical structure of the lubricant. Due to the deterioration of the lubricant quality, the above-mentioned serious engine failures occur in a very short time [14]. In order to avoid the aforementioned serious engine failures, the unacceptably high viscosities of vegetable oils should be decreased to a value close to that of petro-diesel. This viscosity reduction is achieved through the transesterification reaction. As shown in Figure 1, in the transesterification reaction, the triglyceride molecule, which is the main constituent of vegetable oils and animal fats, is chemically broken down by reacting with alcohol in the presence of a catalyst and its glycerin is replaced by the alkyl radical of the alcohol used in the reaction [15]. In a transesterification reaction, three moles of alcohol are theoretically used for one mole of feedstock, but since this is an equilibrium reaction, more alcohol should be used to force the reaction to the products side. The transesterification reaction is also an alcoholysis reaction, and any alcohol can be used in this reaction. However, for both technical and economic reasons, methanol is predominantly used [16]. Therefore, biodiesel is commonly defined as methyl ester (as seen in many fuel standards). Although alkaline, acid or enzyme catalysts can be used to catalyze the reaction, alkaline catalysts (mostly hydroxide catalysts such as KOH or NaOH) are generally preferred as they are much faster than other catalysts [17]. However, when alcohols other than methanol (such as ethanol) are used, better results can be obtained with alkoxide catalysts such as CH_3ONa, CH_3OK

instead of hydroxide catalysts [18]. It should be strongly emphasized that if the free fatty acid (FFA) content of the feedstock used in the transesterification reaction is above 1%, the alkaline catalyst causes saponification problem. In this case, the FFA content of the feedstock can be reduced to below 1% by the acid-catalyzed pre-treatment reaction/s and then the alkaline-catalyzed transesterification reaction (main reaction) can be carried out [19].

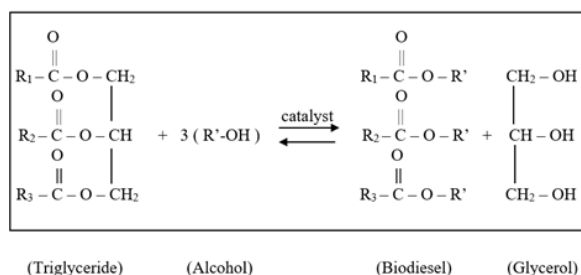(Triglyceride)   (Alcohol)   (Biodiesel)   (Glycerol)

Figure 1. Stoichiometric transesterification reaction

When the chemical structure of any biodiesel fuel is analyzed, it will be seen that it consists of the fatty acid moiety coming from the feedstock from which it is produced and the alkyl radical moiety coming from the alcohol used in transesterification. Although alcohol has effects on the fuel properties of biodiesel, the main determining factor at this point is the biodiesel feedstock [20]. In a transesterification reaction, the fatty acid distribution remains essentially the same and shows itself in the biodiesel fuel obtained. In other words, the fatty acid composition of the biodiesel fuel reflects the fatty acid structure of the feedstock from which it is produced. Because of this, the fuel properties of different origin biodiesels show significant differences. For example, as the fatty acid chain length and saturation level increases, properties such as cetane number, heating value, lubricity and oxidative stability improve, while viscosity and cold flow properties are adversely affected [21-23].

Biodiesel can be obtained from many different feedstocks. Biodiesel fuels produced from conventional edible vegetable oils are classified as the first-generation biodiesel. If a worldwide investigation is conducted, it will be seen that edible vegetable oils including soybean oil, rapeseed oil, palm oil, etc. are the main feedstocks in the global biodiesel production industry. However, since

approximately 75-80% of the total cost of biodiesel fuel is the feedstock price, the unit price of first-generation biodiesel fuel produced from food-grade high quality, but expensive feedstocks are quite high in comparison to petro-diesel [24]. Due to the unacceptably high break-even price of first-generation biodiesel fuels, their marketing is so difficult and consequently the biodiesel industry needs economic incentives, tax reductions, and subsidies. It can be said that first-generation biodiesel industry is not affordable and sustainable.

Waste frying oils, waste animal fats and inedible oils can also be used as feedstock in biodiesel production. Waste feedstock or inedible oil origin biodiesel fuel is classified as the second-generation biodiesel fuel. The usage of waste frying oils and fats as feedstock in transesterification may be beneficial for a sustainable biodiesel industry by alleviating the high-cost problem of biodiesel. Furthermore, by using the waste frying oils and waste animal fats as biodiesel feedstock, the probable environmental problems caused by the disposal of the waste materials may be prevented and also these waste feedstocks will be transformed into a very important and strategic product such as energy. However, this important point should be stressed that FFA content of second-generation feedstocks may be quite high. Thus, alkaline-catalysed transesterification may lead to saponification problem. This can hinder the biodiesel production process and result in significantly lower product yields [25].

Another biodiesel feedstock that is more recent than other feedstocks is algae. A biodiesel fuel obtained from algae oil is defined as the third-generation biodiesel. Compared to other biodiesel feedstocks, algae have many advantages such as not requiring soil for algae production, can be grown in a very short time and can be produced even in wastewater. There are many different algae species and the literature in this field is getting richer every year. However, studies on changing the fatty acid composition of algae according to the fuel properties of the biodiesel to be produced are quite remarkable [26]. For example, in order to produce algal oil-derived biodiesel, which can be mixed with jet fuel at certain ratios in the

aviation sector, the algae feedstock should consist of fatty acids with low freezing point. However, while modifying the genetics of the fatty acid structure of the algae feedstock for this purpose, other critical fuel properties such as kinematic viscosity, calorific value, volatility, etc. should not be adversely affected by this intervention.

In the literature, there are various studies comparing the fuel properties of biodiesel fuels produced from different feedstocks. However, when these studies are examined, it is seen that either the test fuels do not cover all three biodiesel generations or most of the fuel properties are quoted from other studies. When the transesterification reaction parameters and conditions change, the fuel properties of the obtained biodiesel will also change. When the related literature is studied from this perspective, it will be realized that the number of studies comparing the critical fuel properties of biodiesels produced from different feedstocks under the same transesterification reaction conditions, covering all three generations, is quite limited. This experimental study aims to fill this gap in literature partially.

2. Experimental

The physico-chemical fuel properties of different generation biodiesels produced from various feedstocks will also be different. This will significantly affect combustion efficiency, engine performance characteristics, exhaust emissions and engine life. For this reason, in the current study, biodiesel fuels were produced from different feedstocks (including 3 generations) to determine some key fuel properties of biodiesels of different generations. Sunflower oil, hazelnut oil, rapeseed oil, corn oil, soybean oil, olive oil, safflower oil, palm oil as the first-generation feedstocks. Waste frying oil, waste chicken fat, waste fleshing oil and cottonseed oil as second-generation feedstocks. Algae oil (*chlorella protothecoides*) is the third-generation feedstock.

In the production of biodiesel fuels, transesterification reaction conditions were selected as 6:1 molar ratio of methanol to feedstock, 1% KOH, 1 hour, 60 °C. At the end of the reaction, the mixture in the reaction vessel was taken into the separation funnel and

waited overnight for a complete phase separation. After draining the glycerol, the biodiesel fuel was washed 3 times with distilled water at 50 °C and then heated at 101 °C for one hour to dehydration.

Biodiesel fuels are coded as follows: sunflower oil biodiesel (SoB), hazelnut oil biodiesel (HoB), rapeseed oil biodiesel (RoB), corn oil biodiesel (CoB), olive oil biodiesel (OoB), safflower oil biodiesel (SfB), palm oil biodiesel (PoB), soybean oil biodiesel (SyB), cottonseed oil biodiesel (CtB), waste cooking oil biodiesel (WOB), waste chicken fat biodiesel (WCB), waste fleshing oil biodiesel (WFB), algea oil biodiesel (AlB). In order to symbolize the determined fuel properties FP, CFPP, KV, D, and CI stands for flash point, cold filter plugging point, kinematic viscosity, density and cetane index, respectively.

Table 1 shows the measured properties, equipment, and methods used in this study.

Property	Equipment	Method	Accuracy
Density	DMA 38	EN 12185	0.1
Kinematic Viscosity	HVM 472	EN 3104	0.001
Flash Point	HFP 339	EN 3679	0.5
Cold Filter Plugging Point	FPP 5Gs	EN 116	0.1
Distillation Temperatures	Herzog	EN 3405	0.1

In order to calculate the CI values of biodiesel fuels, ASTM D4737-21 method was used:

$CI = 45.2 + (0.0892) (T_{10N}) + [0.131 + (0.901) (B)] [T_{50N}] + [0.0523 - (0.420) (B)] [T_{90N}] + [0.00049] [(T_{10N})^2 - (T_{90N})^2] + (107) (B) + (60) (B)^2$

where:
CI= Cetane Index, D= Density at 15 °C, DN= D-0.85, B= $[e^{(-3.5)(DN)}]$-1, T_{10}= 10% recovery temperature (°C), T_{10N}= T_{10}-215, T_{50}= 50% recovery temperature (°C), T_{50N}= T_{50}-260, T_{90}= 90% recovery temperature (°C), T_{90N}= T_{90}-310.

The determination of distillation temperatures of test fuels can be seen in Figure 2.

3. Results and discussion

The physico-chemical properties of the biodiesel fuels were determined through a series of standardized tests and measurements.

The results obtained for these fuel properties are presented in Table 2 for reference and comparison.

Figure 2. Determination of distillation temperatures of test fuels

3.1. Flash point

Flash point can be described as the minimum temperature at which fuel emits vapor in sufficient concentration to form an ignitable mixture with air near its surface. In other words, the lower the flash point, the easier it is to ignite a fuel [28]. It is generally evaluated in terms of transportation and storage safety; however, flash point is an important fuel property for the operability of a diesel engine. Namely, flash point of a fuel can be useful for providing insight into that fuel's volatility and flammability both of which directly influence easy start in cold weather, combustion and exhaust emissions. A diesel fuel with high

viscosity and flash point may cause difficulties in easy cold-start and also ignition delay time. Moreover, in the literature, there are some studies reporting that high flash points may result in soot formation inside the engine cylinders [29].

Among the fuel properties defined in EN 14214 and ASTM D6751, the only property that has the same specifications is the flash point. Both biodiesel standards require a flash point of minimum 101 °C. This flash point value is considerably higher than that of petro-diesel. The flash point specification required for petro-diesel is min 55 °C in EN 590, while min 52 °C in ASTM D975. This significant difference between the flash points of petro-diesel and biodiesel fuels shows that the logistics and storage of biodiesel are safer than diesel fuel. This is one of the important superiorities of biodiesel over diesel fuel.

As can be seen from Table 2, the FP values of all biodiesel fuels were well above the limit value of 101 °C. The highest (184 °C) and lowest (142 °C) FP values were measured for HoB and AlB fuels, respectively. The most remarkable result here is that there is a significant difference of 26 °C between the FP value of AlB, which has the lowest temperature, and the FP value of WFB (168 °C), which has the second lowest temperature. Similar situation was not observed among biodiesel fuels with high FP values. The difference between the highest FP value (184 °C, HoB) and the second highest FP value (182 °C, OoB) is only 2 °C. The FB values of WCB and WFB, which were biodiesel fuels of waste animal fat origin, were almost the same (169 °C and 168 °C, respectively).

Table 2. Some key fuel properties of biodiesel fuels

Biodiesel	FP (°C)	CFPP (°C)	KV (mm².s⁻¹, 40 °C)	D (kg.m⁻³, 15 °C)	CI
AlB	142	-10	4.49	880.25	55.90
WOB	180	9	6.65	891.31	50.54
WCB*	169	3	5.30	889.70	52.30
WFB*	168	10	4.70	876.70	58.80
CtB	178	3	4.36	884.36	55.82
HoB	184	-10	4.77	879.94	57.70
RoB	180	-10	4.84	885.24	55.83
CoB	176	-9	4.32	879.52	55.48
OoB	182	-6	4.84	890.48	57.09
SfB	174	-9	4.13	887.85	53.74
PoB	172	8	4.55	885.15	56.40
SyB	170	-9	4.11	875.83	51.50
SoB	176	-6	4.45	891.46	51.39

3.2. Cold filter plugging point

Among the physico-chemical properties of a fuel, cold flow properties are the most important features that affect the ability of that fuel to be used without any problems in regions with different weather conditions. A vehicle fuelled in a hot region can move to a region with much lower temperatures during the day and the engine must continue to run smoothly. Although biodiesel is generally used in road transport, projects are being developed for the use of biodiesel fuels in air transportation by blending with jet fuel in certain proportions. This is very important in terms of the usability of biodiesel in all transportation sectors. At this point, the cold flow properties of biodiesel fuels are very critical. The fatty acid distribution of a biodiesel fuel has a significant effect on its cold flow properties. As the fatty acid chain length and saturated fatty acid content increase, the cold flow properties deteriorate. In addition, the alcohol type used in transesterification reaction also affects the cold flow quality. For example, in comparison to methanol, when branched-chain alcohols such as 2-propanol are used, the cold flow properties improve, but when alcohols such as ethanol, n-propanol, n-butanol are used, the fuel begins to freeze at relatively higher temperatures [30].

In general, three concepts (cloud point, pour point, and cold filter plugging point) are used to characterize the cold-flow quality of a liquid fuel. The cloud point is the temperature at which the crystal cloud (wax crystals), which is an indicator of the onset of freezing, first appear on the fuel surface. As the temperature drops, crystallization increases, and consequently the fluidity of the fuel decreases. The pour point is defined as the lowest temperature at which fuel can maintain its fluidity and still be pumped. However, the fuel pumped by the fuel pump can continue to flow in the fuel line, but as a result of gel formation, it cannot pass through the small pores of the fuel filter and clogs the filter, causing the engine to stop. Therefore, pour point may be misleading in order to assess the usability of an engine fuel in cold weather. The cold filter plugging point (CFPP) is the temperature at which the pumped fuel cannot pass through the fuel filter as a result of crystallization, and it is more accurate to use the CFPP value for internal combustion engines [31].

There is no specification for CFPP value in EN 14214 and ASTM D6751. A similar situation is also seen in petro-diesel standards. While ASTM D975 does not specify a CFPP limit, EN 590 has a limit of -15 °C for winter and 5 °C for summer. As can be seen from Table 2, there were significant differences between the CFPP temperatures of biodiesel fuels. The difference between the highest and lowest CFPP values was 20 °C. The lowest CFPP temperature (-10 °C) was measured for RoB, HoB and AlB fuels. The CFPP value (-9 °C) of CoB, SyB and SfB is quite low and ranked second. The CFPP temperatures of SoB and OoB (-6 °C) were acceptable and the last temperature value below zero. It is noteworthy that the CFPP values (3 °C) of WCB, which is of animal fat origin, and CtB, which is of vegetable oil origin (both second generation biodiesels) were the same. WFB had the highest CFPP (10 °C) value among 13 different biodiesel fuels tested. CFPP temperatures of WOB (9 °C) and PoB (8 °C) were also too high and close to that of WFB. The high CFPP results may be caused by these biodiesels' high saturation level.

3.3. Kinematic viscosity

Viscosity, which can be defined as the resistance to flow, is one of the most important physical fuel properties. It should be noted that the main objective of the transesterification reaction is to bring the very high viscosity of triglycerides closer to that of petro-diesel. As the viscosity of the fuel increases, the atomisation quality decreases. Injection of a high viscosity fuel lead to large diameter droplets from the injector nozzle. Since it will take a long time for this relatively large-diameter fuel droplet to evaporate in the cylinder and mix with air, the formation of air-fuel mixture will be insufficient. This will adversely affect combustion efficiency, engine performance and exhaust emissions. In addition, since today's electronically controlled modern fuel injection systems are extremely sensitive to fuel quality, the use of high viscosity fuels may cause fuel pump, injector and engine failures. Also, higher PM emissions resulted by the incomplete

combustion in the engine cylinder may clog the diesel particulate filter of the vehicle in a short time [32].

While the kinematic viscosity specification in EN 14214 is between 3.5-5.0 $mm^2.s^{-1}$, this value is 3.5-6.0 $mm^2.s^{-1}$ in ASTM D6751. The difference of 1.00 $mm^2.s^{-1}$ between the upper viscosity limit of these two biodiesel standards can be critical especially for biodiesel fuels produced from relatively higher saturated feedstocks such as waste animal fats and waste frying oils. It may be useful to remember that the viscosity specification in EN 590 is 2.0-4.5 $mm^2.s^{-1}$, while in the ASTM D975 this range is 1.9-4.1 $mm^2.s^{-1}$. In other words, the upper limit of biodiesel viscosity is higher than that of petro-diesel in both EU and US standards.

Table 2 shows that the viscosity values of 11 biodiesel fuels (except WCB and WOB fuels) were lower than 5 $mm^2.s^{-1}$ and met the EN 14214 standard. The viscosity value of WCB (5.30 $mm^2.s^{-1}$) exceeded the upper limit of the EU biodiesel standard but it met the ASTM D6751. Nevertheless, the viscosity of WOB (6.65 $mm^2.s^{-1}$) exceeded even the upper limit of the ASTM D6751 standard. WOB processed in this study was obtained from a fast-food restaurant and it was palm oil origin. The high saturation level of palm oil and also high molecular weight degradation products (polar materials) resulted by frying process may be possible reasons of this high kinematic viscosity value of WOB.

Another remarkable point in the kinematic viscosity results is that the viscosity value of WFB (4.70 $mm^2.s^{-1}$), a biodiesel of animal fat origin, is lower than the viscosity values of ROB (4.84 $mm^2.s^{-1}$), OoB (4.84 $mm^2.s^{-1}$) and HoB (4.77 $mm^2.s^{-1}$). The viscosity values of vegetable oil based biodiesel fuels varied between 4.11 $mm^2.s^{-1}$ (SyB)-4.84 $mm^2.s^{-1}$ and all of them met the EN 14214 standard. As a third generation biodiesel, the viscosity of AlB (4.49 $mm^2.s^{-1}$) was very close to the first and second generation vegetable oil based biodiesel fuels.

3.4. Density

Density is important in terms of the consecutive breakdown steps of the injected fuel droplet. This will influence the total vaporisation duration and penetration distance of the fuel inside the combustion chamber,

inevitably affecting the combustion kinetics. In the literature, there are studies showing that fuel density has an effect on exhaust emission characteristics, especially NO_x and PM emissions [33]. In diesel fuel injection systems, the volume of fuel discharged by the injector needle moving upwards is sprayed into the cylinder. Therefore, if a high density fuel is used, more fuel mass will be sprayed into the engine cylinder, affecting the air excess ratio in the flame front. In addition, in the studies carried out on diesel engines with electronically controlled fuel injection system, it has been observed that as the fuel density increases, the time between the signal input to the injector and the lifting of the injector needle (response time) increases [34]. This delay in the response time may affect both injection characteristics and combustion characteristics such as ignition delay, start and end of combustion.

The density specification in EN 14214 is 860-900 $kg.m^{-3}$ while ASTM D6751 does not specify any density standard. When diesel fuel standards are analysed, it is seen that there is no density specification in ASTM D975 (as in the biodiesel standard) while the density is required to be 820-845 $kg.m^{-3}$ in EN 590.

As can be understood from Table 2, the density values of all biodiesel fuels were within the range required in EN 14214. Regardless of feedstock and generation, the density values of all biodiesel fuels were very close to each other. The highest density (891.46 $kg.m^{-3}$) and the lowest density (875.83 $kg.m^{-3}$) were measured for SoB and SyB, respectively. The density value of WFB (876.70 $kg.m^{-3}$) was lower than those of all vegetable oil based biodiesel fuels except SyB (875.85 $kg.m^{-3}$) and AlB (880.25 $kg.m^{-3}$). Similar situation was also detected in the kinematic viscosity values of the related fuels. It can be said that the density value of AlB, the third generation biodiesel, was close to that of the 1_{st} and 2_{nd} generation vegetable oil origin biodiesel fuels. As mentioned before, WOB was of palm oil origin. When WOB and PoB fuels are compared, it is seen that similar to the viscosity values, the density value of WOB (891.31 $kg.m^{-3}$) was higher than that of PoB (885.15 $kg.m^{-3}$). This result can be explained by the chemical groups formed as a result of the

degradation reactions in the oil during the frying process and inevitably present in biodiesel fuel.

3.5. Cetan index

Cetane number is one of the most critical fuel properties as it directly affects the combustion process and consequently all engine characteristics. However, before explaining the cetane number and its significant effect on the combustion process, it will be useful to briefly examine the diesel combustion process. Combustion in diesel engines can generally be analysed in 4 stages: 1- Ignition delay, 2- Pre-mixed controlled combustion phase, 3- Diffusion-controlled combustion phase, 4- Post-combustion phase. An ignition delay is the time between the start of fuel injection and the start of combustion. The pre-mixed controlled combustion is the combustion stage in which all of the fuel injected and vaporised into the combustion chamber during the ignition delay period ignites at the same time and can also be referred to as uncontrolled combustion. In the diffusion-controlled combustion, which is the main phase of diesel combustion, the combustion phenomenon (and therefore the temperature and pressure increase) is controlled by the amount of fuel injected onto the flame. Post-combustion is the last stage of the diesel combustion process [35]. In today's modern diesel engines with electronically controlled fuel injection system, a small amount of fuel is injected into the cylinder in this combustion phase in order to reduce HC and especially PM emissions. Cetane number is an indicator of the flammability of a fuel. In other words, fuel with high cetane numbers can burn more easily. The cetane number significantly affects the ignition delay time. As the cetane number increases, the ignition delay decreases. As a result, since the amount of fuel burning at the same time in the pre-mixed combustion phase will decrease, the sudden pressure and temperature rise will also decrease. Thus, the engine runs more quietly and smoothly. In addition, NO_x emission, which is the biggest problem for diesel engines, is also significantly affected by this situation. The increase in cetane number reduces NO_x emission [36-39]. When both biodiesel and diesel standards of the EU and the USA are analyzed, it is seen that higher cetane number is required in EU standards compared to the USA. While a minimum of 51 is required as cetane specification in EN 14214, this limit is 47 in ASTM D6751. While the minimum cetane number should be 46 in EN 590, this value is 40 in ASTM D975.

The cetane number of a fuel is measured by using a cetane engine. However, since the cetane engine is very expensive, it can only be used in a very limited number of research centres. In addition, the determination of the cetane number is time-consuming and labour-intensive. Instead of cetane number, the cetane index (CI) can be calculated by using a fuel's density value and distillation range. The difference between experimentally determined cetane number and estimated cetane index is negligible. In this study, ASTM D4737-21 method was used to calculate the cetane index values of test fuels. Cetane number values of WCB and WFB fuels were quoted from Ref (27). Distillation temperatures of biodiesel fuels were given in Table 3.

Table 3. Distillation range of biodiesel fuels.

Dist. Temp.	AlB	WOB	CtB	HoB	RoB	CoB	OoB	SfB	PoB	SyB	SoB
IBP	325.3	92.0	312.2	327.5	307.7	244.1	87.3	93.4	281.8	227.2	90.0
5%	326.5	322.7	329.6	330.2	331.8	329.6	327.6	317.8	320.3	325.0	312.5
10%	336.3	323.1	330.4	330.6	331.8	330.5	328.1	326.8	321.7	327.6	320.5
15%	337.1	323.4	330.6	331.0	332.1	330.7	329.0	334.1	321.7	328.4	321.1
20%	337.8	323.8	330.9	334.8	332.5	331.0	330.0	335.4	322.0	329.1	321.8
30%	338.5	324.3	331.1	334.8	332.8	331.3	330.2	335.4	322.3	329.4	322.8
40%	339.6	325.6	332.0	334.9	333.1	331.3	330.3	335.8	322.9	329.9	324.2
50%	340.5	326.5	333.3	335.3	333.2	331.4	330.4	336.4	324.1	330.6	325.6
60%	341.6	327.1	334.4	335.9	333.5	332.2	330.5	337.2	325.0	330.9	365.5
70%	343.8	327.5	336.0	337.0	334.4	333.1	331.4	338.8	326.5	331.6	327.4
80%	345.4	328.4	338.8	338.9	335.8	334.6	333.3	339.3	327.9	333.4	328.5
90%	348.6	336.2	344.6	343.5	340.8	340.2	338.2	343.5	330.0	336.5	337.0
95%	349.8	339.4	345.6	347.8	343.4	344.6	341.7	349.3	332.1	337.8	338.2
FBP	350.6	341.1	347.2	353.9	347.9	349.5	349.0	355.2	339.8	341.3	340.1

As can be seen from Table 2 where fuel properties are given, the difference between WOB and WFB fuels with the lowest (50.54) and highest (58.80) cetane values, respectively, was 16.34%. The highest CI value (57.70) among the first generation biodiesel fuels belonged to HoB. The CI of OoB (57.09) was also very close to this value. The CIs of SoB (51.39) and SyB (51.50) were almost the same. The cetane index of CtB (55.82), which is classified as second generation biodiesel, and AlB (55.90), which is a third generation biodiesel, were almost the same. The cetane index of WCB (52.30), one of the two animal fat based biodiesels in this study, was about 11% lower than the cetane index of WFB (58.80), the other animal fat based biodiesel. However, all of the biodiesel fuels met the minimum cetane specification given in EN14214.

4. Conclusion

Biodiesel can be produced from many different feedstocks. The feedstock type from which a biodiesel fuel produced influences not only the production cost of the obtained fuel but also the sustainability of the biodiesel industry. Furthermore, the physico-chemical fuel properties of biodiesels from different origins are substantially dependent on the feedstock characteristics since the fatty acid distribution of the feedstock does not undergo a significant change during transesterification reaction in which biodiesel fuel is obtained. Biodiesel fuels are classified in three generations according to the type of feedstock they are produced from. First generation biodiesel fuels produced from conventional edible vegetable oil feedstocks, second generation biodiesel fuels produced from inedible vegetable oils, waste frying oils and waste animal fats, and third generation biodiesel fuels based on algae oil.

In this study, some key fuel properties (kinematic viscosity, density, flash point, cold filter plugging point and cetane index) of 13 different biodiesel fuels including three biodiesel generations were compared with each other and with the specification values given in European and American biodiesel standards. Among the biodiesel fuels, only the kinematic viscosity values of WOB and WCB

exceeded the upper limit value given in EN 14214 standard and could not meet this fuel specification.

The density values of biodiesel fuels were very close to each other (875.83 kg.m^{-3}-891.46 kg.m^{-3}) and were within the required standard range. AlB had the lowest flash point (142 °C). The differences between this value and the other biodiesels' flash points were significant. The highest flash point (184 °C) was measured for HoB. The cetane values of the biodiesel fuels ranged from 50.54 (WOB) to 58.80 (WFB), but all biodiesels regardless of the feedstock type met the minimum cetane limit specification. Among the fuel properties of different generation biodiesels investigated in this study, the biggest differences were seen in CFPP temperatures. The CFPP value of AlB was -10 °C, while WFB (10 °C), WOB (9 °C) and POB (8 °C) had very high CFPP temperatures. Poor cold flow properties of biodiesel fuels from waste feedstocks and palm oil can cause operational problems, especially in cold regions.

The viscosity and cold flow properties of biodiesel fuels produced from waste frying oil and waste animal fats may cause problems in case of their neat usage in internal combustion engines. However, these biodiesels, which are classified as second generation, can be blended with other biodiesel fuels in certain ratios. Thus, a relatively cheaper biodiesel can be obtained and the properties of other biodiesels such as lubricity, calorific value and oxidative stability can be improved. Among the biodiesel fuels of different generations analysed in this study, AlB has the most remarkable properties (low viscosity, density and flash point values, high cetane number and relatively good CFPP temperature). Therefore, it can be said that algae oil based biodiesel fuels have an important technical potential for being used especially in the aviation sector. In the future studies in this field, it will be useful to investigate how the fuel properties will change by blending the third generation biodiesel fuels produced from various algae oils with different jet fuels at certain ratios. Also, algae-based biodiesel fuels' effects on the characteristics of gas turbines should be studied in detail.

CRediT authorship conribution statement
Huseyin Sanli: Literature Review, Writing,

Visualization and Methodology.
Fevzi Yasar: Investigation, Experiments, Journal correspondence

Declaration of Competing Interest

The authors declare that they have no known competing financial interests or personal relationships that could have appeared to influence the work reported in this paper.

5. References

1. Statista. Industrial energy consumption worldwide in 2022, with a forecast until 2050, by energy source. https://www.statista.com/statistics/263471/industrial-energy-consumption-worldwide/ , accessed on October 8, 2024.

2. International Energy Agency (IEA). Transport-Tracking transport. Why is transport important? https://www.iea.org/energy-system/transport , accessed on October 10, 2024.

3. International Energy Agency (IEA). Global EV outlook 2024. Trends in electric cars. https://www.iea.org/reports/global-ev-outlook-2024/trends-in-electric-cars, accessed on October 10, 2024.

4. International Energy Agency (IEA). Bioenergy Annual Report 2023. https://www.ieabioenergy.com/wp-content/uploads/2024/06/Annual-Report-2023.pdf, accessed on October 11, 2024.

5. Musavi SA, Bakhshi H, Khoobkar Z, "Biodiesel production from chlorella sp. microalgae using new derived calcium methoxide-microalgae based catalyst", Fuel, Volume:387, 134459, 2025.

6. Sethin A, Oo YM, Thawornprasert J, Somnuk K, "Effects of blended diesel-biodiesel fuel on emissions of a common rail direct injection diesel engine with different exhaust gas recirculation rates", ACS Omega, Volume:9, pp:20906-20918, 2024.

7. Sanli H, "An experimental investigation on the usage of waste frying oil-diesel fuel blends with low viscosity in a common rail DI-diesel engine", Fuel, Volume:222, pp: 434-443, 2018.

8. Alptekin E, Sanli H, Canakci M, "Effects of biodiesel fuels produced from vegetable oil and waste animal fat on the characteristics of a TDI diesel engine", European Journal of Technique, Volume: 12, Issue: 1, pp: 36-42, 2022.

9. Gadore V, Mishra SR, Ahmaruzzaman Md, "Visible light-deriven photocatalytic biodiesel production using novel SnS_2/fly ash photocatalyst", Fuel, Volume:382, 133615, 2025.

10. Canakci M, Sanli H, "Biodiesel production from various feedstocks and their effects on the fuel properties", Journal of Industrial Microbiology and Biotechnology, Volume: 35, Issue: 5, pp: 431-441, 2008.

11. Pamuluri VKN, Avulapati MM, "Effect of composition and temperature on the puffing and microexplosion of diesel-ethanol-jatropha oil ternary fuel droplets", Energy, Volume:308, 132755, 2024.

12. Chen Z, Zhao P, Zhang H, Chen H, He H, Wu J, Wang L, Lou H, "An optical study on the cross-spray characteristics and combustion flames of automobile engine fueled with diesel/methanol under various injection timings", Energy, Volume:290, 130286, 2024.

13. Luo H, Fan W, Li Y, Nan G, "Biodiesel production using alkaline ionic liquid and adopted as lubricity additive for low-sulfur diesel fuel", Bioresource Technology, Volume:140, pp:337-341, 2013.

14. Gadore V, Mishra SR, Ahmaruzzaman Md, "Advances in photocatalytic biodiesel production: preparation methods, modifications and mechanisms", Fuel, Volume: 362, pp: 130749, 2024.

15. Yasar F, "Comparision of fuel properties of biodiesel fuels produced from different oils to determine the most suitable feedstock type", Fuel, Volume: 264, pp: 116817, 2020.

16. Mekonnen KD, Sendekie ZB, "NaOH-Catalyzed methanolysis optimization of biodiesel synthesis from desert date seed kernel oil", ACS Omega, Volume: 6, pp: 24082-24091, 2021.

17. Atadashi IM, Aroua MK, Abdul Aziz AR, Sulaiman NMN, "The effects of catalysts in biodiesel production: A review", Journal of Industrial and Engineering Chemistry, Volume: 19, pp: 14-26, 2013.

18. Sanli H, Alptekin E, Canakci M, "Production of Fuel Quality Ethyl Ester Biodiesel: 1. Laboratory-Scale Optimization of Waste Frying Oil Ethanolysis, 2. Pilot-Scale

Production with the Optimal Reaction Conditions", Waste and Biomass Valorization, Volume: 10, pp:1889-1898, 2019.

19.   Alptekin E, Canakci M, Sanli H, "Evaluation of leather industry wastes as a feedstock for biodiesel production", Fuel, Volume: 95, pp: 214-220, 2012.

20.   Verma P, Sharma MP, Dwivedi G, "Impact of alcohol on biodiesel production and properties", Renewable and Sustainable Energy Reviews, Volume: 56, pp: 319-333, 2016.

21.   Kumar N, "Oxidative stability of biodiesel: Causes, effects and prevention", Fuel, Volume: 190, pp: 328-350, 2017.

22.   Leng L, Li W, Li H, Jiang S, Zhou W, "Cold Flow Properties of Biodiesel and the Improvement Methods: AReview", Energy Fuels, Volume: 34, pp: 10364-10383, 2020.

23.   Fathurrahman NA, Auzani AS, Zaelani R, Anggrani R, Aisyah L, Wibowo CS, "Lubricity Properties of Palm Oil Biodiesel Blends with Petroleum Diesel and Hydrogenated Vegetable Oil", Lubricants, Volume: 11, Issue: 4, 2023.

24.   Haas MJ, McAloon AJ, Yee WC, Foglia TA, "A process model to estimate biodiesel production costs", Bioresource Technology, Volume: 97, Issue: 4, pp: 671-678, 2006.

25.   Pourhoseini SA, Karimian A, "Optimization of oil extraction from Melia azedarach fruits using methanol-modified SC-CO2 for highly efficient biodiesel production using a modified LAC catalyst", Fuel, Volume: 380, pp: 133024, 2025.

26.   Pandey S, Narayanan I, Selveraj R, Varadavenkatesan T, Vinayagan R, "Biodiesel production from microalgae: A comprehensive review on influential factors, transesterification processes, and challenges", Fuel, Volume: 367, pp: 131547, 2024.

27.   Alptekin E, Canakci M, Ozsezen AN, Turkcan A, Sanli H, "Using waste animal fat based biodiesels-bioethanol-diesel fuel blends in a DI diesel engine", Fuel, Volume: 157, pp: 245-254, 2015.

28.   Fu J, "Flash points measurements and prediction of biofuels and biofuel blends with aromatic fluids", Fuel, Volume: 241, pp: 892-900, 2019.

29.   Zhang Z, Li D, Niu C, Pan M, Guan W,

Liu H, Lu K, Tan D, "Soot formation mechanism of modern automobile engines and methods of reducing soot emission for catalyzed diesel particulate filter: A review", Process Safety and Environmental Protection, Volume: 190, pp: 1403-1430, 2024.

30.   Sia CB, Kansedo J, Tan YH, Lee KT, "Evaluation on biodiesel cold flow properties, oxidative stability and enhancement strategies: A review", Biocatalysis and Agricultural Biotechnology, Volume: 24, pp: 101514, 2020.

31.   Santos SM, Wolf-Maciel MR, Fregolente LV, "Cold flow properties: Applying exploratory analyses and assessing predictive methods for biodiesel and diesel-biodiesel blends", Sustainable Energy Technologies and Assessments, Volume: 57, pp: 103230, 2023.

32.   Wang B, Lau YS, Huang Y, Organ B, Chuang HC, Ho SSH, Qu L, Lee SC, Ho KF, "Chemical and toxicological characterization of particulate emissions from diesel vehicles", Journal of Hazardous Materials, Volume: 405, pp: 124613, 2021.

33.   Tan P, Zhao J, Hu Z, Lau D, Du A, Du D, "Effects of fuel properties on exhaust emissions from diesel engines", Journal of Fuel Chemistry and Technology, Volume: 4, Issue: 3, pp: 347-355, 2013.

34.   Agarwal AK, Singh AP, Maurya RK, Shukla PC, Dhar A, Srivastava DK, "Combustion characteristics of a common rail direct injection engine using different fuel injection strategies", International Journal of Thermal Sciences, Volume: 134, pp: 475-484, 2018.

35.   Sanli H, Alptekin E, Canakci M, "Using low viscosity micro-emulsification fuels composed of waste frying oil-diesel fuel-higher bio-alcohols in a turbocharged-CRDI diesel engine", Fuel, Volume: 308, pp: 121966, 2022.

36.   Wei YJ, Zhang YJ, Zhu XD, Gu HM, Zhu ZQ, Liu SH, Sun XY, Jiang XL, "Effects of diesel hydrocarbon components on cetane number and engine combustion and emission characteristics", Applied Sciences, Volume: 12, pp: 3549, 2022.

37.   Sahin S, Ersoy E, Menges HA, "Determination of some fuel properties of binary biodiesel and binary biodiesel-diesel blend fuels obtained from camelina oil and

waste frying oils", International Journal of Automotive Engineering and Technologies, Volume: 13(1), pp: 1-11, 2024.

38.   Balki MK, "Biodiesel production from waste frying oil by electrochemical method using stainless steel electrode", International Journal of Automotive Engineering and Technologies, Volume: 13(1), pp: 54-62, 2024.

39.   Kamble B, Revuru RS, Zhang Z, "A comprehensive investigation of injection strategies for improving diesel engine combustion under cold start development", International Journal of Automotive Engineering and Technologies, Volume: 13(2), pp: 73-83, 2024.
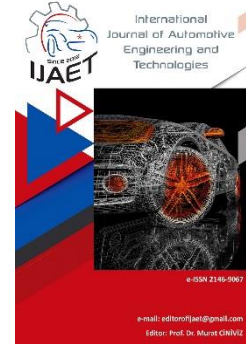
Original Research Article

Examining the effect of adding natural gas to an engine using a gasoline-methanol mixture as fuel on engine performance and emissions

Talip Akbıyık[1, *]

[1, *] Motor Vehicles and Transportation Technologies, Aksaray University, Aksaray Türkiye.

ARTICLE INFO

ABSTRACT

The power produced by the combustion of fossil fuels in internal combustion engines is transferred to the powertrain, and this generated power causes carbon dioxide (CO_2) and particulate matter emissions. Systems that do not cause CO_2 and other harmful emissions or cause less emissions are a strong alternative. In this context, methanol and natural gas are added to the engine to reduce emissions. In this study, engine performance and emissions were examined using three fuel mixtures. A two-cylinder gasoline engine was run using M20 fuel and natural gas was added at different rates from the engine manifold. The engine was operated at a constant 3000 rpm and using 6 different fuels (gasoline, M20, M20+50 g natural gas, M20+100 g natural gas, M20+150 g natural gas, M20+200 g natural gas), at different torque values (5, 10, 15 and 20 Nm) engine performance and emission values were compared. When fuel consumption is compared to gasoline fuel, the overall cycle average is 6% higher in M20, 3% higher in M20+50 and M20+100, 1% higher in M20+150 and 6% higher in M20+200, and emissions are reduced compared to gasoline in other fuels.

Keywords: Gasoline, methanol, natural gas, emission, engine performance.

1. Introduction

Fuel cell vehicles [1] or battery-using vehicles [2, 3, 4] are attracting increasing attention, considering the carbon dioxide (CO_2) and particulate matter emissions produced in the transfer of power produced as a result of the combustion of fossil fuels to the powertrain. Fuel cells are a potentially powerful technology because they do not cause CO_2 and other harmful emissions [5]. Similarly, these zero-emission systems have been widely used in urban vehicle applications [6, 7]. However, the use of internal combustion engine technology for heavy-duty vehicles with high levels of power requirements and long-distance transportation is likely to continue for many years [8]. Among these internal combustion engines (diesel, gasoline, natural gas and alcohol engines), natural gas spark ignition (SI) engines have been more widely used, especially in heavy-duty vehicle applications [9].

In natural gas SI engines, two combustion modes are used for combustion technology: stoichiometric and lean-burn combustion [10]. Extremely low emissions can be achieved in

stoichiometric combustion through simple three-way catalyst equipment. Lean-burn combustion can achieve higher thermal efficiency but must be equipped with a high-cost after-treatment to meet the EURO VI emission regulation [11]. Due to increasingly stringent emission regulations, most natural gas SI engines operate in stoichiometric mode rather than lean-burn combustion mode but have low thermal efficiency and need precise air-fuel ratio control strategies [12]. Methane, the main component of natural gas, has a low laminar flame speed, resulting in incomplete combustion and high emissions of unburned hydrocarbons [13, 14].

Using natural gas together with liquid fuels with high flame spread rates may be a promising approach to improve the combustion characteristics of a natural gas SI engine. Methanol is considered the best alternative fuel for IC engines due to its following advantages. First, methanol is a renewable fuel that can be synthesized from hydrogen and CO_2 captured from the atmosphere [15]. Second, the laminar flame speed of methanol is higher than all other hydrocarbon fuels [16]. Third, methanol has high latent heat evaporation. Therefore, volumetric efficiency can be significantly increased when methanol is injected into the intake manifold [17]. Fourth, the oxygen content of methanol is almost 50% by mass. Therefore, methanol as an additive can lead to complete combustion [18]. There are many studies in literature regarding the advantages of methanol and natural gas.

Akbıyık et al. [19] investigated the effect of boron addition to lubricating oil on engine performance and emissions when gasoline and natural gas were used as fuel in a spark ignition engine. Experimental results showed that the use of boron-added lubricating oil caused an average reduction of 2.4-8% in specific fuel consumption when gasoline and natural gas were used as fuel in the engine. They found that the use of boron in lubricating oil did not cause a significant change in CO_2, CO and HC emissions, but caused a significant decrease in NO_X emissions by 11.4-12.9%.

Verhelst et al [20] made a systematic investigation of methanol as a fuel in internal combustion engines. Improved thermal efficiency can be achieved when methanol is used as pure fuel or blend component for IC engines. This is due to the advantages of methanol, such as high latent heat evaporation, fast combustion rate, and no carbon-carbon bond, which leads to increased compression ratio and shrinkage.

Akbıyık et al. [21] tested four different torque values (5, 10, 15, 20 Nm) at a constant 3000 rpm using four different fuels (gasoline, gasoline + 50 g natural gas, M20 and M20 + 50 g natural gas). In the tests, they stated that the lowest specific fuel consumption and the best emissions were achieved with gasoline + 50 g natural gas fuel, and that the first and second law efficiencies of all fuel types increased with the increase in torque values in the energy and exergy analysis. They found that the combination of 50 g of natural gas fuel and gasoline gave the best results.

Chen et al. [22, 23, 24] They reviewed innovative research on natural gas/methanol dual fuel engines. They stated that the combustion of methanol and natural gas can be controlled in a complementary strategy and thus, the combustion rate of natural gas can be significantly increased by the introduction of methanol, resulting in better thermal efficiency and reduced hydrocarbon emissions. Akbıyık et al. [25] investigated the effects of using CNG (natural gas) and gasoline in spark ignition engines on engine emissions, performance and lubricating oil by adding boron additive to engine oil. As test results, they found that engine performance decreased over time from the moment the engine oil was first added, but when boron-added oil was used in the engine, the decrease in engine performance was less than when boron-free engine oil was used. They reported that the use of boron additive in lubricating oil not only reduces NO_X emissions but also causes the properties of the lubricating oil to change less as the engine temperature decreases.

Dumanlı et al. [26] experimentally examined 4 different torque values (5, 10, 15, 20 Nm) in the engine with different volumetric ratios of methanol and gasoline fuel mixtures (M10, M20, M30, M40) at a constant 3000 engine speed. As a result of the study, engine performance, emission and energy analysis were carried out.

Akbıyık and Ark [27] in an experimental study, found that adding natural gas at different rates (50, 100, 150 and 200 g/hour) to the intake air at a constant 3000 rpm affected the engine performance and emissions at different torque values (5, 10, 15 and 20 Nm) examined its effect. As a result of the experiment, it was determined that adding natural gas to gasoline reduces fuel consumption, emissions decrease as the torque value increases, and thermal efficiency increases as the natural gas addition rate increases.

Singh et al. [28] The combustion and emissions of SI engines operating in dual fuel mode with natural gas/gasoline have been examined experimentally. They found that gasoline engine knocking performance at medium and high engine loads could be eliminated by the use of natural gas. Pan et al. [29] They examined the combustion characteristics of a methane enriched gasoline engine. They found that adding methane to gasoline accelerates the combustion process in the initial stage under conditions of low compression ratios, lean combustion and fuel stratification.

Yin et al. [30] Dual direct coding technology is a very promising method to determine the mixture organization and combustion process of dual-fuel engines. In this way, the performance of a modified dual-fuel turbine operating on methanol and diesel fuel was investigated separately at various methanol energy replacement amounts and diesel replacement timings. Independent coupling in methanol and diesel, staying real-time and accurate thanks to the dual-direct coupling system with two different in-cylinder injectors according to engine operating performance. The results show that dual-direct cooling technology has great potential for extending the turbine operating range with the specified thermal heat exchange and exhaust emissions. Simio et al. [31] In this study, the engine running on compressed natural gas was fed with various percentages of natural gas and hydrogen mixtures and tested under different conditions. A detailed combustion and emission analysis was performed. The response of the engine management system to different fuels was evaluated when rapid speed and torque changes occurred.

As mentioned above, adding alternative fuel by operating in dual-fuel, dual-injection mode is an effective approach to increase thermal efficiency and reduce emissions. For a spark ignition engine there is a lot of work in dual fuel combustion mode. Both natural gas and methanol can be added to a gasoline engine when operated in dual-fuel combustion mode. However, the impact of gasoline, methanol and natural gas in triple fuel mode on the engine performance and emissions of SI engines is still unknown. For this reason, there is no information in the literature comparing the combustion performance and emissions of mixed fuel engines running on gasoline, methanol and natural gas. In this study, the effects of using three fuel mixtures in SI engines on engine performance and emissions were examined. This study provides useful information in combustion optimization to increase the thermal efficiency of engines and reduce exhaust emissions.

2. Material and Method
2.1. The experimental setup

In the experimental setup, Lombardini LGW 523 MPI 2-cylinder gasoline engine, Net Brake 80 electric dynamometer, Federal exhaust emission device, computer, liquid fuel flowmeter and mass flowmeter for gaseous fuels were used. The shape of the experimental setup is given in Figure 1. The engine used in the experiments is a Lombardini LGW 523 MPI 2-cylinder, water-cooled, injection engine. The technical specifications of the engine are given in table 1. The dynamometer used in the experiments has the capacity to measure 83 Nm torque and 70 kW power. Federal emission devices were used to determine emissions. For liquid fuels, it is determined by weight with the help of a load cell. Alicat mass flowmeter was used for gaseous fuels. The properties of the fuels used in the experiments are given in Table 2. The content of natural gas used in the experiments is given in table 3. Specifications and error range of the equipment and sensors are given in Table 4.

2.2. Test method

In this study, 6 different fuels were used and compared at 3000 rpm and tested at different

torque values. 6 different fuels (gasoline, M20, M20+50 Natural Gas, M20+100 Natural Gas, M20+150 Natural Gas, M20+200 Natural Gas) were used in the experiment. M20 fuel is a volumetric mixture of 20% methanol and 80% gasoline. 50, 100, 150 and 200 g of natural gas per hour were added to this fuel from the engine's intake manifold. The amount of natural gas was determined by an Alicat mass flow meter. Using these fuels, power, fuel consumption and emission values were compared at 4 different torque values (5, 10, 15 and 20 Nm) at a constant engine speed of 3000 rpm.

Table1.Lombardini LGW 523 engine features [21]

Engine Type	Unit	Result
Number of cylinders	pcs.	2
Diameter of the cylinder	mm	72
Stroke	mm	62
Cylinder volume	cc	505
Stroke ratio		10.7:1
Revolution maximum	rpm	5500
Maximum of the power (5000 rpm)	kW/HP	15/20.4
Maximum of the torque (2150 rpm)	Nm	34
Engine curb weight	kg	52

Figure 1. Schematic view of the experimental setup

Table 2. Fuel Properties of the gasoline, methane and methanol [23]

Fuel properties	Gasoline	Methane	Methanol
Density [kg/m^3]	720–775	0.67	792
Adiabatic flame temperature [K]	2030	2320	1878
Lower heating value [MJ/kg]	42-44	50	20.1
Flame speed [m/s]	0.57	0.37	0.52
Stoichiometric air fuel ratio	14.6	17.24	6.45
Auto-ignition temperature [ºC]	440	600	470
Flammability limits [vol.%]	1.4-7.6	5.3-14	6-37
Octane no RON	95	130	110
Octane no MON	85	105	87

Table 3. Natural gas component [23]

Chemical component	Chemical Formula	Rate (%)
Methane	CH_4	90.8
Ethane	C_2H_6	3.6
Propane	C_2H_8	1.1
Butane	C_4H_{10}	0.4
Pentane	C_5H_{12}	0.1
Nitrogen	N_2	3.5
Carbon Dioxide	CO_2	0.4

Table 4. Specifications and error range of the experimental equipment and sensors.

Instrument	Values	Accuracies
Liquid flow meter	0.001–5 kg	±0.001%
Gas flow meter (Alicat)	1–1000 SLPM	±0.4%
Electric Dynamometer (Netfren)	70 kW/8000 rpm	±1 rpm
Exhaust gas analyzer (Federal)		
CO	0–10% Vol	0.001% vol
CO_2	0–18% Vol	0.010% vol
O_2	0–22% Vol	0.010% vol
NO_x	0–5000ppm	1.0ppm
HC	0–9999ppm	1.0ppm
Lambda	0.5–9.999	0.001

3. Results and Discussion

One of the most important parameters in determining engine performance is power. In engines, power varies according to torque and speed. Since speed and torque are constant in the experiments, the power values are the same, but there are small differences, and this is due to the limits allowed in the experiments. The power change depending on torque is given in Figure 2.
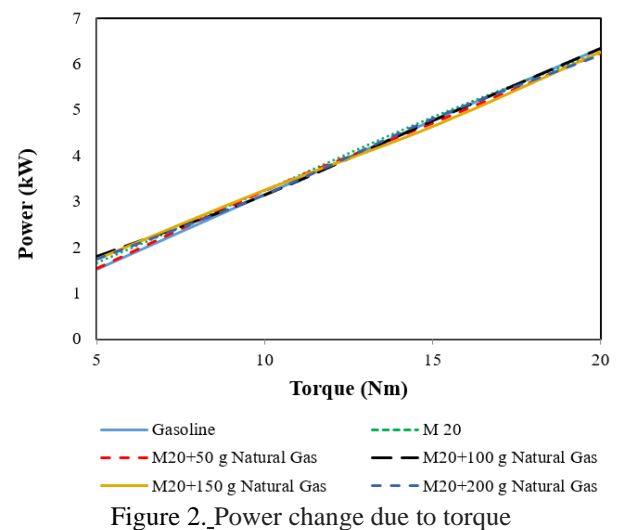

Figure 2. Power change due to torque

Figure 3 shows the change in different torque values of 6 different fuels at 3000 rpm. BSFC

shows the amount of fuel consumed per unit power. Compared to gasoline, alcohol fuels have lower calorific values and higher stoichiometric A/F ratios, causing more fuel to be used for the same output power. For this reason, in the use of alcohol fuels, the BSFC is slightly higher than in gasoline [32-35]. The addition of natural gas reduced the specific fuel consumption value. As the torque value increased, the specific fuel consumption value decreased. The reduction rate between 5 and 20 Nm torque values is 55% for gasoline fuel, 52% for M20 fuel, 54% for M20+50 g natural gas fuel, 48% for M20+100 g natural gas fuel, 51% for M20+150 g natural gas fuel and 51% for M20+200 g natural gas fuel. There has been a 55% reduction in natural gas fuel consumption.
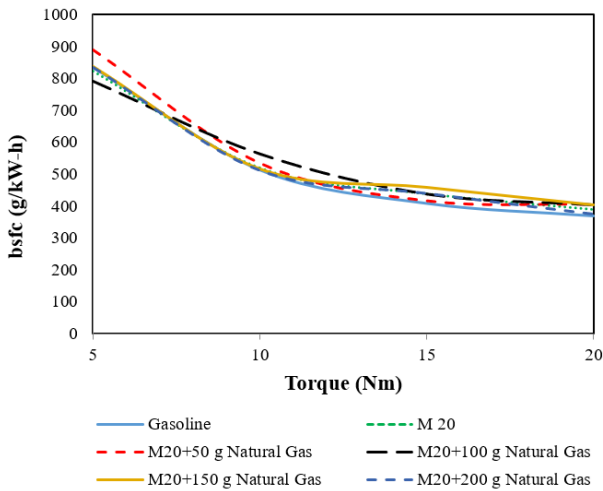

Figure 3. Specific fuel consumption change depending on torque

Fuel consumption curves are given in Figure 4. Adding methanol to gasoline increased fuel consumption. Fuel consumption decreased by adding natural gas. The lowest fuel consumption was obtained with gasoline + 200 g/h natural gas fuel, and the highest fuel consumption was obtained with M20 fuel. Fuel consumption values increased with increasing torque amounts.

When Figure 5 is examined, it is seen that CO decreases with increasing torque values. As the torque value increases and the air velocity entering the cylinders increases, turbulence in the combustion chamber increases, resulting in a more homogeneous mixture. Since this will improve the combustion of fuel, there will be a decrease in CO at high speeds. The lowest CO emission values were obtained for gasoline +

100 g natural gas and gasoline + 150 natural gas fuels. As can be seen from the graph, the addition of methanol increased CO emissions at 5 and 10 Nm torque values and has the lowest values at other torque values. In addition to natural gas, the lowest values were obtained at 100 and 150 g additions. At high torque values, combustion improves, and CO emissions decrease with increasing pressure and temperature.
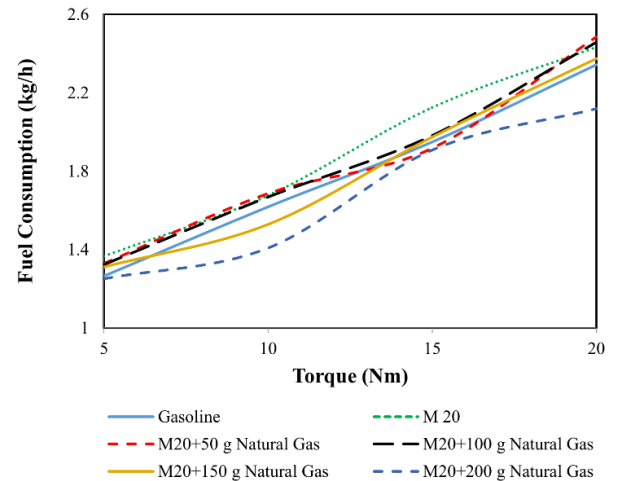

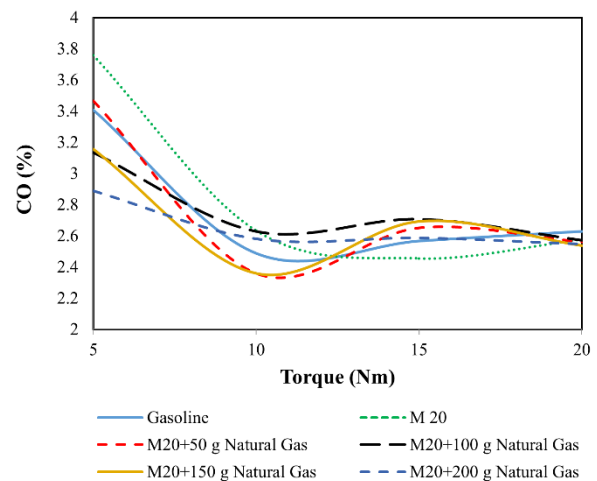Figure 4. Fuel consumption changes depending on torque

Figure 5. CO change due to torque

Figure 6 shows the measured HC emissions of the study. Hydrocarbon emissions are caused by fuel expelled from the exhaust without being burned. When Figure 6 is examined, HC emissions are less in methanol mixtures. HC emissions decrease as the natural gas addition rate increases. Since methanol's lower calorific value and stoichiometric A/F ratio are much lower than gasoline, HC emissions decrease [35]. In addition, with increasing torque values, it increases up to 15 Nm torque and then decreases slightly.
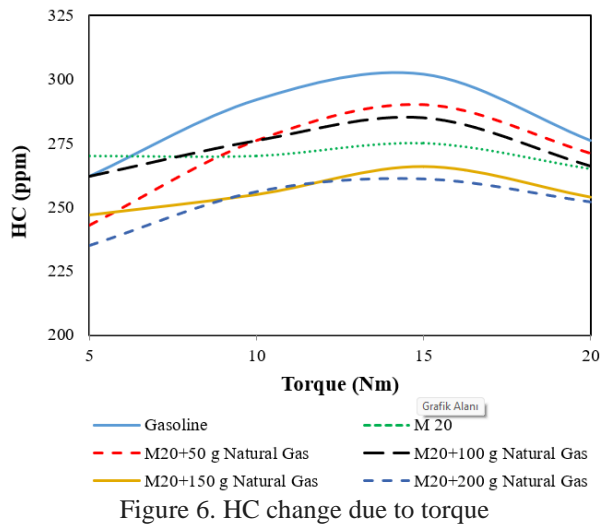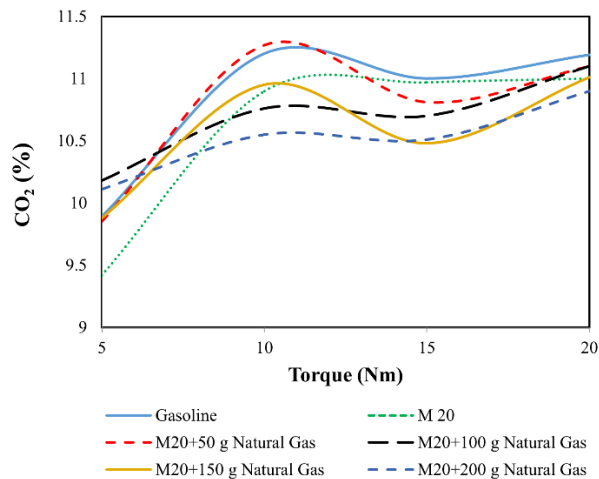
Figure 6. HC change due to torque

Figure 7 shows the CO_2 emission changes for fuels with different torque values. CO_2 is a gas that causes global warming. Fuels with fewer or no carbon atoms are preferred in terms of CO_2 emissions. When the graph in Figure 7 is examined, there is a decrease in CO_2 emissions in the methanol mixture. As the proportion of natural gas in the fuel mixture increases, CO_2 emission values decrease. As the torque value increases, CO_2 emissions increase. The reason for the decrease in CO_2 emissions with methanol is the low C/H ratio of methanol and the fact that the C atom in its structure is less than that of gasoline.

Figure 7. CO_2 change due to torque

NO_X emission changes for each fuel at different torque values are given in Figure 8. When the graph in Figure 8 is examined, it is seen that NO_X emissions are lower in methanol operation than in gasoline, and emissions decrease with the addition of natural gas. In each fuel type, NO_X emissions increase with increasing engine load. At maximum torque, the most filling is taken into the cylinder and

temperatures increase. High temperatures cause NO_X emissions to increase. The reason why NO_X emissions are low in studies involving methanol and natural gas additions is that methanol has a high evaporation temperature and natural gas is given in gaseous form, thus cooling the mixture and ultimately reducing the cycle temperature.
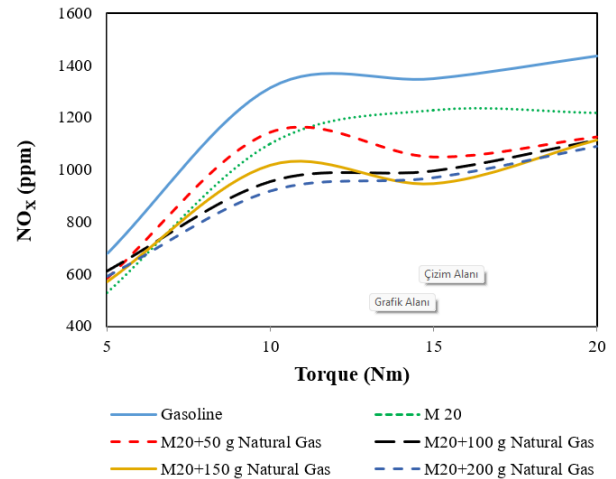
Figure 8. NO_X change depending on torque

4. Conclusion and Recommendations

In a study conducted by adding both natural gas and methanol to a spark-ignition gasoline engine, its effect on engine performance and emissions was examined. In this study, power, fuel consumption and emissions (CO, CO_2, HC and NO_X) were examined, and 6 fuels were compared. In the results obtained.

- There was no change in power.
- The addition of methanol increased the BSFC, and the addition of natural gas decreased the BSFC. As the torque value increased, the BSFC value decreased.
- Addition of methanol increased the amount of fuel consumption, and addition of natural gas decreased the amount of fuel consumption. As the torque value increased, the amount of fuel consumption increased.
- The emission values of fuels with added methanol and natural gas gave better results when compared to gasoline fuel.

Abbreviations

SI   : Spark Ignition
CO   : Carbon monoxide
CO_2 : Carbon dioxide
HC   : Hydrocarbon
NO_X : Nitrogen Oxides
IC   : Internal Combustion

BSFC : Brake Specific Fuel Consumption
RON   : Research Octane Number
MON   : Motor Octane Number

CRediT authorship contribution statement

Talip Akbıyık: Conceptualization, Data curation, Formal analysis, Investigation, Methodology, Software, Validation, Visualization, Writing – original draft, Writing – review & editing.

Declaration of Competing Interest

The author declares that they have no known competing financial interests or personal relationships that could have appeared to influence the work reported in this paper.

5. References

1.   Schafer, A., Heywood, JB., Weiss, MA., Future fuel cell and internal combustion engine automobile technologies: a 25-year life cycle and fleet impact assessment, Energy, 31(12):2064-2087, 2006.

2.   Oh, S., Park, C., Kim, S., Kim, Y., Choi,Y., Kim, C., Natural gaseammonia dual-fuel combustion in spark-ignited engine with various airefuel ratios and split ratios of ammonia under part load condition, Fuel, 290:120095, 2021.

3.   Xie, Y., Li, Y., Zhao, Z., Dong, H., Wang, S., Liu, J., Microsimulation of electric vehicle energy consumption and driving range, Applied Energy, 267: 115081, 2020.

4.   Zhang, B., Carlson, RB., Smart, JG., Dufek, EJ., Liaw, B., Challenges of future high power wireless power transfer for light-duty electric vehicles technology and risk management, eTransportation, 2:100012, 2019.

5.   Inci, M., Büyük, M., Demir, MH., Ilbey, G., A review and research on fuel cell electric vehicles: topologies, power electronic converters, energy management methods, technical challenges, marketing and future aspects, Renewable and Sustainable Energy Reviews, 137:110648, 2021.

6.   Zhuang, W., Li, S., Zhang, X., Kum, D., Song, Z., Yin, G., A survey of powertrain configuration studies on hybrid electric vehicles, Applied Energy, 262:114553, 2020.

7.   Li, Y., Wang, S., Duan, X., Liu, S., Liu, J., Hu, S., Multi-objective energy management for Atkinson cycle engine and series hybrid electric vehicle based on evolutionary NSGA-II algorithm using digital twins, Energy Conversion and Managment, 230: 113788, 2021.

8.   Chen, Z., He, J., Chen, H., Wang, L., Geng, L., Experimental study of the effects of spark timing and water injection on combustion and emissions of a heavyduty natural gas engine, Fuel, 276:118025, 2020.

9.   Zhang, S., Li, Y., Wang, S., Zeng, H., Liu, J., Duan, X., et al. Experimental and numerical study the effect of EGR strategies on in-cylinder flow, combustion and emissions characteristics in a heavy-duty higher CR lean-burn NGSI engine coupled with detail combustion mechanism, Fuel, 276:118082, 2020.

10.   Chen, Z., Chen, H., Geng, L., Influence of water port injection on cycle-to-cycle variations in heavy-duty natural gas engine under low load, Fuel, 280:118678, 2020.

11.   Chen, H., He, J., Zhong, X., Engine combustion and emission fuelled with natural gas: a review, Journal of the Energy Institute, 92(4):1123-1136, 2019.

12.   Cho, HM., He, B-Q., Spark ignition natural gas enginesda review, Energy Conversion and Managment, 48(2):608-618, 2007.

13.   Wang, J., Huang, Z., Tang, C., Zheng, J., Effect of hydrogen addition on early flame growth of lean burn natural gaseair mixtures, International Journal of Hydrogen Energy, 35(13):7246-7252, 2010.

14.   Wang, J., Huang, Z., Zheng, J., Miao, H., Effect of partially premixed and hydrogen addition on natural gas direct-injection lean combustion, International Journal of Hydrogen Energy, 34(22):9239-9247, 2009.

15.   Gong, C., Li, Z., Sun, J., Liu, F., Evaluation on combustion and lean-burn limitof a medium compression ratio hydrogen/methanol dual-injection spark-ignition engine under methanol late-injection, Applied Energy, 277:115622, 2020.

16.   Veloo, PS., Wang, YL., Egolfopoulos, FN., Westbrook, CK., A comparative experimental and computational study of methanol, ethanol, and n-butanol flame, Combustion and Flame, 157(10):1989-2004, 2010.

17.   Gong, C., Yi, L., Zhang, Z., Sun, J., Liu, F., Assessment of ultra-lean burn

characteristics for a stratified-charge direct-injection spark-ignition methanol engine under different high compression ratios, Applied Energy, 261:114478, 2020.

18.   Gong, C., Zhang, Z., Sun, J., Chen, Y., Liu, F., Computational study of nozzle spray-line distribution effects on stratified mixture formation, combustion and emissions of a high compression ratio DISI methanol engine under lean-burn condition, Energy, 205:118080, 2020.

19.   Akbıyık, T., Kahraman, N., Taner, T., Investigation of the effect of boron additive to lubricating oil on engine performance, exhaust, and emissions, Fuel, 312, 122931, 2022.

20.   Verhels,t S., Turner, JWG., Sileghem, L., Vancoillie, J., Methanol as a fuel for internal combustion engines, Progress in Energy and Combustion Science, 70:43-88, 2019.

21.   Akbıyık, T., Kahraman, N., Taner, T., Energy and exergy analysis with emissions evaluation of a gasoline engine using different fuels, 2023, 345, 128189, Fuel.

22.   Chen, Z., Wang, L., Zhang, Q., Zhang, X., Yang, B., Zeng, K., Effects of spark timing and methanol addition on combustion characteristics and emissions of dual-fuel engine fuelled with natural gas and methanol under lean-burn condition, Energy Conversion and Managment,181:519-527, 2019.

23.   Akbıyık, T., Kahraman, N., Taner, T., The effect of boron-doped addition to spark ignition engine oil on engine emission, performance and lubricating oil properties, 2022, 324, 124783, Fuel.

24.   Dumanlı, A.T., Çeper, B.A., Akbıyık, T., Kahraman, N., Experimental Investigation of Energy Analysis of Methanol-Gasoline Mixtures at Different Torque Values Energy, Enviroment and Storage, 15-20, 2024,

25.   Akbıyık, T., Kahraman, N., Çeper, B.A., Investigation of The Effect of Adding Natural Gas to A Gasoline Engine On Engine Performance and Emissions Energy, Enviroment and Storage, 116-120, 2024,

26.   Chen, Z., Wang, L., Yuan, X., Duan, Q., Yang, B., Zeng, K., Experimental investigation on performance and combustion characteristics of spark-ignition dual-fuel engine fueled with methanol/natural gas, Applied Thermal Engineering, 150:164-174,

2019.

27.   Wang, L., Chen, Z., Zhang, T., Zeng, K., Effect of excess air/fuel ratio and methanol addition on the performance, emissions, and combustion characteristics of a natural gas/methanol dual-fuel engine, Fuel, 255:115799, 2019.

28.   Singh, E., Morganti, K., Dibble, R., Dual-fuel operation of gasoline and natural gas in a turbocharged engine, Fuel, 237:694-706, 2019.

29.   Pan. J., Li, N,, Wei, H., Hua, J., Shu, G., Experimental investigations on combustion acceleration behavior of methane/gasoline under partial load conditions of SI engines, Applied Thermal Engineering, 139:432-44, 2018.

30.   Yin, X., Yan, Y., Ren, X., Yu, L., Duan, H., Hu, E., Zeng, K., Effects of methanol energy substitution ratio and diesel injection timing on a methanol/diesel dual-fuel direct injection engine, Fuel, Volume 382, Part B, 15 February, 133773, 2025.

31.   Simio, L., D., Iannaccone, S., Guido, C., Napolitano, P., Maiello, A., Natural Gas/Hydrogen blends for heavy-duty spark ignition engines: Performance and emissions analysis, International Journal of Hydrogen Energy, Volume 50, Part B, 2 January, Pages 743-757, 2024.

32.   Balki, M.K., Sayin, C., Canakci, M., The effect of different alcohol fuels on the performance, emission and combustion characteristics of a gasoline engine, Fuel, 145, 2012.

33.   Bayındır, H., Yücesu, H.S., Effects of ethanol-gasoline mixtures and intake manifold filler temperature on engine performance and exhaust emissions, 6th International Combustion Symposium, 19-21 July, Istanbul, Türkiye, p.395-408, 1999.

34.   Salman, M.S., Sümer, M., Effect of using ethanol and ethanol-gasoline mixture on engine performance in spark ignition engines, Journal of Polytechnic, 2(2), 27-35 1999.

35.   Gravalos, I., Moshou, D., Gialamas, T., Xyradakis, P., Kateris, D., Tsiropoulos, Z., Performance and Emission Characteristics of Spark Ignition Engine Fuelled with Ethanol and Methanol Gasoline Blended Fuels, Alternative Fuel, Manzanera, M. Editor.; Intech, Rijeka, Croatia, p.155-174, 2011.